Master of Science Thesis

The effect of wing deformation on unsteady aerodynamic mechanisms in hovering flapping flight

A numerical study using a three-dimensional immersed boundary method

Tijs Noyon

March 17, 2014

Aerodynamics

TU Delft

Faculty of Aerospace Engineering

Delft University of Technology

The effect of wing deformation on unsteady aerodynamic mechanisms in hovering flapping flight

A numerical study using a three-dimensional immersed boundary method

Master of Science Thesis

For obtaining the degree of Master of Science in Aerospace Engineering
at Delft University of Technology

Tijs Noyon

March 17, 2014

Faculty of Aerospace Engineering · Delft University of Technology

Delft University of Technology

DELFT UNIVERSITY OF TECHNOLOGY
DEPARTMENT OF AERODYNAMICS

The undersigned hereby certify that they have read and recommend to the Faculty of Aerospace Engineering for acceptance the thesis entitled **"The effect of wing deformation on unsteady aerodynamic mechanisms in hovering flapping flight"** by **Tijs Noyon** in fulfillment of the requirements for the degree of **Master of Science**.

Dated: March 17, 2014

Supervisors:

prof. dr. ir. drs. H. Bijl

dr. ir. B.W. van Oudheusden

dr. W.B. Tay, MSc

ir. C. de Wagter

Preface

This thesis marks the end of my master in aerodynamics at the TU Delft. I have several people to thank for helping me during the final stage of my master and completing this thesis. First of all I would like to thank my supervisor Wee-Beng Tay for always having time to talk about the assignment and troubleshoot issues with the IBM solver. Even from half way across the world you always had time to help me out and give advice when needed. Secondly I'd like to thank my other supervisors Bas van Oudheusden and Hester Bijl for their input during our meetings.

Finally I want to thank parents for supporting me throughout my study and their patience with me while finishing this final part.

Tijs Noyon
Delft, March 2014

Abstract

This study investigated the effect of chord deformation on the unsteady aerodynamic mechanisms found in hovering flapping flight at a Reynolds number of $\mathcal{R}e = 2002$. This was done in order to get a better understanding of the physics involved in flapping flight, which in turn could lead to improved Micro Aerial Vehicle (MAV) designs. A three-dimensional numerical study was performed using an immersed boundary method (IBM) with the discrete forcing approach. The solver was first validated against an experiment by Kim and Gharib (2011).

The effect of deformation was investigated by modeling a flapping wing as a flat plate. This plate had an aspect ratio of 2 and three different time dependent chord shapes were defined: a rigid case that only included rotation around the leading edge, a case with the maximum deformation at the trailing edge (the deforming end case) and a case with the maximum deformation at the center (the deforming center case). In the deforming end case the angle of attack near the leading edge was increased compared to the rigid case, whereas in the deforming center case the angle of attack near the leading edge was decreased. A flapping angle of $\theta = 45^\circ$ was chosen, which is typical to that of a wing in a four-winged MAV in biplane configuration. The simulated configuration corresponds to one wing pair, where the effect of the two wings on one another was simulated by use of a symmetry plane.

When the deformation was taken constant along the span, the deforming center case created the highest lift coefficient (C_L), followed by the rigid case and the deforming end case created the lowest C_L. The curvature of the deforming center case caused a higher pressure on the lower surface of the plate, whereas the deforming end case reduced the pressure on the lower surface. The higher angle of attack created by the deforming end case caused a faster C_L buildup, created by a faster buildup of the leading edge vortex (LEV). The lower angle of attack in the deforming center case caused a slower LEV buildup and therefore slower C_L buildup. In all cases the presence of the symmetry plane increased LEV buildup, causing a higher C_L during the outstroke. No shedding of the LEV was observed in any of the cases.

When the deformation was varied along the span both deforming cases showed a higher C_L compared to the rigid case. For the deforming end case this was caused by a low pressure region near the trailing edge of the tip of the plate caused by a combination of the tip and trailing edge vortex. A distinct hump in C_L buildup was shown to be caused by the interaction of the LEV with the LEV shed from the previous stroke. This interaction was delayed for the deforming center case, both by the slower LEV buildup and because the previously shed

vortex got trapped below the plate, limiting the interaction.

Decreasing the distance to the symmetry plane showed an increased buildup speed of the LEV, resulting in a faster C_L buildup. The positive effect of the faster LEV buildup on C_L was limited, since the stronger LEV interacted much faster with the vortex shed from the previous stroke, thus limiting further growth. As a result of this, the beneficial effect of the deforming center on delaying the interaction was reduced when moving the plate closer to the symmetry plane.

A later peak in C_L showed a longer C_L buildup and therefore led to a higher C_L^{max}. The moment C_L^{max} was reached during strokes depended on the trailing edge vortex (TEV) and the tip vortex (TV) behavior. The effect of the TEV and TV behavior on the timing depends on the orientation of the surface of the plate on the location of the vortex. This dependence means the positive and negative effects on the TEV and TV depend on the shape of the plate. For the deforming center case C_L benefits from a stronger TV near the leading edge, whereas for the deforming end case C_L benefits from the fact that the TEV stays closer to the trailing edge.

The deformation of the wing is shown to play a significant role in the aerodynamic performance of a flapping wing during hover. As a result of this it is important to take the deformation of the wings into account when designing an MAV. Overall it is seen that the deforming center case creates a higher C_L compared to the other cases and reduces the negative effects of interaction with the previously shed LEV. As a result of this, designing a wing prone to deform in such a way will likely be beneficial to its performance.

Table of Contents

Preface v

Abstract vii

List of Figures xiii

List of Tables xix

List of Symbols xxi

1 Introduction 1

2 Aerodynamic mechanisms in flapping flight 5

2.1 Stable leading edge vortex and delayed stall 5

2.2 Rotational lift 6

2.3 Wake capture and added mass effect 7

2.4 Clap and fling 8

2.5 Interaction between mechanisms 9

3 Governing equations and solver 13

3.1 Immersed Boundary Methods 13

3.2 IBM method 14

3.3 Boundary reconstruction . . . 15
3.4 Spurious force oscillations in IBMs . . . 16

4 Validation **19**
4.1 Spurious fluctuations . . . 19
4.2 Kim and Gharib experiment . . . 22
4.2.1 Steady plate with impulsively started inflow . . . 24
4.2.2 Impulsively started flat plate with zero inflow . . . 29
4.3 Grid and time step study . . . 30
4.3.1 Steady plate . . . 30
4.3.2 Moving plate . . . 30
4.3.3 Influence of plate thickness . . . 32

5 Set-up of simulations **35**
5.1 Wing model . . . 35
5.2 Chordwise deformation patterns . . . 36
5.2.1 Rigid case with rotation . . . 37
5.2.2 Deforming end . . . 37
5.2.3 Deforming center . . . 39
5.2.4 Elongation of arc length . . . 39
5.3 Performed simulations . . . 40
5.3.1 Spanwise constant deformation . . . 40
5.3.2 Spanwise varying deformation . . . 40
5.3.3 Distance to symmetry plane . . . 41
5.4 Grid size . . . 42

6 Results **45**
6.1 Spanwise constant deformation . . . 45

6.2 Spanwise varying deformation . . . 52
6.3 Effect of distance to symmetry plane . . . 59
6.3.1 Rigid case . . . 59
6.3.2 Deforming center case . . . 61
6.3.3 Effect of deformation . . . 62
6.4 Peak timing . . . 63

7 Conclusions and Recommendations 73
7.1 Conclusions . . . 73
7.1.1 Validation . . . 73
7.1.2 Simulation results . . . 74
7.2 Recommendations . . . 75

A Interpolation points method 83
A.1 Function input . . . 83
A.2 Determining the cuboids boundaries . . . 83
A.3 Determining surface slopes and angles . . . 84
A.4 Limitations . . . 87

B Extra figures for results 89
B.1 Extra figures for Section 6.1 . . . 89
B.2 Extra figures for Section 6.2 . . . 93
B.3 Extra figures for Section 6.3 . . . 96
B.4 Extra figures for Section 6.4 . . . 97

List of Figures

1.1 DelFly I (50 cm span, 21.00g), DelFly II (28 cm span, 16.07g) and DelFly Micro (10 cm span, 3.07g). Copied from de Croon et al. (2009). 2

2.1 Separation of rotational lift and total lift. The red trace indicates measured lift, and the blue trace represents the estimated translational component. Rotational circulation is the difference between the measured and predicted values. White dots indicate lift transients attributed to wake capture, black dots indicate transients attributed to rotational circulation. Copied from Dickinson et al. (1999). 7

2.2 Clap and fling as redrawn from Weish-Fogh (1973) in Miller and Peskin (2004). The three-dimensional motion (top) and the corresponding two-dimensional approximation (bottom). In this drawing, the insect flies with its body oriented almost vertically, and the wings move in a horizontal plane. At the beginning of the upstroke (A), the wings move from the ventral to the dorsal side of the body, and rotate together about the leading edges. At the beginning of the downstroke (B), the wings rotate apart about the trailing edges. Towards the end of rotation, the wings translate away from each other. 10

2.3 Comparison of the lift coefficient obtained in (Kolomenskiy et al., 2009) (solid and dashed lines) with the corresponding curve in (Miller and Peskin, 2004) (dash-dot). The spacing between the wing centerlines equals c/6 during the near clapfling. During the full clapfling there is no spacing between the wings. Copied from (Kolomenskiy et al., 2009) 11

3.1 Conventional and non-body conforming grids as used in CFD simulations. 14

3.2 Two-dimensional examples of the interpolation and extrapolation method. Taken from (Luo et al., 2012) 16

4.1 The non-uniform grid used in the simulations at $\mathcal{R}e = 100$. 20

4.2 Force response of a moving flat plate using the IB solver. 20

4.3 Single-sided amplitude spectrum of fluctuations for $\Delta t = 0.002$ and $\Delta x = 0.012$. 21

4.4 Force responses for different Δt and Δx. 21

4.5 Fluctuation amplitudes at a) different minimum cell size, and b) different time steps. 22

4.6 (a) Experimental setup. White lines are the edges of the plate model. (b) Details of the mechanical model from the camera view. The arrow indicates the moving direction of a traverse. Taken from Kim and Gharib (2011). 23

4.7 Velocity profile of the inflow used in the simulations with a steady plate. 23

4.8 The non-uniform grid used in the steady simulations along with a close-up. . . . 25

4.9 The drag force vs formation time for the steady plate for $\Delta x = 0.009$ and $\Delta t = 0.0005$and the experimental result. 25

4.10 Contour plots of vorticity magnitude at half span at **T**=3.3. 26

4.11 Front view of vorticity magnitude isosurfaces with $|\omega| = 3$ from simulation and experiment. Experimental results taken from Kim and Gharib (2011) 27

4.12 Side view of vorticity magnitude isosurfaces with $|\omega| = 3$ from simulation and experiment. Experimental results taken from Kim and Gharib (2011) 28

4.13 The non-uniform grid used in the simulations with a moving body along with a close up. 29

4.14 C_D response of the moving plate along with its averaged value, compared to the response of the steady plate with inflow. 30

4.15 C_D vs formation time for the steady plate for Δx=0.012, 0.009 and 0.006. . . . 31

4.16 The drag force vs formation time for the steady plate for Δx=0.009 at Δt=0.0005 and 0.00025. 31

4.17 Averaged and non-averaged C_D vs formation time plot of the moving plate. . . . 32

4.18 The drag force vs formation time for the steady plate for Δx=0.006 at h =0.06 and h =0.038 33

5.1 Three-dimensional view of the flapping motion. 36

5.2 Top view of the flapping motion. 37

5.3 Definition of chord for the rigid case. 38

5.4 Shape of the chord for the deforming end case. 38

5.5 Shape of the chord for the deforming center case. 39

5.6 Three dimensional overview of the instrokes of the spanwise constant deforming cases. 41

5.7 Three dimensional overview of the instrokes of the spanwise varying deforming cases. 42

5.8 The non-uniform grid used for the deforming chord simulations. 43

6.1 C_L and C_D plot for the spanwise constant deforming cases. The motion starts with an outstroke. 46

6.2 C_L/C_D plot for the spanwise constant deforming cases. The motion starts with an outstroke. 46

6.3 Pressure contours of the lower surface for the spanwise constant rigid case at a) T=0.12 with the wingtip located at the left side and b) T=0.60 with the wingtip located at the right side. 47

6.4 Pressure contours of the lower surface for the spanwise constant deforming center case at a) T=0.12 with the wingtip located at the left side and b) T=0.60 with the wingtip located at the right side. 48

6.5 Pressure contours of the lower surface for the spanwise constant deforming end case at a) T=0.12 with the wingtip located at the left side and b) T=0.60 with the wingtip located at the right side. 48

6.6 Contour plots of the Q criterion at 50% span, for the spanwise constant deformation cases. On the left side the rigid case, in the middle the deforming center case and on the right side the deforming end case. 50

6.7 Pressure contours of the lower surface for the spanwise constant deforming cases at T=0.28. a) rigid case, deforming center, c) deforming end. 51

6.8 Pressure contours of the upper surfaces for the spanwise constant deforming cases at T=0.28. a) rigid case, deforming center, c) deforming end. 51

6.9 C_L and C_D plot for the spanwise varying deformation cases. The motion starts with an outstroke. 52

6.10 C_L/C_D plot for the spanwise varying deformation cases. The motion starts with an outstroke. 53

6.11 Pressure contours of the lower surfaces for the spanwise varying deforming cases at T=0.28. a) rigid case, b) deforming center, c) deforming end. 53

6.12 Pressure contours of the upper surfaces for the spanwise varying deforming cases at T=0.28. a) rigid case, b) deforming center, c) deforming end. 54

6.13 Pressure isosurfaces of $p = -1.5$ near the tip for the spanwise varying deforming cases at T=0.28. 55

6.14 Contour plots of the Q criterion at 50% span, for the spanwise varying deformation cases during the instroke. On the left side the rigid case, in the middle the deforming center case and on the right side the deforming end case. 56

6.15 Pressure isosurfaces of p=-1 during the instroke. On the left side the rigid case, in the middle the deforming center case and on the right side the deforming end case. 57

6.16 C_Ls of the three cases during initial outstroke. 58

6.17 Velocity vectors showing the effect of the interaction of the LEV. Left without interaction, and right with interaction. 58

6.18 Lift and drag coefficient plot for the spanwise varying rigid cases, at different distances from the symmetry plane. The motion starts with an outstroke. 59

6.19 C_L/C_D plot for the spanwise varying rigid cases, at different distances from the symmetry plane. The motion starts with an outstroke. 60

6.20 Lift and drag coefficient plot for the spanwise varying deforming center cases, at different distances from the symmetry plane. The motion starts with an outstroke. 61

6.21 C_L/C_D plot for the spanwise varying deforming center cases, at different distances from the symmetry plane. 61

6.22 Contour plots of Q criterion for the spanwise varying cases at different distances from the symmetry plane at 50% span. Left without symmetry plane, in the center at **D**=0.50c and right at **D**=0.25c. 65

6.23 Side view of the isosurfaces of the pressure with $p = -2$ for the spanwise varying rigid cases at various distances from the symmetry plane. Left without symmetry plane, in the center at **D**=0.50c and right at **D**=0.25c. 66

6.24 Isosurfaces of the pressure with $p = -2$ for the spanwise varying deforming center cases at various distances from the symmetry plane. Left without symmetry plane, in the center at **D**=0.50c and right at **D**=0.25c. 67

6.25 Side view of the isosurfaces of the pressure with $p = -2$ for the spanwise varying rigid cases at various distances from the symmetry plane. Left without symmetry plane, in the center at **D**=0.50c and right at **D**=0.25c. 69

6.26 Side view of the isosurfaces of the pressure with $p = -2$ for the spanwise varying deforming center cases at various distances from the symmetry plane. Left without symmetry plane, in the center at **D**=0.50c and right at **D**=0.25c. 70

6.27 Isosurfaces of the pressure where $p = -2$ for the spanwise varying deforming end case at different times. a) T=0.204, b) T=0.280, c) T=0.319. 71

6.28 Isosurfaces of the pressure with $p = -2$ at T=0.28 for the spanwise constant cases on the top, and the spanwise varying cases on the bottom, all at distance to the symmetry plane of **D**=0.50c. Left the rigid cases, in the center the deforming center cases and at the right deforming end cases. 71

A.1 Order in which the corner coordinates should be given to the function. 84

A.2 Example situation in which to find the z coordinate of the surface at the x and y coordinates of points E and F. 85

A.3 Example with surface rotated around z axis. 86

A.4 Example with surface rotated around y axis. 87

B.1 Full C_L and C_D response plot for the spanwise constant deforming cases. The coefficients are not corrected for the chord elongation. 89

B.2 Contour plots of the Q criterion at 75% span, for the spanwise constant deformation cases. On the left side the rigid case, in the middle the deforming center case and on the right side the deforming end case. 90

B.3 Contour plots of the Q criterion at 90% span, for the spanwise varying deforming cases. On the left side the rigid case, in the middle the deforming center case and on the right side the deforming end case. 91

B.4 Pressure isosurfaces of p=-1 during the instroke for the spanwise constant cases. On the left side the rigid case, in the middle the deforming center case and on the right side the deforming end case. 92

B.5 Full C_L and C_D response plot for the spanwise constant varying cases. The coefficients are not corrected for the chord elongation. 93

B.6 Contour plots of the Q criterion at 75% span, for the spanwise varying deformation cases during the instroke. On the left side the rigid case, in the middle the deforming center case and on the right side the deforming end case. 94

B.7 Contour plots of the Q criterion at 90% span, for the spanwise varying deformation cases during the instroke. On the left side the rigid case, in the middle the deforming center case and on the right side the deforming end case. 95

B.8 Lift and drag coefficient plot for the spanwise varying deforming center case without symmetry plane. The coefficients are not corrected for the chord elongation. . . . 96

B.9 Contour plots of Q criterion for the spanwise varying cases at different distances from the symmetry plane at 75% span. Left without symmetry plane, in the center at **D**=0.50c and right at **D**=0.25c. 98

List of Tables

4.1 Experiment parameters as used in Kim and Gharib (2011) and simulations. . . . 23

5.1 Parameters of the simulations 36

5.2 Non-dimensionalized parameters for the spanwise constant deforming cases. . . . 41

6.1 Cycle averaged values of the force coefficients for the spanwise constant cases. . 46

6.2 Cycle averaged values of the force coefficients for the spanwise varying cases, as well as the spanwise constant cases copied from Table 6.1. 52

6.3 Difference in force coefficients with varying distance to the symmetry plane for the rigid and deforming center case. 62

6.4 Timing of C_L peak during outstroke for all cases along with the associated value of C_L. 63

List of Symbols

Abbreviations

AB2	Adam-Bashforth second order
CN2	Fully implicit Crank-Nicolson
FSI	Fluid Structure Interaction
IBM	Immersed Boundary Method
LEV	Leading Edge Vortex
MAV	Micro Aerial Vehicle
TEV	Trailing Edge Vortex
TU Delft	Delft University of Technology
TV	Tip Vortex

Greek Symbols

α	Rotation angle around leading edge
Δt	Timestep
Δx	Cell size
δ	Deformation
ν	Kinematic viscosity
ω	Vorticity magnitude
ρ	Fluid density
θ	Flapping angle

Roman Symbols

AR	Aspect Ratio
fc	Forcing term
$\mathcal{R}e$	Reynolds number
$\mathbf{D}$	Distance to symmetry plane
C	Coefficient
c	Chord length
C_D	Drag coefficient
C_L	Lift coefficient
C_L/C_D	Lift over drag ratio
D^{max}	Maximal deformation

f	Frequency
F_i	Total force
h	Plate thickness
k	Reduced frequency
L	Length
p	Pressure
S	Surface area
t	Time
U	Plate velocity
u	Flow velocity
T	Non-dimensional time

Superscripts

max	Maximal value

Subscripts

$center$	Deforming center case
end	Deforming end case
ext	Extended
f	Fluid
max	Maximal value
n	Time step number

Chapter 1

Introduction

Micro aerial vehicles (MAVs) have the potential to play an important role in future information gathering missions, in areas such as search and rescue, environmental monitoring and security (Shyy et al., 2010). To be able to perform missions in different circumstances these MAVs should be small, maneuverable, controllable and have a broad flight envelope (Groen, 2010). The Reynolds number range at which MAVs will operate and the desired flight performance mean the vehicles require flapping flight propulsion, since fixed-wing aircraft do not have the desired maneuverability and helicopters are too inefficient and noisy (Ansari et al., 2009). This causes designers to look to nature for inspiration, since insects are extremely maneuverable, silent and much more efficient at low flight speeds (Ellington, 1999; Zbikowski, 2002). An example of an insect inspired MAV is the DelFly project by the Delft University of Technology (TU Delft), with some of the resulting designs shown in Figure 1.1. Mimicking insect flight poses a number of challenges however, both technically, and due to a lack of understanding of the fundamental aerodynamics behind the flight capabilities (Sane, 2003; Lehmann, 2008). Insect flight is very different from that of fixed wing aircraft or rotorcraft, since it relies on the use of unsteady aerodynamic mechanisms to generate sufficient lift force. In free flying red admiral butterflies the unsteady mechanisms that were observed are wake capture, a stable leading-edge vortex (LEV), clap and fling and use of rotational mechanisms. Different aerodynamic mechanisms were used in successive strokes, which leads to the conclusion that no single mechanism can be pointed out as the key to the aerodynamic capabilities of flying insects (Srygley and Thomas, 2002). Instead, insects rely on a wide range of mechanisms to maneuver, take-off, hover and land, with some insects using all mentioned mechanisms, some only one and others only use unsteady mechanisms for carrying loads or during special maneuvers (Lehmann, 2008).

Biologist have been interested in the flying capabilities of insects for a long time and have conducted many experiments using tethered insects (Ellington et al., 1996), free flying insects (Srygley and Thomas, 2002) and dynamically scaled mechanical flappers (Ellington et al., 1996; Dickinson et al., 1999; Lehmann and Pick, 2007). Particularly the experiments with a mechanical flapper have produced some very interesting results for MAV designers, including

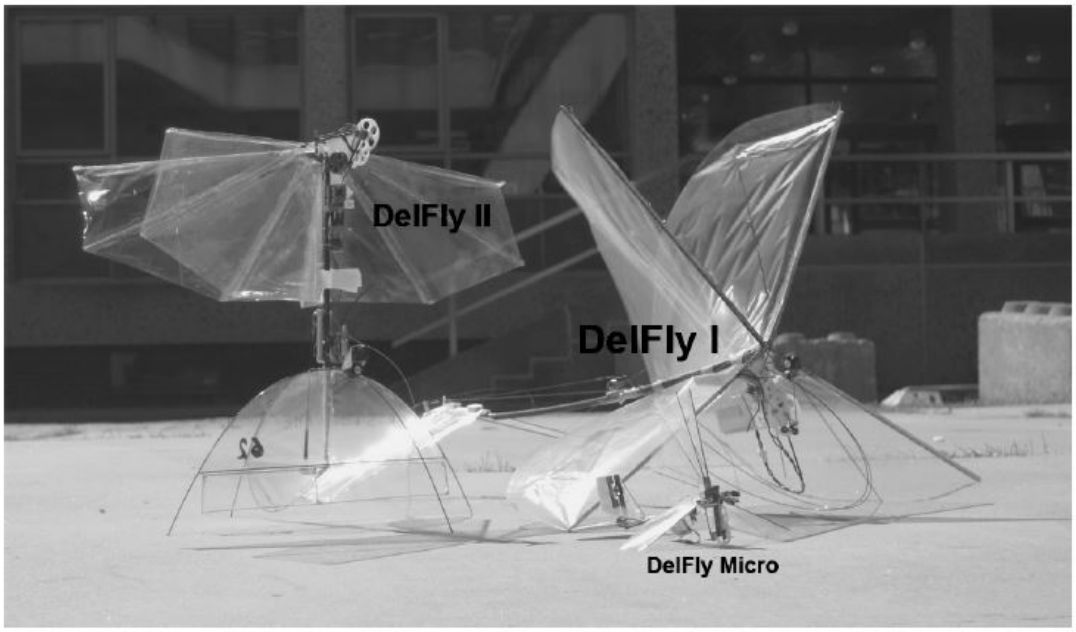

Figure 1.1: DelFly I (50 cm span, 21.00g), DelFly II (28 cm span, 16.07g) and DelFly Micro (10 cm span, 3.07g). Copied from de Croon et al. (2009).

optimal stroke trajectory (Dickinson et al., 1999; Wang et al., 2003), the effect of wing planform (Usherwood and Ellington, 2002a) and leading edge design (Usherwood and Ellington, 2002b). To completely understand the effect of all parameters however, it is essential to quantify and visualize the three-dimensional flow around the wings. Although recent developments in non-intrusive measurement techniques allow researchers to capture three dimensional flow fields (David et al., 2012; Kim et al., 2013), it remains very difficult to capture all relevant details of the flow using only experimental techniques. To get a more detailed overview of the relevant flow phenomena, numerical simulations can be performed (Wang, 2000). Several three-dimensional simulations have been performed on specific insect geometries, however, the computational requirements of such simulations are too demanding to do a systematic parametric study of all the important parameters involved (van Oudheusden, 2009). A very detailed three dimensional study on the effect of flexibility on the performance of a hawkmoth wing has been performed for example (Nakata and Liu, 2012), but this study is so specific, including vein distribution and anisotropy of the wing, that its results are hard to generalize.

This study aims to perform a three-dimensional simulation of hovering flapping wings to investigate the effects of chordwise deformation on the unsteady aerodynamic mechanisms found in flapping flight. This will result in a better understanding of the physics involved in flapping flight, which in turn could lead to improved MAV designs. Since the actual three-dimensional deformation of both insect and MAV wings is very specific to the wings' structural and material properties, this study does not include fluid-structure interaction, instead prescribing the time dependent deformation of the wings directly. That said, the configuration of the wings that will be simulated is based on a wing pair as found on a four-winged MAV in biplane configuration. This means the wings will rotate in opposing phase

around a point at the leading edge root. In such cases the flow around one wing will be affected by the presence of the other wing. The effect of the wings on one another will be simulated by creating a symmetry plane, and investigated by varying the distances to the symmetry plane. Only deformation in chordwise direction will be investigated in this study, with the wing considered fully rigid in spanwise direction. However, for several cases the chordwise deformation will be varied along the span, resulting in a twist in spanwise direction.

To perform the simulations a three-dimensional immersed boundary method (IBM) with a discrete forcing approach will be used. A big challenge with simulating flapping wings is the large translation and rotation of the wings. In conventional body conforming grid simulations these large movements result in large grid deformations, which causes problems in convergence and stability of the algorithms, as well as having a negative impact on the accuracy (Fadlun et al., 2000). IBMs that employ a non-body conforming grid have been used successfully to deal with large translations in two-dimensional simulations (Miller and Peskin, 2004, 2009), and have also been extended to three-dimensional studies (Balaras, 2004; Zhang et al., 2013; Tay et al., 2014).

Chapter 2 will discuss the unsteady aerodynamic mechanisms found in flapping flight and the parameters that are known to affect them. Chapter 3 will discuss the governing equations and how they are discretized using the immersed boundary method. Next, Chapter 4 will show the validation of the solver. Chapter 5 will discuss the set-up of the simulations, discussing the different motions and deformations that will be examined. The results of the simulations are shown in Chapter 6 and finally conclusions will be drawn in Chapter 7.

Chapter 2

Aerodynamic mechanisms in flapping flight

Flying insects have some impressive aerodynamic capabilities that cannot be explained by conventional steady aerodynamic theory. The conventional theory on how wings generate lift is based on a rigid wing moving through a fluid. However, in steady windtunnel tests on insect wings these wings cannot generate enough lift to support the insect weight, let alone the extra lift required for the special maneuvers shown by some insects. Insects therefore must use unsteady aerodynamic mechanisms to generate the lift required for insect flight (Dickinson et al., 1999). The wing stroke of insects is considered to consist of flapping motion, lead-lag motion and feathering motion around a spanwise axis. Although these motions are not actually independent they can basically be treated as a combination of heaving (also referred to as plunging) normal to the chord, swaying motion parallel to the chord, and pitching (Okamoto and Azuma, 2005), and all unsteady mechanisms should be caused by one or a combination of these motions. The different unsteady aerodynamic mechanisms that are observed in insect flight are wake capture, a stable leading edge vortex, clap and fling, clap and fling and the use of rotational mechanisms. This chapter will explain these different mechanisms and some of the parameters that are known to affect them.

2.1 Stable leading edge vortex and delayed stall

The first mechanism that will be discussed is the stable leading edge vortex (LEV) observed over insect wings, which is often regarded as the most important of all the unsteady mechanisms identified for flapping flight (Sudhakar and Vengadesan, 2010). Insects create a large LEV by flapping their wings at a very high angle of attack. This strong vortex is capable of creating a very high lift (Lehmann, 2008). A normal translating wing would shed the LEV when the angle of attack becomes too large. Insect wings however, do not show shedding at angles of attack much higher than ordinary translating wings. There are two different theories for why the LEV does not shed during the flapping of insect wings. Over a normal translating wing, at a high angle of attack, the vortex increases in size until it is shed and the wing stalls, causing a loss in lift. Before stall however, the presence of the strong attached LEV produces

very high lift. This process is called delayed, or dynamic stall. The first possible explanation for the stable LEV is that the stroke amplitude of insects is small enough to avoid shedding, but that if the stroke amplitude would become larger shedding would occur (Sane, 2003).

The other explanation is that the LEV is stabilized by the rotation of the wing. Instead of just translating their wings through the air, insects also rotate their wings around their body. This rotation causes a strong spanwise flow that stabilizes the LEV, which explains why it does not shed. In this case the stable vortex is simply a steady aerodynamic mechanism, caused by three-dimensional flow (Usherwood and Ellington, 2002a). It is important to note that the stabilizing effect of the axial flow on the LEV is not subject of debate (van den Berg and Ellington, 1997), but instead whether this mechanism is sufficient to explain the stable LEV observed in flying insects, or that dynamic stall is also required.

Parameters affecting the stability of the leading edge vortex

The stabilizing effect of the wing rotation on the LEV is independent of Reynolds number but instead governed by the aspect ratio of a single wing. Theoretically all flapping wings with a single wing aspect ratio of 3 or lower should be able to produce a stable LEV (Lentink and Dickinson, 2009). The camber of the wing, thickness of the leading edge and twist of the wing only have a small, if any, influence on the force production and stability of the LEV (Usherwood and Ellington, 2002a). The flexibility of the wing affects the strength of the LEV. When the wing is more flexible, the increased bending will lower the effective angle of attack, leading to a weaker LEV (Gillebaart et al., 2011). Since the strength of the LEV also influences the stability, a more flexible wing could also result in a more stable vortex (Yin and Luo, 2010; Eldredge et al., 2010a). However very flexible wings will suffer from premature detachment (Eldredge et al., 2010b). Finally the kinematics of the wing also affect the stability of the LEV (Trizila et al., 2011).

2.2 Rotational lift

Lift force measurements on a flapping wing show two force peaks when the wing rotates around its spanwise axis and reverses direction, as shown in Figure 2.1. When the wing does not rotate these peaks are absent, meaning the rotating of the wing generates these extra peaks in lift force (Dickinson et al., 1999). The first peak occurs when the wing is rapidly pitching around the spanwise axis, and the timing and sign of the peak are a function of the the timing of the wing rotation. The extra generated lift related to the first peak is called rotational lift. The lift peak attributed to rotational lift can be attributed to either one of three separate mechanisms, or a combination of the three. One explanation for the extra lift is that the wings own rotation serves as a source of circulation to generate the upward force. Although this force has been compared to the Magnus effect (Dickinson et al., 1999), rotational circulation is not akin to this effect (Lehmann, 2004), and is in fact a separate mechanism. Rotating wings might experience both rotational and Magnus circulation, however, including the Magnus force makes the prediction of some analytical models worse, and is possibly not important for rotational lift at all (Walker, 2002). A third contribution to the extra lift found

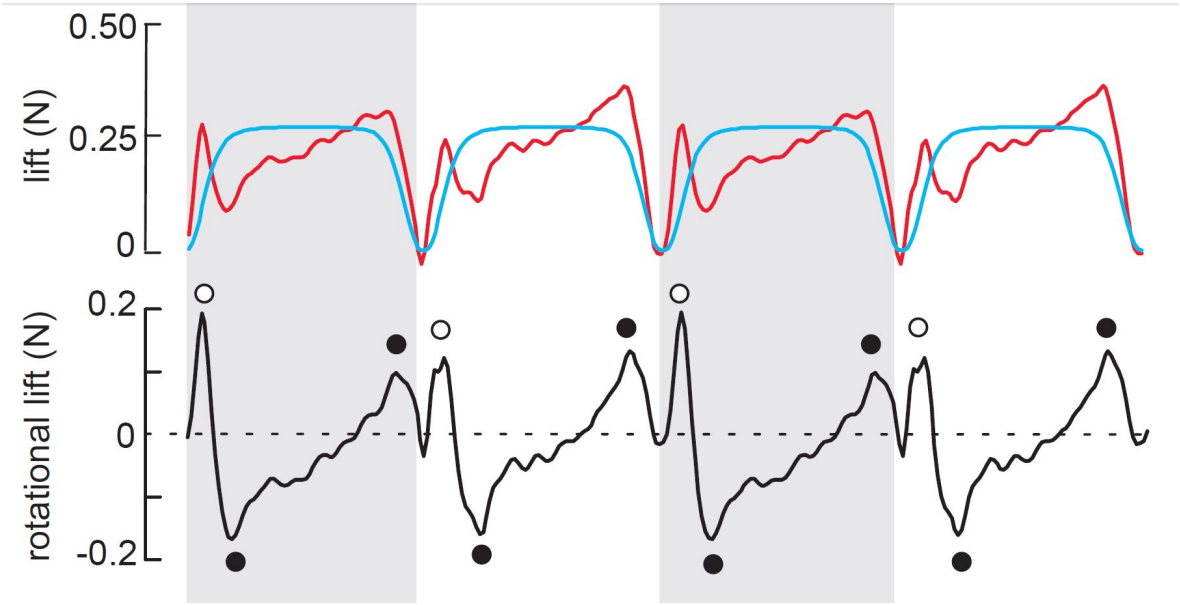

Figure 2.1: Separation of rotational lift and total lift. The red trace indicates measured lift, and the blue trace represents the estimated translational component. Rotational circulation is the difference between the measured and predicted values. White dots indicate lift transients attributed to wake capture, black dots indicate transients attributed to rotational circulation. Copied from Dickinson et al. (1999).

during wing rotation is the wings ability to delay stall during translation (Lehmann, 2004). Kramer (as cited in Lehmann (2004)) has shown that a wing in steady motion can experience lift coefficient above the steady stall value when the wing is rotating slowly from low to high angles of attack. The increase in maximum lift coefficient by wing rotation is called the Kramer effect. Although these three mechanisms are sometimes referred to separately, they are often merged and referred to as either rotational forces or Kramer forces (Groen, 2010).

Parameters affecting rotational lift

As mentioned before the force peak that is attributed to rotational lift is affected by the timing of the rotation. To have the proper angle of attack, the wing must pronate before the downstroke and supinate before the upstroke. If the wing flips early the lift is increased, if the wing flips late the lift is decreased. The force of the vortex generated by a rotating wing is a function of the chordwise location of the center of rotation, and the chord length (Walker, 2002).

2.3 Wake capture and added mass effect

The position of the second force peak in Figure 2.1 is independent of the timing of the wing rotation, and cannot be explained by the rotational lift. In Dickinson et al. (1999) it is

suggested that this might be caused by the wing interacting with the vortex that was shed when the wing began to rotate. This mechanism is called wake capture. The claim that the wake interacting with the wing causes the peak in lift is supported by several experiments (Dickinson et al., 1999), and some simulations (Walker, 2002). Other simulations found that when the effect of the wake was investigated the lift coefficient was actually reduced however, and concluded that the high peak at the beginning of the stroke is not due to wake capture, but instead due to reaction of accelerating an added mass of fluid (Sun and Tang, 2002; Miller and Peskin, 2004, 2009). In other studies a distinction is made between rotational and translational added mass effects (Jardin et al., 2012), where the translational added mass has a nett effect of zero, and the rotational added mass has a positive effect on the lift. The two-dimensional simulations of Miller and Peskin (2004) and Miller and Peskin (2009) showed a negative effect caused by wake interaction, instead of an increase lift.

Parameters affecting wake capture

Although the timing of the second peak attributed to wake capture does not change with wing rotation, its amplitude does. When the wing rotation is delayed with respect to stroke reversal the angle of attack will be negative with respect to the oncoming flow, resulting in negative lift. The interaction of the wing with the previously shed vortex is of course also depending on the strength and position of the shed vortex. This means that the parameters effecting the strength and the shedding of the LEV also affect the wake capture mechanism. Gillebaart (2011) reported an increase in force due to the interaction with the wake, with the increase in force being more significant when the wing was more rigid. It is unclear how exactly the benefit of wake capture changes during fast forward or maneuvering flight of an insect when the wings experience additional fluid components produced by the animals own body motion (Lehmann, 2008).

2.4 Clap and fling

The clap and fling motion corresponds to a lift enhancing mechanism first proposed by Weis-Fogh in 1973, while studying the hovering motion of a tiny wasp (Weish-Fogh, 1973). This mechanism occurs when the wings clap together at the end of the upstroke, from ventral to dorsal, and fling apart at the beginning of the downstroke as shown in Figure 2.2. How this motion is thought to enhance lift was described analytically by Lighthill using two-dimensional inviscid theory (Lighthill, 1973) and confirmed later by experiments, although the actual produced lift proved to be higher than the value predicted by Lighthill (Maxworthy, 1979). The lift generation is augmented during fling by the formation of two large leading vortices (Miller and Peskin, 2009). The leading vortex of each wing acts as the starting vortex of the other, and being equal in size, causing the total circulation around both wings to remain zero. This means no trailing vortices are required to conserve circulation, eliminating the delay in lift buildup required by the Wagner effect. During the following translation the leading edge vortices remain attached and small trailing edge vortices are formed. However, the leading edge vortices are much stronger than the ones on the trailing edge, causing vortical asymmetry. This asymmetry leads to negative circulation, giving larger lift forces when

compared to flapping wings without fling motion in which case there the leading and trailing edge vortices will be of equal strength (Miller and Peskin, 2004; Sun and Yu, 2006). During clap two large trailing edges are formed which again are each others opposites. The large circulation causes a high lift during this phase, approximately 1.6 times as large as a single wing performing the same motion (Sun and Yu, 2003). During clap a small jet of fluid is also squeezed out of the closing gap between the trailing edges, causing a modest increase in lift (Lehmann and Pick, 2007).

Parameters affecting clap and fling

The added lift generated by the clap and fling mechanism is affected by several parameters. The first parameter has to do with the whether the wings completely touch each other. For a true 'clap' the wings have to physically touch each other, but even when there is a small gap between the wings this mechanism can create extra lift. The extra generated lift decreases with increasing gap size. When the gap becomes too large the wings do no longer influence each other and the clap and fling mechanism is said to be absent (Kolomenskiy et al., 2009). The influence of the gap size can be very important for certain simulations, in which it is not possible to make the wings completely touch each other and a small gap is always present. This effect is shown in Figure 2.3, which compares the results of (Kolomenskiy et al., 2009) and (Miller and Peskin, 2004) in which the simulation method did not allow for a 'full' clap and fling. It can be seen that the gap does not only influence the size of the lift, but also the timing of the lift creation. From research on different insects it has been discovered that although clap and fling is very common in the smallest flying insects, larger insects do not use this mechanism (Dickinson et al., 1999). A possible explanation is that the mechanism is less effective at higher Reynolds numbers (Sun and Yu, 2006).

2.5 Interaction between mechanisms

Although the mechanisms discussed in this chapter are presented as separate mechanisms, these mechanisms will affect one another, which may change their behavior. The wake of the wing will be determined by the strength of the shed leading edge vortices and the moment that they were shed. This means the stability and strength of the LEV will affect the behavior of wake interaction. This type of interaction between mechanisms will make it much harder to distinguish between the separate mechanisms and might be the reason different researchers come to different conclusions on their effects. This interaction also makes it more difficult to determine what parameters affect a mechanism. For example, the aspect ratio of the wing might not directly change the wake capture mechanism, but it changes the LEV stability which will in turn affect wake capture. Again this makes distinguishing between separate mechanisms very difficult. Research focusing on the interaction between the different mechanisms will help to explain the behavior better.

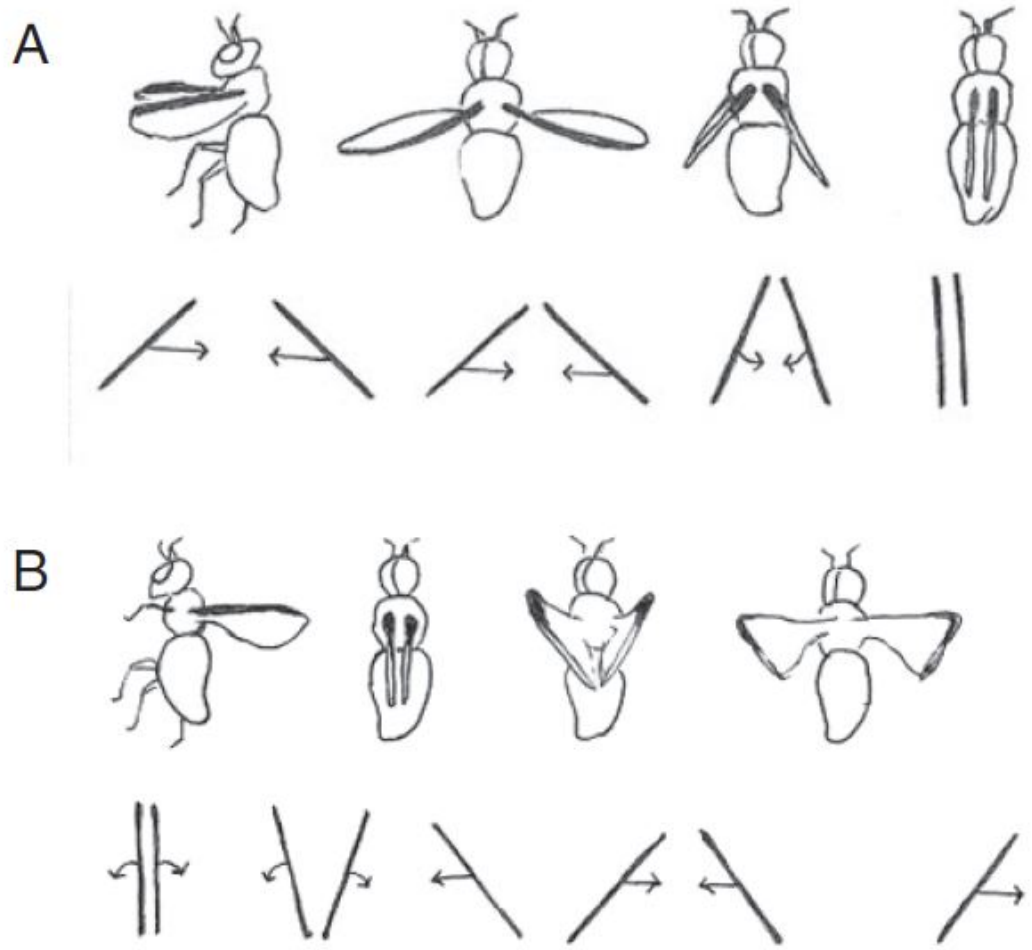

Figure 2.2: Clap and fling as redrawn from Weish-Fogh (1973) in Miller and Peskin (2004). The three-dimensional motion (top) and the corresponding two-dimensional approximation (bottom). In this drawing, the insect flies with its body oriented almost vertically, and the wings move in a horizontal plane. At the beginning of the upstroke (A), the wings move from the ventral to the dorsal side of the body, and rotate together about the leading edges. At the beginning of the downstroke (B), the wings rotate apart about the trailing edges. Towards the end of rotation, the wings translate away from each other.

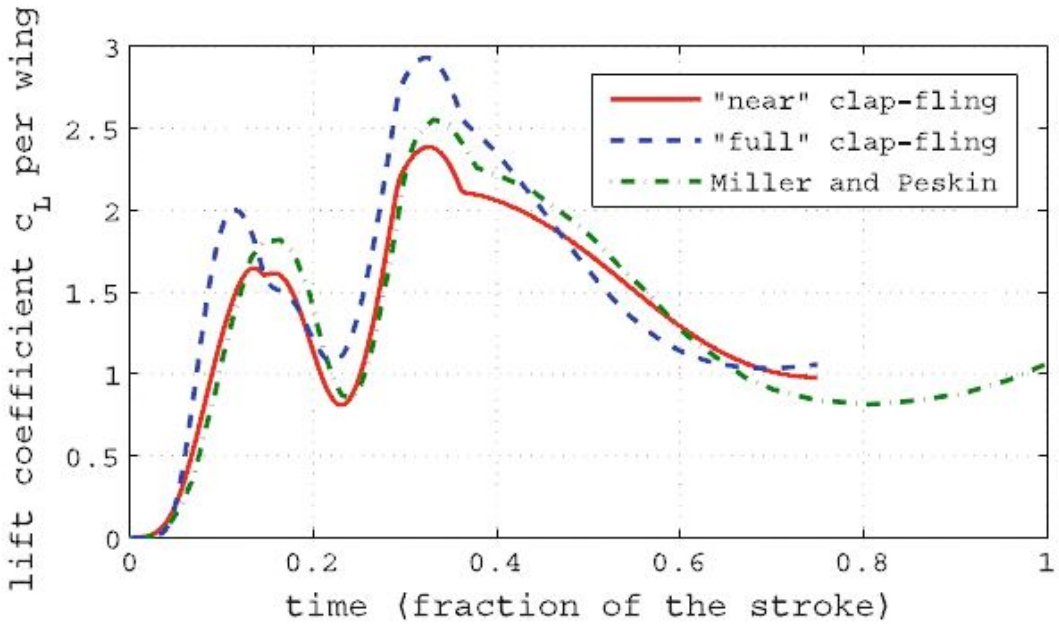

Figure 2.3: Comparison of the lift coefficient obtained in (Kolomenskiy et al., 2009) (solid and dashed lines) with the corresponding curve in (Miller and Peskin, 2004) (dash-dot). The spacing between the wing centerlines equals c/6 during the near clapfling. During the full clapfling there is no spacing between the wings. Copied from (Kolomenskiy et al., 2009)

Chapter 3

Governing equations and solver

With the ever increasing computing power and decreasing prices of modern computers, more and more complex flows can be solved. Most codes capable of handling complex geometries however, require either body-fitted curvilinear or unstructured meshes. High quality body-fitted curvilinear meshes have as disadvantage that they require a lot of specialist attention to get right, whereas unstructured meshes have negative impact on both the stability and the convergence of the algorithms (Fadlun et al., 2000). For both cases, these disadvantages become even more relevant when the simulation includes deforming or moving boundaries, which will indeed be the case for the simulations performed in this study. To avoid these issues an alternative strategy will be used in which the grid does not conform to the boundaries. Methods in which the grid does not conform to the body are referred to as immersed boundary methods (IBMs) and have several advantages over grid conforming methods. In the case of moving boundaries a very big advantage is that no redistribution of the mesh is required. Many different immersed boundary method exist with the main difference being in the way they deal with the immersed boundary. In this study a combination of the methods described by Kim et al. (2001), Yang and Balaras (2006) and Liao et al. (2010) is used. This chapter will first explain the idea behind IBMs. Next the specific method used in this study will discussed in a little more detail. Finally two important aspects in solving the system, the interpolation scheme to prescribe the boundary condition and the numerical oscillations caused by moving boundaries will be discussed.

3.1 Immersed Boundary Methods

Low Reynolds number flow is governed by the incompressible Navier-Stokes equations. The non dimensionalized form of these equations is given in Equations 3.1 and 3.2.

$$\nabla \cdot u = 0 \tag{3.1}$$

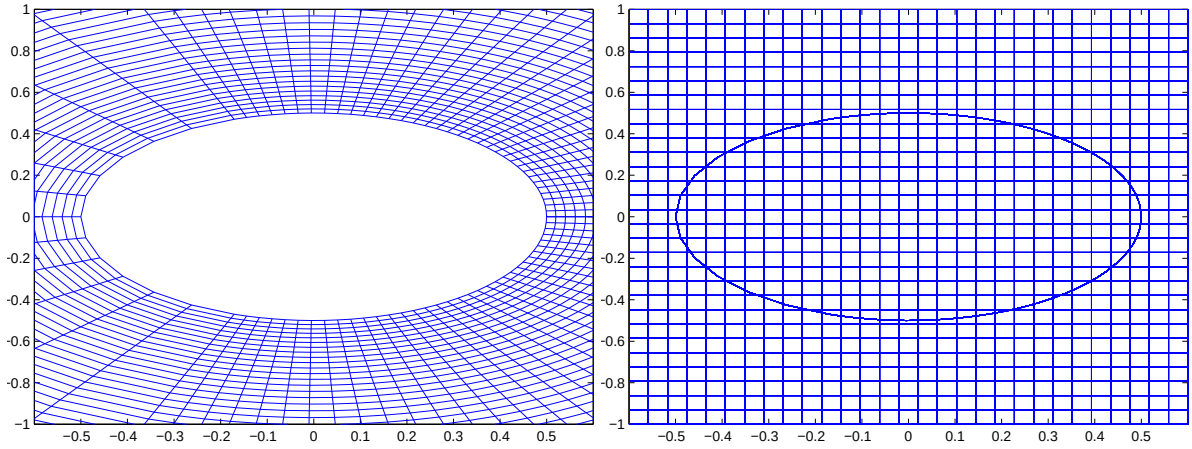

(a) Conventional grid (b) Non body conforming grid

Figure 3.1: Conventional and non-body conforming grids as used in CFD simulations.

$$\frac{\partial u}{\partial t} = -u \cdot \nabla u + \frac{1}{\mathcal{R}e}\nabla^2 u - \nabla p \tag{3.2}$$

In which u is the velocity, t is time, p is the pressure and $\mathcal{R}e$ is the Reynolds number.

A standard approach when simulating a flow around a boundary is to generate a grid conforming to that boundary, as shown in Figure 3.1a. Next, Equations 3.1 and 3.2 are discretized on this grid, and the conditions at the boundary can be prescribed directly. As mentioned in the introduction the generation of this grid can become troublesome in case of complex boundaries. When using an immersed boundary method, the grid is generated with no regard for the boundary (Mittal and Iaccarino, 2005), as shown in Figure 3.1b. Since this means the boundary conditions cannot be prescribed directly, the governing equations have to be modified to be able to include their effect. This is done by including an extra force term fc in Equation 3.2 resulting in Equation 3.3.

$$\frac{\partial u}{\partial t} = -u \cdot \nabla u + \frac{1}{\mathcal{R}e}\nabla^2 u - \nabla p + fc \tag{3.3}$$

Two different approaches can be taken to solve for Equation 3.3. The first option applies the forcing fc to the entire domain and then discretizes the equation. This approach is called the continuous forcing approach. The second approach first discretizes the equations without taking fc into account, after which the discretization in the cells near the boundaries is adjusted to account for their presence (Mittal and Iaccarino, 2005). This approach is called the discrete forcing approach. The next section will give some extra details on the approach used in this study.

3.2 IBM method

The IBM used in this study is a combination of the methods described by Kim et al. (2001), Yang and Balaras (2006) and Liao et al. (2010). In both the method by Liao et al and the one

by Yang and Balaras, the forcing term fc is calculated explicitly using an Adam-Bashforth second-order (AB2) scheme and the time integration scheme uses a semi-implicit AB2 scheme. In this study, the time integration scheme has been changed to a fully implicit Crank-Nicolson (CN2) scheme. Secondly, fc is calculated explicitly using the first-order forward Euler and second-order AB2 schemes for the viscous and convective terms, respectively. This will reduce the computational cost while having no observable difference on the results compared to an AB2 scheme (Tay et al., 2014). The forcing term fc will be calculated using Equation 3.4.

$$fc^{n+1} = \frac{u_f - u^n}{\Delta t} + \left[u^n \cdot \nabla u^n - \frac{1}{\mathcal{R}e} \nabla^2 u^n \right] + \nabla p^n \tag{3.4}$$

In this equation the superscript indicates the time step number and u_f is the velocity contribution of the boundary which has to be imposed. Since the boundary does not match the grid this velocity is not known and must be reconstructed using information from the interface and the surrounding velocity field (Yang, 2005). The reconstruction is discussed in Section 3.3. Finally the total force exerted on the surface of the solid will be calculated using fc^{n+1}, using Equation 3.5.

$$F_i = -\int_{solid} fc_i^{n+1} dV + \int_{solid} \left(\frac{\partial u_i}{\partial t} + \frac{\partial u_i u_j}{\partial x_j} \right) dV \tag{3.5}$$

3.3 Boundary reconstruction

To calculate fc the velocity u_f has to be reconstructed in the grid points near the boundary. To be able to do this it is first necessary to identify the grid points that are near the boundary. This is done by first determining for each grid point if it lies within the solid region or in the fluid region. If a point lies in the fluid region and has at least one neighboring point in the solid region it is considered a forcing point. The velocities in the forcing points will be interpolated to account for the boundary's presence. The interpolation is done using a triangle linear interpolation in three dimensions. A two-dimensional example of the interpolation method is shown in Figure 3.2a.

When simulating a moving boundary the role of grid points can change from time step to time step. Besides having to reevaluate the role of all grid points at each time step this gives rise to another issue. The time advancement scheme requires physical values of the velocities and pressures from the previous time step, as well as their derivatives. Although the velocities will be reconstructed in a forcing point, its derivatives will include grid points from inside the solid. When a point that was a forcing point in the previous time step becomes a fluid point, these non-physical derivatives can introduce spurious vorticity near the boundary, which in turn can lead to large errors (Yang, 2005). To ensure this does not occur, a field extension procedure was used in Yang and Balaras (2006). In this procedure all solid points with at least one neighboring point in the fluid are identified. The velocities and pressures in these pseudo-fluid points are extrapolated from the fluid to ensure the derivatives in the forcing

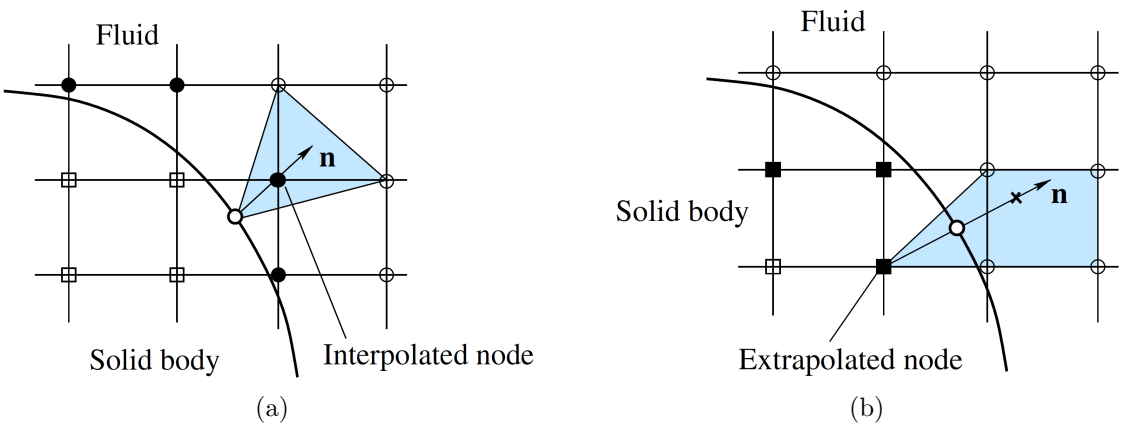

Figure 3.2: Two-dimensional examples of the interpolation and extrapolation method. Taken from (Luo et al., 2012)

points have physical values. A two dimensional example of such an extrapolation method in shown in Figure 3.2b. For this study the field extrapolation is not performed however, since experience has shown that finding the pseudo-fluid points in three dimensional simulations can become quite cumbersome, while the field extension does not help the solution.

Finding the points that can be used for the interpolation is an important step and, since this has to be done at every time step in case of moving boundaries, can become rather time consuming. A quick method to find the required points in case of a non deforming plate was written for this study, and although it was not extensively used for the final simulations a description of this method is given in Appendix A for future reference.

3.4 Spurious force oscillations in IBMs

The field extension method described in the previous section can reduce the spurious force oscillations in the solution but can not completely eliminate them (Lee et al., 2011). The reason it is not effective in this study is a second source of spurious oscillations. When the boundary moves, grid points can change their role from, or to, a forcing point. This can cause spurious oscillations, for example, when a grid point changes its role from a fluid point to a forcing point. When this happens the stencil for its calculation will change instantaneously from the finite-difference stencil for the discrete Navier-Stokes equation, to the interpolation stencil. Although both stencils are valid representations of the same flow field, their discretization errors both have their own characteristics, which in general are not consistent to each other (Luo et al., 2012). The triangle linear interpolation used has associated numerical errors of $O(\Delta x)$ and the spatial scheme used uses a scheme of $O(\Delta x)$ for the convective terms, so the difference between the schemes is expected to be of $O(\Delta x)$. This means that when the boundary crosses and a grid point switches to a forcing point this creates a temporal discontinuity in the velocities. Since the pressure is proportional to the acceleration $\frac{\partial u}{\partial t}$, the oscillation in the pressure (and thus the force) is expected to be of $O\left(\frac{\Delta x}{\Delta t}\right)$. This means that decreasing the time step will actually increase the resulting pressure oscillation. The behavior of these

fluctuations will be investigated in Chapter 4, but no changes to the solver will be made to reduce their effect.

Chapter 4

Validation

The immersed boundary solver described in Chapter 3 has been validated for two-dimensional cases in Tay et al. (2012). The same study showed a quick three-dimensional validation case of the solver at a low grid resolution at a Reynolds number of $\mathcal{R}e = 10000$ of a plunging wing, also described in Tay et al. (2014). An extra validation of the three-dimensional solver will be performed in this chapter by comparing the results to an experiment performed by Kim and Gharib (2011) at a Reynolds number of $\mathcal{R}e = 2000$. Before this is done the spurious fluctuations caused by the moving boundaries as discussed in Section 3.4 will be investigated at a Reynolds of $\mathcal{R}e = 100$. After these are investigated the solver is used to simulate the full experiment, both with and without a moving boundary, and the results are compared. Finally a grid and time step study is performed to investigate the impact of these parameters on the solution.

4.1 Spurious fluctuations

When using an immersed boundary method with discrete forcing in a simulation with moving boundaries, the solution produces spurious force oscillations on a solid body as explained in Section 3.4. To be able to distinguish these oscillations from other possible fluctuations that may have a physical meaning, their behavior in the code is examined. This is done by simulating a impulsively started flat plate with aspect ratio $AR = 1$ at a 90 degree angle with the direction of motion and moving with non-dimensional velocity $U = 1$. The corresponding Reynolds number is equal to $\mathcal{R}e = 100$. The force coefficient will be taken equal to F_i as calculated by Equation 3.5.

When generating a grid for an IBM it is standard practice to have a region of uniform grid spacing around the boundaries (Mittal and Iaccarino, 2005). When simulating a moving body it is important that the uniform region is large enough to ensure the body does not travel outside of the region, reducing the accuracy. On top of that the uniform region needs to extend to some distance behind the body to ensure the wake is resolved correctly. Outside of

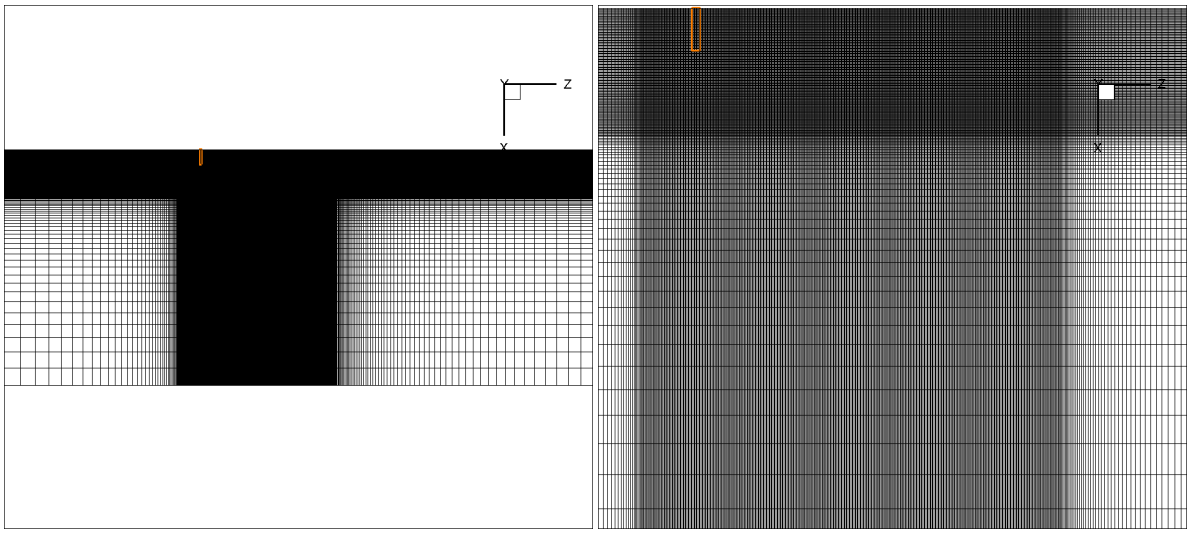

(a) (b)

Figure 4.1: The non-uniform grid used in the simulations at $\mathcal{R}e = 100$.

the uniform region the cell size increases to a fixed value according to an exponential function (Tay et al., 2012). Throughout this report cell size Δx is used to refer to the uniform cell size normalized by chord length c. The grid used is shown in Figure 4.1 with the plate moving in positive z-direction. The orange lines represent the initial position of the plate. From the figure it can be seen that the plate touches the top boundary of the domain. This boundary is a symmetry plane, and as a result only one half of the plate needs to be simulated.

Figure 4.2 shows the response in the drag coefficient C_D for a plate with a uniform cell size $\Delta x = 0.012$ and time step $\Delta t = 0.001$. The response clearly shows large fluctuations.

The cause of the fluctuations is that the boundary moves from one cell to another, causing an instantaneous change in the affected grid points as explained in Section 3.4. This can be

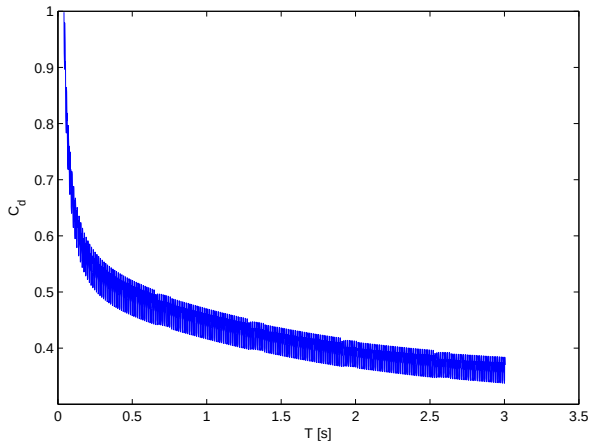

Figure 4.2: Force response of a moving flat plate using the IB solver.

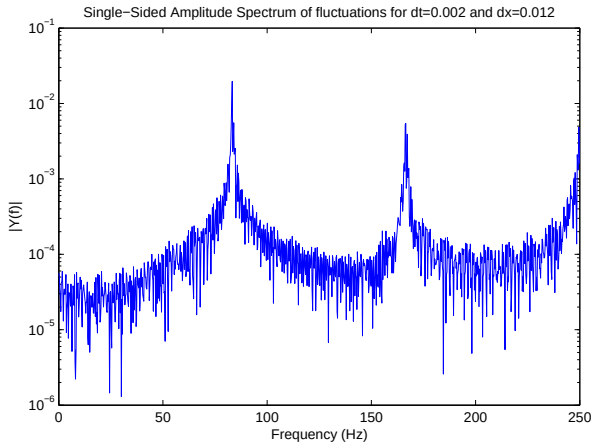

Figure 4.3: Single-sided amplitude spectrum of fluctuations for $\Delta t = 0.002$ and $\Delta x = 0.012$.

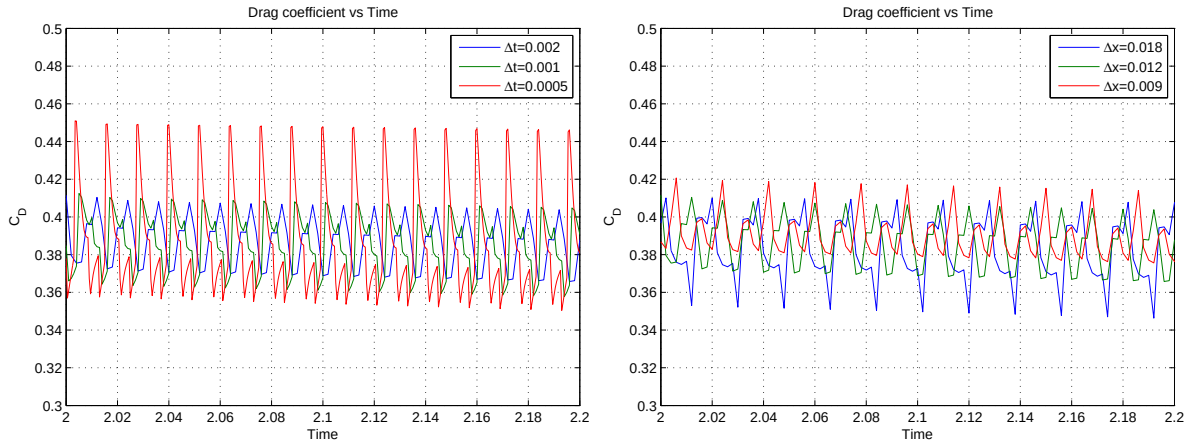

(a) $\Delta x = 0.012$,variable Δt

(b) $\Delta t = 0.002$, variable Δx

Figure 4.4: Force responses for different Δt and Δx.

clearly seen by the frequency of the fluctuations, shown in Figure 4.3. The peak in this plot is at a frequency of 83.3 and its multiples. This frequency is exactly equal to $\frac{U}{\Delta x}$, proving the relation between the fluctuations and the boundary crossing the grid points.

To investigate the behavior of the fluctuations, the simulation is redone using different time steps, Δt=0.0005, 0.001 and 0.002, and cell sizes Δx=0.009, 0.012 and 0.018. Close-ups of the results are shown in Figure 4.4.

The amplitudes in Figure 4.4 can be seen to be affected by both Δx and Δt. To visualize this effect the amplitudes for different cell sizes and time steps are shown in Figure 4.5. The plot also shows a best-fit power law trough the points from which it can be derived that the fluctuations are of order $O\left(\frac{\Delta x^{0.63}}{\Delta t^{0.45}}\right)$. This order is much lower than the expected order $O\left(\frac{\Delta x}{\Delta t}\right)$, mentioned in Section 3.4. More importantly however, the amplitude does decrease with increasing Δt and decreasing Δx. The reason the order is lower than expected is not

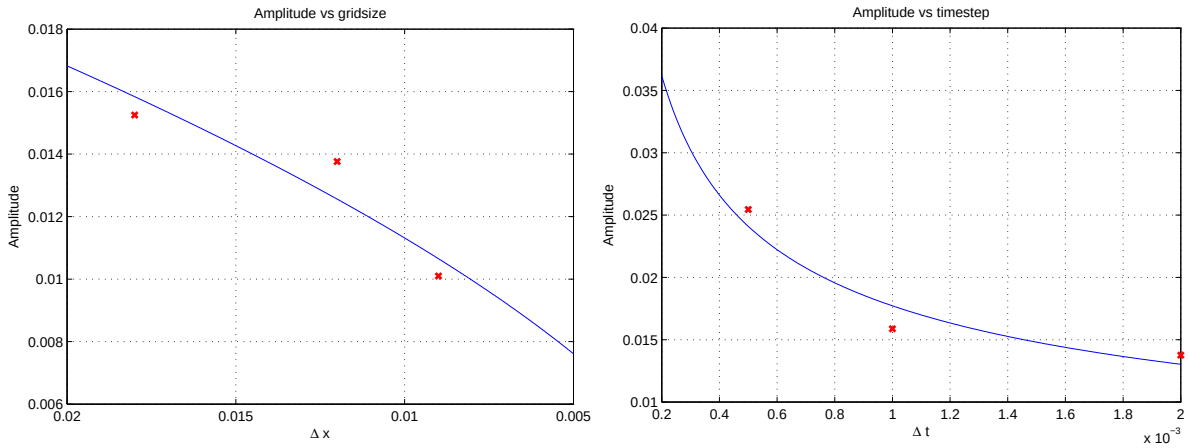

(a) (b)

Figure 4.5: Fluctuation amplitudes at a) different minimum cell size, and b) different time steps.

clear, but it is likely that a more extensive grid and time step study is required, since only 3 different grid sizes and three different time steps were used. Since no attempt will be made to reduce the fluctuations, such a grid and time step study will not be performed here.

4.2 Kim and Gharib experiment

To validate the immersed boundary solver, it will be compared to the experiment described in Kim and Gharib (2011). In this study a flat plate is accelerated from rest to a constant velocity, inside a watertank. The plate has one free end, an aspect ratio of 3.75 and is at a 90 degree angle with the direction of motion. The Reynolds number based on the final plate velocity is equal to $\mathcal{R}e = 2000$. A photograph and a sketch of the setup of the experiment are shown in Figure 4.6. The free surface of the water is considered a symmetry plane and will be modeled as such. The acceleration phase in the experiment takes 0.25 seconds, but the exact velocity profile is not specified in the original publication. Since it was not specified in the publication a velocity profile is chosen that increases smoothly. The normalized velocity profile that is chosen is given by Equation 4.1.

$$u = \frac{\sigma}{2A_c} \frac{\log\left(\cosh\left(A_c(t-t_1)\right)\right)}{\cosh\left(A_c(t-t_2)\right)} + 0.5A_{max} \tag{4.1}$$

With $\sigma = 3.2$, $t_1 = 0.1$, $t_2 = 0.4125$, $A_c = 50$ and $A_{max} = 1$. The resulting velocity is shown in Figure 4.7. From the velocity plot it can be seen that the acceleration takes slightly longer. This is done because the solver cannot deal with too sudden jumps in the acceleration, so the profile is slightly smoothened. The experiment parameters are shown in Table 4.1.

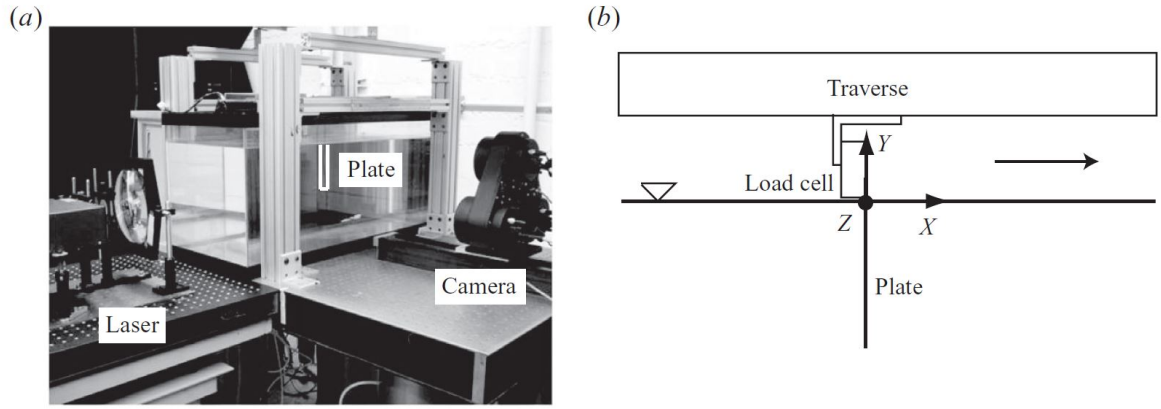

Figure 4.6: (a) Experimental setup. White lines are the edges of the plate model. (b) Details of the mechanical model from the camera view. The arrow indicates the moving direction of a traverse. Taken from Kim and Gharib (2011).

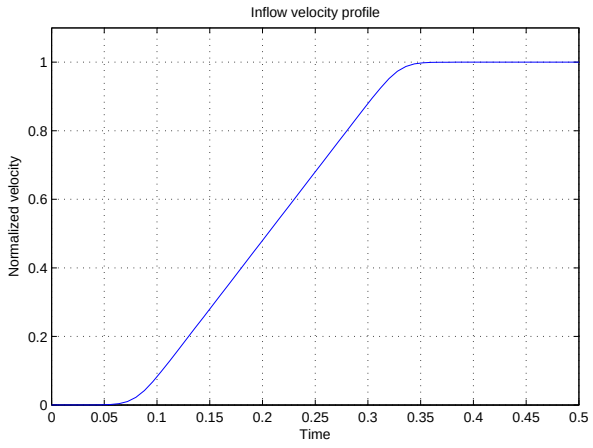

Figure 4.7: Velocity profile of the inflow used in the simulations with a steady plate.

Parameter	Value
Reynolds number based on final velocity	2000
Chord length	40 [mm]
Aspect Ratio	3.75
Final velocity	50 [mm/s]
Acceleration phase	0.25 [s]

Table 4.1: Experiment parameters as used in Kim and Gharib (2011) and simulations.

4.2.1 Steady plate with impulsively started inflow

In the first simulation a steady flat plate is used, with an accelerating inflow. Although this means the acceleration of the air around the plate will differ slightly from that set at the inflow, it will give approximately the same forces and vortex structure, limit the size of the uniform grid since no movement has to be taken into account and will eliminate the problems associated with the moving body mentioned in Section 4.1. The fact that the velocity profile will not perfectly match the experiment is not relevant because the exact profile used in the experiment is not known anyway. The plate used in the simulation has a thickness h of $0.06c$ instead of the $0.038c$ used in the experiment. This is done because experience has shown that the interpolation method used requires at least 4 grid points inside of the plate. Making the plate slightly thicker than in the experiment allows for a coarser grid while it is not expected to affect the solution significantly. This assumption will be tested in Section 4.3. The drag coefficient as used in the experiment is defined as $C_D = \frac{Drag}{1/2\rho_f U^2 S}$, in which ρ_f is the density of the water, U is the final velocity and S is the surface area of the plate. To relate C_D to the coefficients given by Equation 3.5 requires multiplying F_i with $\frac{2c^2}{S} = 0.5333$. The non-dimensional time $\mathbf{T}$ is defined in the experiment as the time it takes to travel the distance of 1 chordlength. This means $\mathbf{T}$ is given by Equation 4.2, since the velocity is not constant during the acceleration phase.

$$\mathbf{T} = \int_0^t \frac{U(t)}{c} dt \tag{4.2}$$

As mentioned in the previous section it is standard practice to have a region of uniform cell size around the simulated body. In the simulations performed in this section this would lead to an excessively large number of cells however, so the uniform region does not include the entire body for the validation cases. Instead the uniform area contains a small region around the free end of the plate. The grid used for the steady simulation is shown in Figure 4.8a, in which the orange lines represent the plate, and the flow is coming from the negative z-direction.

The drag force result of the simulation with a uniform section of $\Delta x = 0.009$ and $\Delta t = 0.0005$ is plotted in Figure 4.9 along with the result of the experiment. The initial peak in the force can be seen to be higher in the experiment. This is most likely caused by the different velocity profile used in the experiment. When the final velocity is reached the force drops in both cases, and shows another distinct hump before approaching a steady state value. After $\mathbf{T}$=1 the simulation and the experiment gradually move towards a steady state value around $C_D = 2$. The experimental final value is not exactly stated but from the plot of Figure 4.9 is estimated to be $C_D = 2.05$ while the simulated value goes to $C_D = 1.93$. This means the C_D found by the simulation is approximately 6% lower than that found by the experiment.

Next the vortices behind the flat plates are investigated. The experimental results show this by plotting the isosurface of vorticity magnitude $|\omega| = 3$, at $\mathbf{T}$= 1.3, 3.3 and 5.3. The vorticity

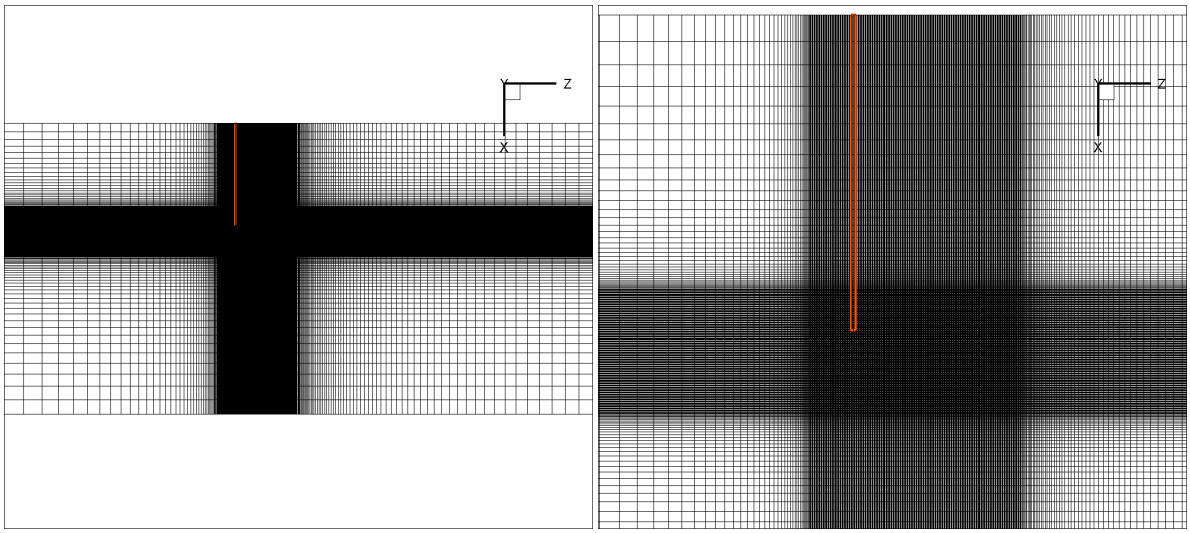

(a) (b)

Figure 4.8: The non-uniform grid used in the steady simulations along with a close-up.

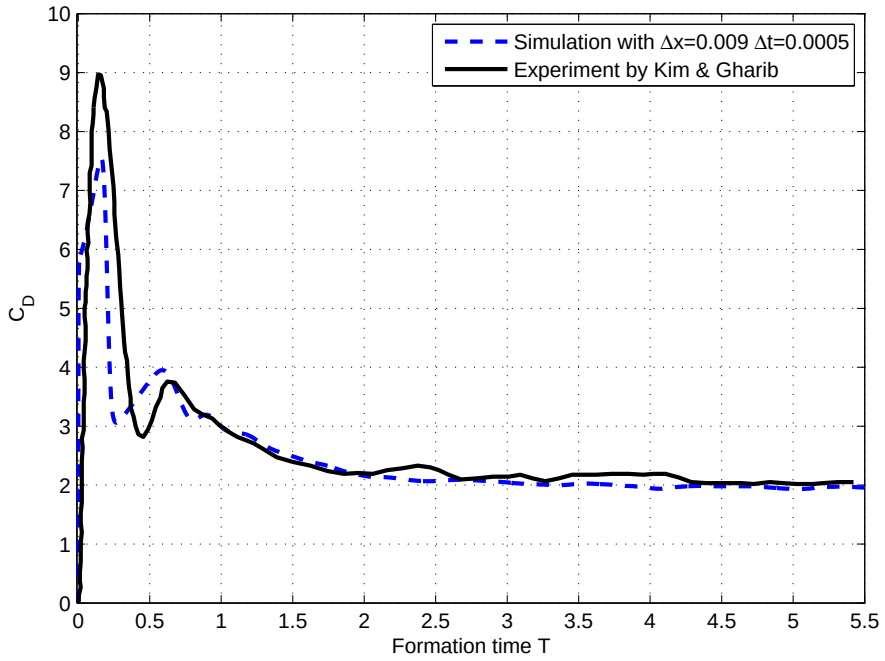

Figure 4.9: The drag force vs formation time for the steady plate for $\Delta x = 0.009$ and $\Delta t = 0.0005$and the experimental result.

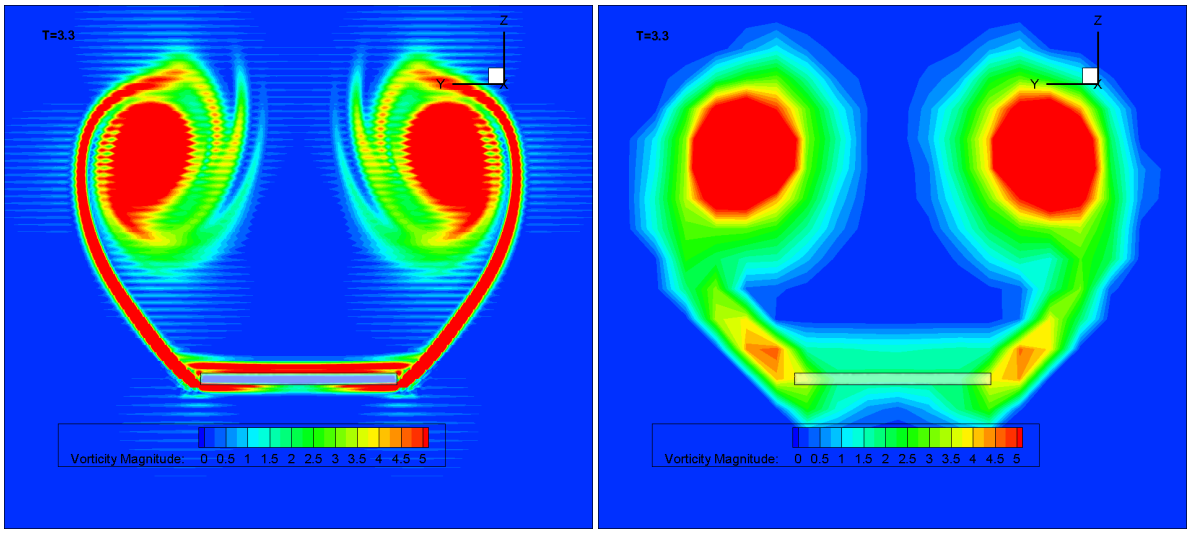

(a) Plot from simulation with Δx=0.009. (b) Interpolated plot with Δx=0.15.

Figure 4.10: Contour plots of vorticity magnitude at half span at **T**=3.3.

magnitude is given by Equation 4.3 (Anderson, 2007).

$$|\omega| = |\vec{\nabla} \times \vec{u}| \tag{4.3}$$

Where $|\omega|$ is non dimensionalized as $\omega = \frac{\omega c}{U}$.

To allow for a good comparison the resolution of the simulation is decreased to match the resolution achieved in the experiment. This means the solution is interpolated onto a uniform grid, with cell size $\Delta x = 0.15$. Matching the resolution before the comparison is non-trivial since it can have a significant effect on the flow field representation. The difference between the simulation with $\Delta x = 0.009$, and the interpolated result with $\Delta x = 0.15$ can be clearly seen from Figure 4.10. This figure shows a contour plot of the vorticity magnitude at **T**=3.3 at half the span. The narrow region of high vorticity leading from the edges of the plate seen in the original image is smoothed out due to the interpolation. Since this region cannot be represented in the experiment comparing the isosurfaces to the simulation directly would be much harder to do.

The isosurfaces of $|\omega| = 3$ from the interpolated results are shown in Figure 4.11 and 4.12. In the same figures the results from the experiment are shown as well. The results from the experiments are averaged over several runs, explaining the smoother appearance of the vortices. Apart from the smoother experimental results the vortex structures are very similar and no important differences can be identified.

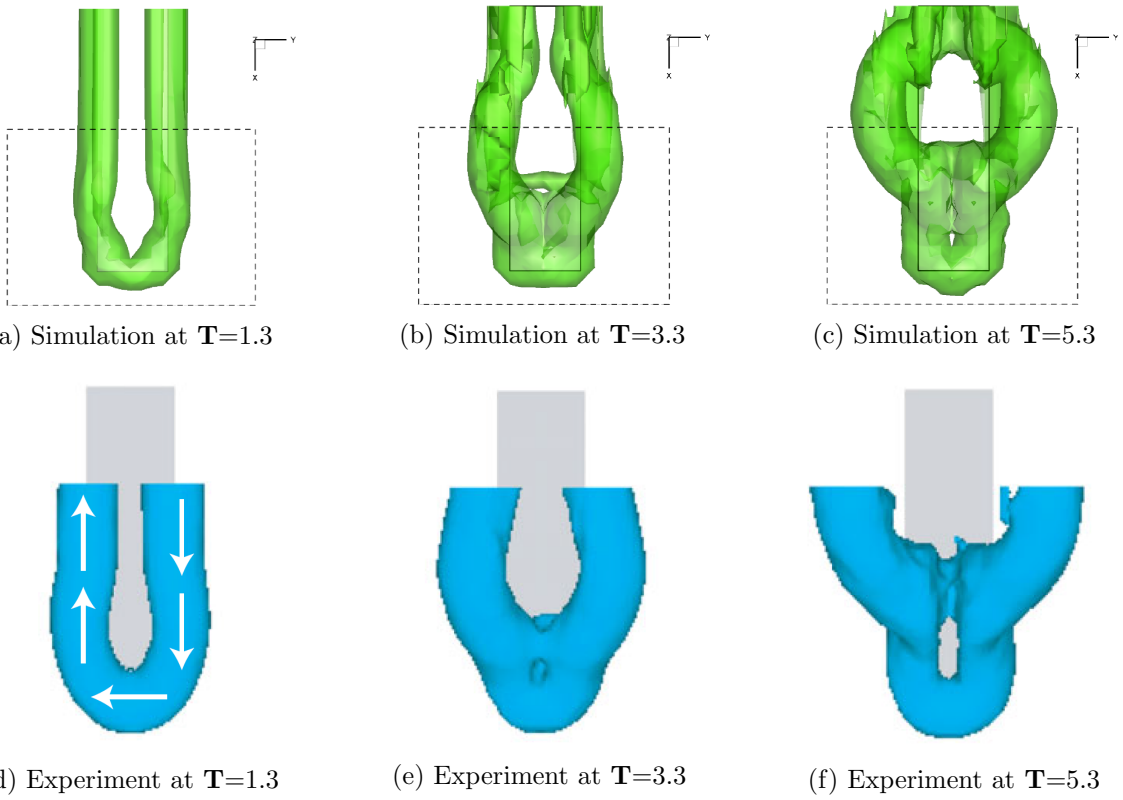

(a) Simulation at **T**=1.3 (b) Simulation at **T**=3.3 (c) Simulation at **T**=5.3

(d) Experiment at **T**=1.3 (e) Experiment at **T**=3.3 (f) Experiment at **T**=5.3

Figure 4.11: Front view of vorticity magnitude isosurfaces with $|\omega| = 3$ from simulation and experiment. Experimental results taken from Kim and Gharib (2011)

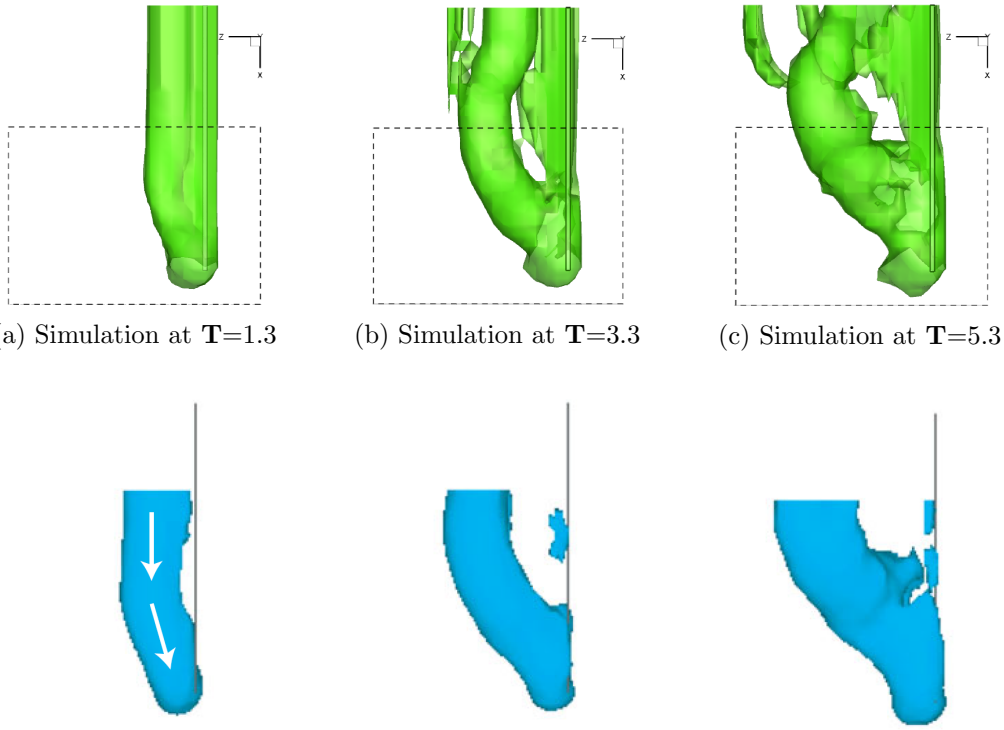

(a) Simulation at **T**=1.3 (b) Simulation at **T**=3.3 (c) Simulation at **T**=5.3

(d) Experiment at **T**=1.3 (e) Experiment at **T**=3.3 (f) Experiment at **T**=5.3

Figure 4.12: Side view of vorticity magnitude isosurfaces with $|\omega| = 3$ from simulation and experiment. Experimental results taken from Kim and Gharib (2011)

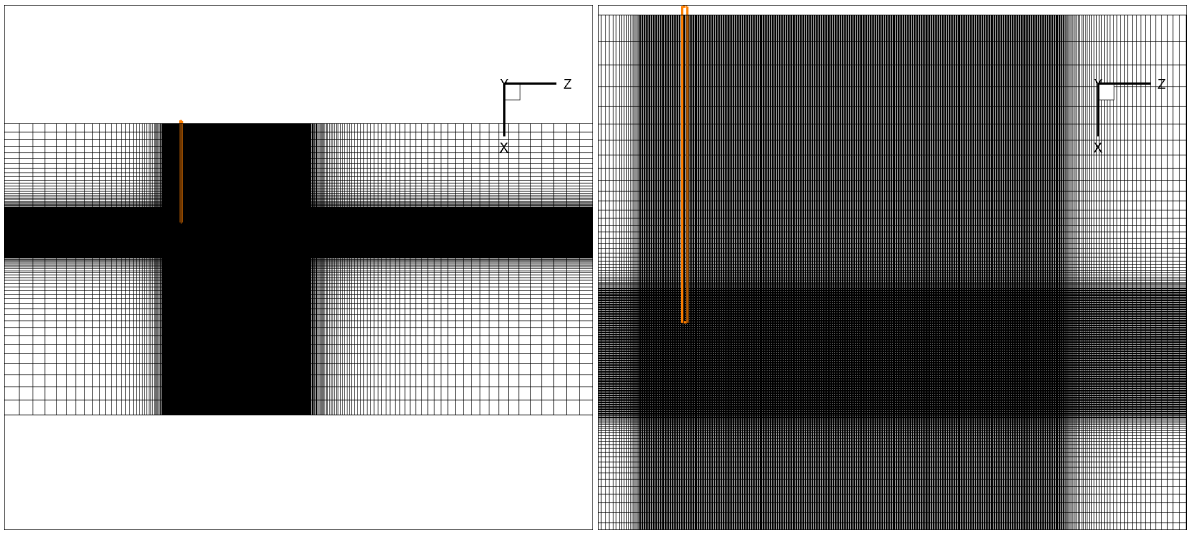

(a) (b)

Figure 4.13: The non-uniform grid used in the simulations with a moving body along with a close up.

4.2.2 Impulsively started flat plate with zero inflow

In the next simulation the inflow will be set to zero and the plate will be accelerated to a constant final velocity. The acceleration of the plate is the same as the acceleration of the inflow in the previous experiment, and all other parameters are left the same to be able to compare the two cases. As with the grid in Section 4.1, the grid has to be extended to prevent the tip of the plate from moving out of the uniform region. The resulting grid is shown in Figure 4.13a, in which the uniform section is 2.5 times larger than for the steady plate case. This larger grid will make the calculations more demanding.

The drag force of the case with $\Delta x = 0.006$ and $\Delta t = 0.0005$ is shown in Figure 4.14. The results clearly reveal the oscillations due to the moving boundary as mentioned in Section 4.1. The averaged force is also shown, along with the result of the steady plate with inflow. Since the frequency of the fluctuations can be calculated from the plate velocity and the cell size, averaging is done over the number time steps that make up one fluctuation cycle.

From Figure 4.14 it can be seen that the moving plate has a slightly lower peak than the steady case. The second hump is lower and shorter than the one in the steady case as well. The differences are most likely caused by the slightly different velocity 'felt' by the body. After the second hump the force coefficient goes to a steady state value of $C_D = 1.83$ which is about 5% lower than for the steady plate and almost 11% lower than that found in the experiment. The vorticity magnitude isosurfaces are examined as well, and show no significant differences with the ones from the steady plate case.

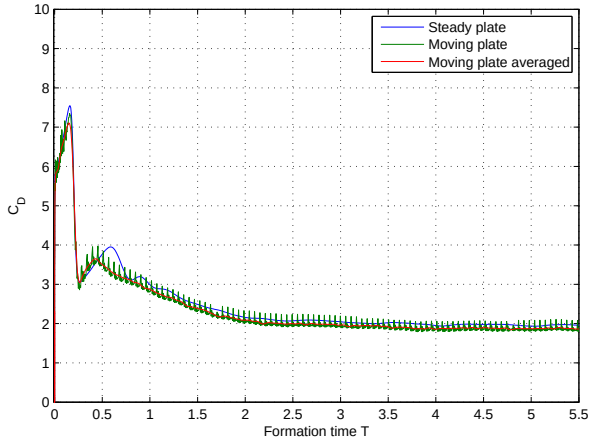

Figure 4.14: C_D response of the moving plate along with its averaged value, compared to the response of the steady plate with inflow.

4.3 Grid and time step study

The uniform section of the grid will be refined to investigate the effect of the cell size on the solution. A coarser grid with $\Delta x = 0.012$ and a finer grid with $\Delta x = 0.006$ will be used, as well as a smaller time step of $\Delta t = 0.00025$, to simulate the cases of Section 4.2.

4.3.1 Steady plate

The drag force of the three different grids used to simulate the steady plate case are shown in Figure 4.15. The initial peak is 1.5% higher for the $\Delta x = 0.006$ case and the same for the case with $\Delta x = 0.012$. The difference between the steady state values is less than 1% for all cases. The big difference between the three cases occurs at the second hump. For the cases with $\Delta x = 0.009$ and 0.012 the second hump starts at the same time, but for $\Delta x = 0.012$ the hump is lower and takes longer. The case with $\Delta x = 0.006$ behaves rather differently, with a much smaller hump that starts earlier. Clearly this part of the solution shows no grid convergence.

Next to the grid refinement, the effect of changing the time step is also investigated. Figure 4.16 shows the drag force of two simulations at $\Delta x = 0.009$, one with $\Delta t = 0.0005$ and one with $\Delta t = 0.00025$. It can be seen that the peak is shifted slightly to the right with the smaller time step but that the amplitude does not change.

4.3.2 Moving plate

To investigate the effect of the cell size and time step on the moving case a second simulation is done with $\Delta x = 0.012$ and $\Delta t = 0.001$. Averaging out the fluctuations again gives the result shown in Figure 4.17a. The second hump appears to start differently for the new case, however investigating the non-averaged values in Figure 4.17b shows that this difference is

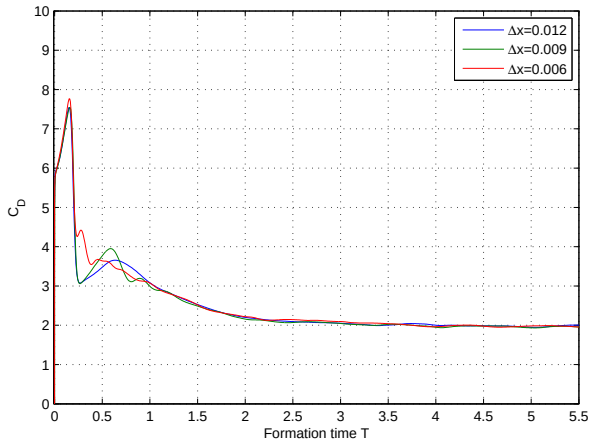

Figure 4.15: C_D vs formation time for the steady plate for Δx=0.012, 0.009 and 0.006.

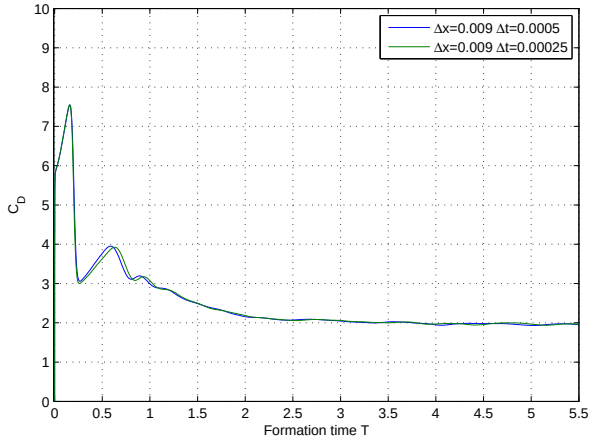

Figure 4.16: The drag force vs formation time for the steady plate for Δx=0.009 at Δt=0.0005 and 0.00025.

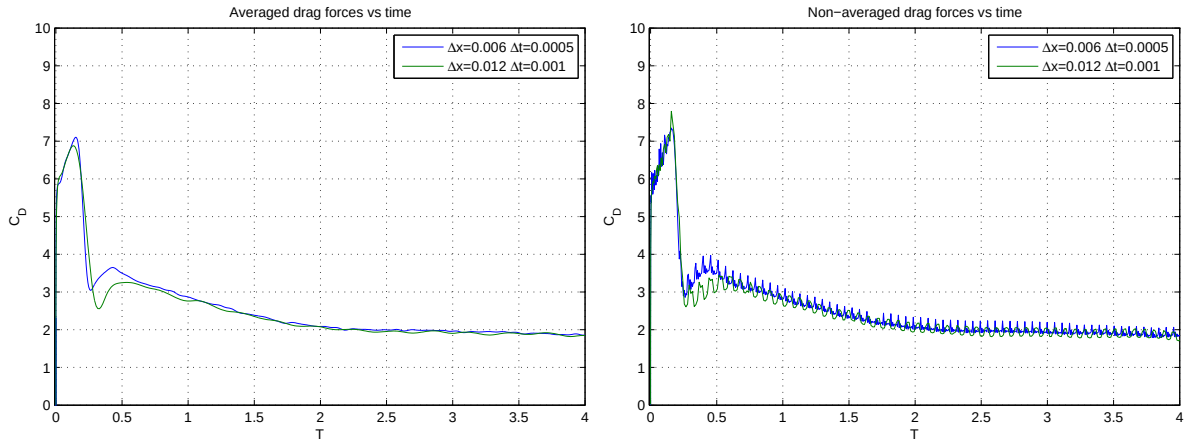

(a) (b)

Figure 4.17: Averaged and non-averaged C_D vs formation time plot of the moving plate.

primarily caused by averaging of the fluctuations. Still, the hump is lower than the one for the $\Delta x = 0.009$, $\Delta t = 0.0005$ case, meaning this part of the solution again shows no grid convergence. The initial peak is roughly 3% higher for the case with $\Delta x = 0.006$ and $\Delta t = 0.0005$. Both simulations converge to the same steady state value.

4.3.3 Influence of plate thickness

In Section 4.2 it was suggested that the effect of the thickness of the plate on the value of the drag force is small. To test this assumption a simulation is performed with the plate thickness equal to the experiment. This has to be done with $\Delta x = 0.006$ to ensure there are enough grid points inside of the body with this small thickness. The result is shown in Figure 4.18. The peak is 4.5% higher in the case of the thin plate, and there are no extra bumps after the initial peak. Both cases converge to the same steady state solution. Although both of these results show differences with the experimental solution, the small difference between them can be seen as proof of the assumption that the plate thickness does not have a large effect on the force.

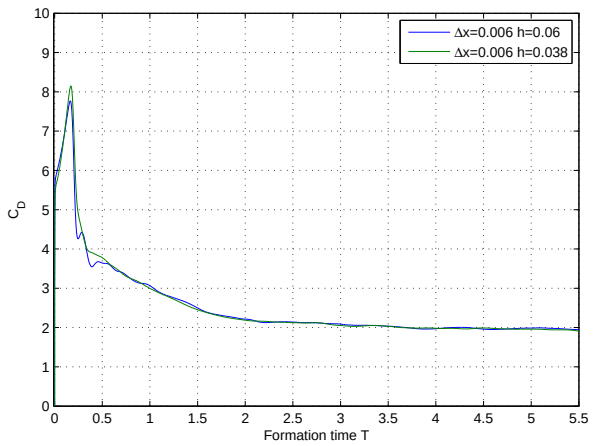

Figure 4.18: The drag force vs formation time for the steady plate for Δx=0.006 at h =0.06 and h =0.038

Chapter 5

Set-up of simulations

To investigate how deformation of the chord affects the aerodynamic mechanisms around a flapping wing a simplified model has been created for the flow simulations. This chapter will describe the model and its simplifications. Next it will describe the simulations that will be performed with the model and finally the grid on which the simulations are performed will be shown.

5.1 Wing model

A wing will be modeled as a rectangular flat plate with a chord of $c = 0.1$[m], a thickness of 0.006[m] and an aspect ratio $AR = 2$. This aspect ratio is chosen at the low side of the range of that of flying insects which is between 2 and 10 (Dudley, 2002). The low value is chosen to reduce computational costs. Instead of modeling two separate plates, a symmetry plane is used which will reduce the required computational resources as well. A three-dimensional view of the motion is shown in Figure 5.1, and a topview is shown in Figure 5.2. In this figure **D** represents the distance to the symmetry plane, and θ the flapping angle. Insects have a wide range of flapping angles (Dudley, 2002) and in this case a total flapping angle θ of 45° is chosen. This flapping angle would be small for two-winged insects but is more typical to that of a four-winged MAV in biplane configuration, like the Delflys shown in Figure 1.1 (e.g. Delfly II has maximum flapping angle $\theta = 48°$ (Kristien M.E de Clercq et al., 2009)). The configuration would then correspond to one wing pair, with the assumption that the wing pairs do not influence one another. The motion will start with an outstroke, which results in θ given by Equation 5.1.

$$\theta = 22.5 - 22.5\cos(ft) \tag{5.1}$$

In Equation 5.1 f is the flapping frequency and t is the solution time. The Reynolds number based on the average tip velocity U should be around that of the validation cases in Section 4.2. Taking $f = 1[s^{-1}]$ gives a average tip velocity of $U = 2cAR\theta = 0.314[m/s]$, with θ given

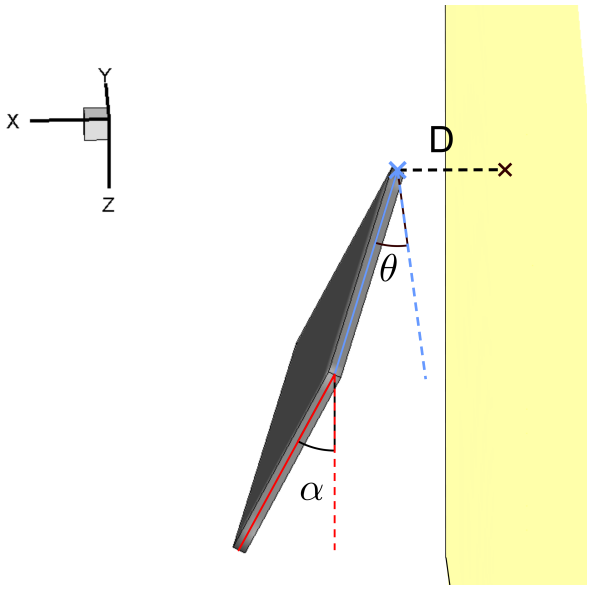

Figure 5.1: Three-dimensional view of the flapping motion.

	Value	Non-dimensionalized value
Chord	0.1[m]	1
Thickness	0.006[m]	0.06
Aspect ratio	2	2
Average tip velocity	0.314 [m/s]	1
Frequency	1 $[s^{-1}]$	0.319
Reynolds number	2002	2002

Table 5.1: Parameters of the simulations

in radians. Using the definition $\mathcal{R}e = \frac{UL}{\nu}$ and taking $L = c$ and ν as the kinematic viscosity of air at sea level (15.68×10^{-6}) gives $\mathcal{R}e = 2002$. The reduced frequency is now given by $k = fc/U = 0.319$. All variables are summarized in Table 5.1. This table also includes the non-dimensionalized variables, which are calculated using the chord length and the average tip velocity.

5.2 Chordwise deformation patterns

To test the effect of the deformation two different type of deforming chords are defined, as well as a case without deforming chord. How these deforming shapes were tested is explained in Section 5.3.

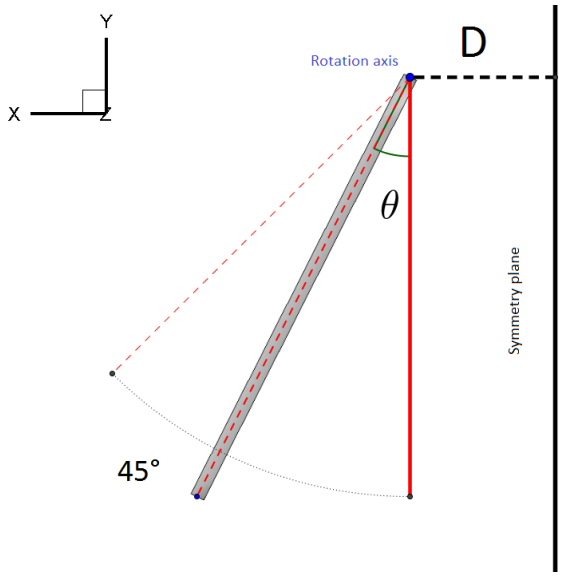

Figure 5.2: Top view of the flapping motion.

5.2.1 Rigid case with rotation

A fully rigid plate given just the flapping motion described n the previous section would give only drag, since it has 90 degree angle of attack. To create an angle of attack the plate will be rotated around the leading edge as shown in Figure 5.3. This angle is given by Equation 5.2.

$$\alpha = -\alpha_{max} \sin(kT) \tag{5.2}$$

In which α_{max} represents the maximum angle. Note that this angle α is not the angle of attack, but instead 90 degree minus the angle of attack.

5.2.2 Deforming end

The first deforming case does not contain any pitching, meaning an angle of attack is created by the deformation alone. This is done by assuming the leading edge remains straight and the maximum deformation occurs at the trailing edge. The shape of the chord is described using a quadratic function of the distance from the leading edge. The deformation is given by Equation 5.3.

$$\delta_{end} = -D_{end}^{max} \left(\frac{z}{c}\right)^2 \sin(kT) \tag{5.3}$$

In Equation 5.3 D_{end}^{max} is the maximum deformation and $\frac{z}{c}$ is the distance from the leading edge normalized by the length of the chord. The resulting shape is shown in Figure 5.4. It can be seen that this shape increases the angle of attack near the leading edge compared to the rigid case.

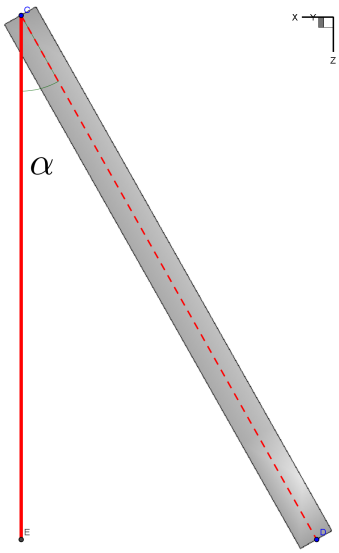

Figure 5.3: Definition of chord for the rigid case.

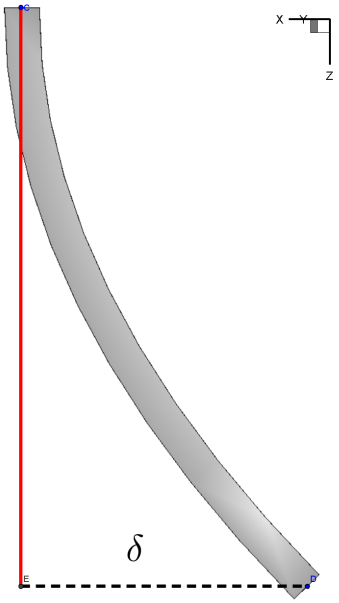

Figure 5.4: Shape of the chord for the deforming end case.

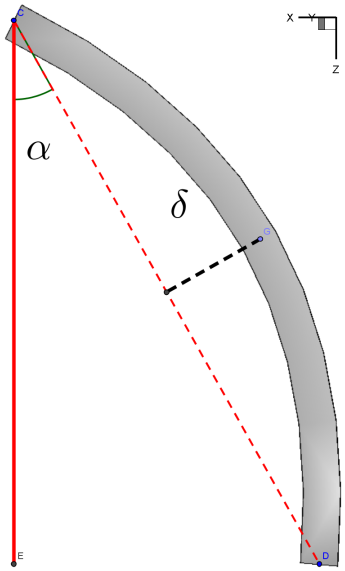

Figure 5.5: Shape of the chord for the deforming center case.

5.2.3 Deforming center

The second deforming case allows the leading edge to rotate. It again uses a quadratic function to describe the deformation, this case having the maximum deformation at the center of the chord. The deformation is given by Equation 5.4.

$$\delta_{center} = -D^{max}_{center}\left[1 - 4\left(\frac{z}{c} - 0.5\right)^2\right]\sin(kT) \tag{5.4}$$

The deformation given by Equation 5.4 is combined with the angle of attack given by Equation 5.2 to give the complete deformed shape in time. The resulting shape is shown in Figure 5.5. From the figure it is clear that for this case the deformation decreases the angle of attack at the leading edge compared to the rigid case.

5.2.4 Elongation of arc length

The previously defined chord shapes have not taken into account that the deformation will result in the distance between the leading and trailing edge becoming smaller. This simplification means that the plates will stretch out during the deformation, increasing the surface area of the plates. This increase in arc length is significant at the maximum deformation for both cases, meaning its effect on the forces cannot be ignored. Although calculation of the force coefficients will take the increasing surface area into account, any quantitative comparison of the forces created by the different shapes could still be misleading. Care has to be taken that effect of extending the chord is not confused with aerodynamic mechanisms. The maximal elongation of the plates depends on the set values of D^{max} and will be calculated in the following section.

5.3 Performed simulations

Several simulation will be performed using the defined motion and chord deformation. They consist of three spanwise constant deforming cases, three spanwise varying deforming cases, and finally two cases with changing distances to the symmetry plane.

5.3.1 Spanwise constant deformation

All three cases discussed in Section 5.2 will first be simulated, with α and δ constant for the entire span of the plate. For the rigid case α_{max} is set to 30°. Care must be taken that the bottom of the plate does not cross the symmetry plane when it is at the maximum angle, so the distance **D** can be calculated. The maximum angle α occurs when $\theta = 0$. This means the plate has an angle of 22.5° with respect to the symmetry plane, and thus **D** can be calculated using $\mathbf{D}/c > \sin 30 \cos 22.5 = 0.46$. For this reason the distance to the symmetry plane is set to **D**=0.50c. The deformation δ_{end} is taken such that the trailing edge position matches that of the rigid case. This means that $D_{end}^{max} = \sin 30 = 0.5c$. As mentioned in Subsection 5.2.4 the deformation causes the chord to be elongated. The length of a curve y is given by Equation 5.5.

$$L_{ext} = \int \sqrt{1 + \left(\frac{\partial y}{\partial x}\right)^2} dx \tag{5.5}$$

Entering Equation 5.3 into Equation 5.5 gives a maximal elongated length of $L_{ext} = 1.148c$, or an increase in length of 14.8%. This increase is used to calculate the force coefficients given by Equation 5.6.

$$C_i = F_i \frac{2c^2}{S_{ext}} \tag{5.6}$$

In which S_{ext} is the extended surface area given by $L_{ext} c AR$.

Initially the deforming center case was set up with $D_{center}^{max} = 0.35c$, which would cause the extended chord length to match that of the deforming end case, enabling direct comparison between the two cases. However this D_{center}^{max} corresponded to a very extreme deformation which would yield no useful insights. Instead, the value was taken as $D_{center}^{max} = 0.175c$. Entering Equation 5.4 into Equation 5.5 gives a maximal elongation of 7.7%. On top of the deformation this case will also be rotated with angle α, equal to the rigid case. All parameters are non-dimensionalized using chord length c, and summarized in Table 5.2. Figure 5.6 shows part of the instroke for the three cases for extra clarity.

5.3.2 Spanwise varying deformation

In insect wings the deformation is usually higher near the wing tip due to torsional flexibility of the wing (Mazaheri and Ebrahimi, 2010). To investigate the effect of the spanwise varying deformation the parameters of the spanwise constant simulations are redefined as functions

Parameter	Value
Distance to symmetry plane	0.5
Angle α	30°
D_{end}^{max}	0.5
D_{center}^{max}	0.175

Table 5.2: Non-dimensionalized parameters for the spanwise constant deforming cases.

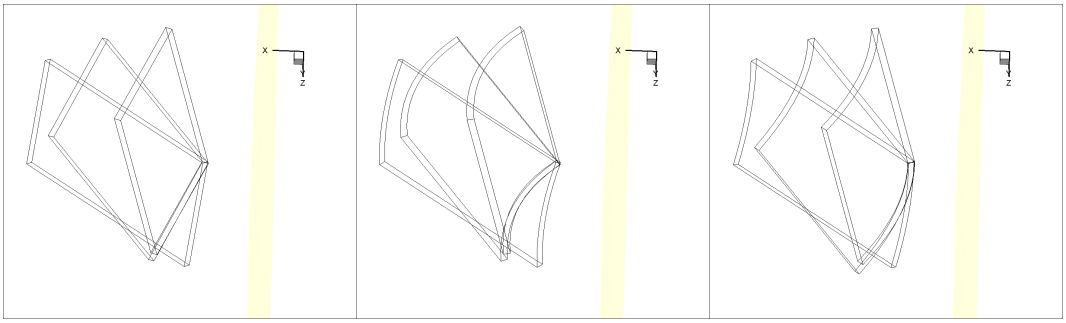

(a) (b) (c)

Figure 5.6: Three dimensional overview of the instrokes of the spanwise constant deforming cases.

of the span position. This is done by a linear function resulting in a undeformed unrotated chord at the root of the plate, and the shape at the tip matching that of the spanwise constant deforming case. Since the span is equal to $2c$, taking y in spanwise direction results in the new definitions in Equations 5.7 to 5.9.

$$\alpha = -\frac{y}{2c}\alpha_{max}\sin(kT) \tag{5.7}$$

$$\delta_{end} = -\frac{y}{2c}D_{end}^{max}\left(\frac{z}{c}\right)^2\sin(kT) \tag{5.8}$$

$$\delta_{center} = -\frac{y}{2c}D_{center}^{max}\left[1-4\left(\frac{z}{c}-0.5\right)^2\right]\sin(kT) \tag{5.9}$$

All parameters stay the same as the ones shown in Table 5.2. Three dimensional views of the instroke of the three cases are shown in Figure 5.7.

5.3.3 Distance to symmetry plane

The minimum distance to the symmetry plane was determined to ensure that the trailing edge of the spanwise constant deforming plates would not cross the symmetry plane. With the spanwise varying deformation this is not an issue since there is almost no deformation of

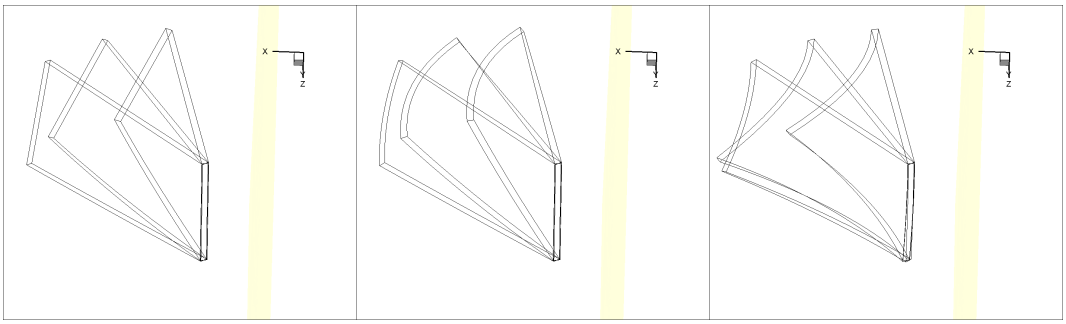

(a) (b) (c)

Figure 5.7: Three dimensional overview of the instrokes of the spanwise varying deforming cases.

the chords near the root. This allows a simulation with the plates closer to the symmetry plane to investigate the effects on the aerodynamics. The rigid case and the deforming center case are both simulated at $\mathbf{D} = 0.25c$, as well as without a symmetry plane, which simulates a single wing.

5.4 Grid size

The grid used for the simulations described in this chapter is similar to the non-uniform grids used for the validation cases in Chapter 4. It again consist of a section with uniform cell size around the body, after which it expands exponentially towards the outside of the domain. In this case the uniform section is much larger however, as can be seen in Figure 5.8. This is needed both because the tip of the plate moves through a larger area, and due to the presence of the symmetry plane. Due to the larger region with uniform cell size the required computational time increases dramatically. Therefore it is chosen to use the coarsest grid from the validation cases in Chapter 4 with uniform cell size $\Delta x = 0.012$. This leads to a region with uniform cell size of 289x413x260 cells. A time step of $\Delta t = 0.0008$ is used for all cases. Several flapping cycles will be simulated, after which it will be determined from the force coefficients if the behavior is periodic. This is done to exclude startup effects. When the forces behave periodic a final cycle is simulated from which the flow variables are stored at 25 points during the cycle. These results from the final cycle will be used for the visualizations in Chapter 6.

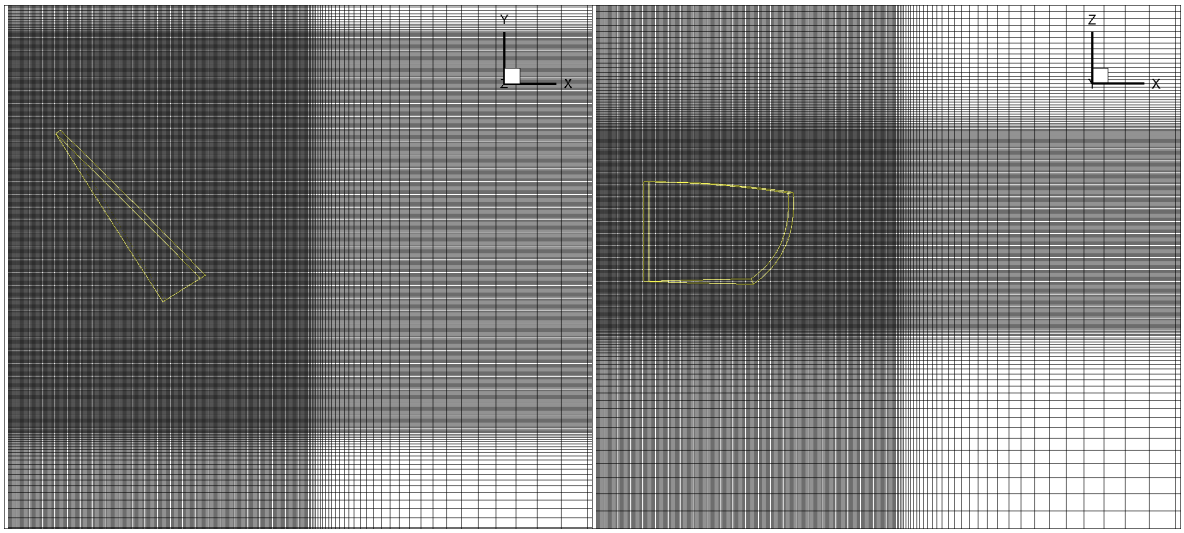

(a) (b)

Figure 5.8: The non-uniform grid used for the deforming chord simulations.

Chapter 6

Results

The results of the different simulations presented in Chapter 5 are presented and discussed in the following chapter. First the cases with spanwise constant deformation are investigated. Next the results of the spanwise varying deformation cases are shown and compared to the spanwise constant deformation simulations. The influence of the symmetry plane is investigated by looking at a case with the plate closer to the symmetry plane, as well as a single plate without symmetry plane. This is done for the spanwise varying rigid case, and the spanwise varying deforming center case. Finally the vortices around the plate are examined to determine their effect on the forces on the plate.

6.1 Spanwise constant deformation

For the three cases with spanwise constant deformation the lift and drag coefficients are calculated, and averaged over the last 3 cycles. Figure 6.1 shows the lift coefficient C_L and drag coefficient C_D for these cases, as well as their cycle average value. Figure 6.2 does the same for C_L/C_D, in which the average value is calculated as the cycle average value of C_L/C_D (not the the cycle average value of C_L divided by the cycle average value of C_D). The force result of the complete simulations are shown in Appendix B.1, Figure B.1. Although averaging the plots over 3 cycles reduces the fluctuations due to the moving boundary, they are still present to some extend. Averaging over more cycles would give smoother results but was considered too time consuming, as this would require a longer simulation time. Figures 6.1 and 6.2 represent one entire cycle, starting with an outstroke. The cycle average values of the three cases are shown in Table 6.1.

From the average lift coefficients in Figure 6.1a it can be clearly seen that the deforming center case creates the highest lift, followed by the rigid case and that the deforming end case creates the lowest lift. The lift generation throughout the motion is very similar for all three cases, with the most noticeable differences being the maximal values of C_L and the lift build up at the start of the instroke.

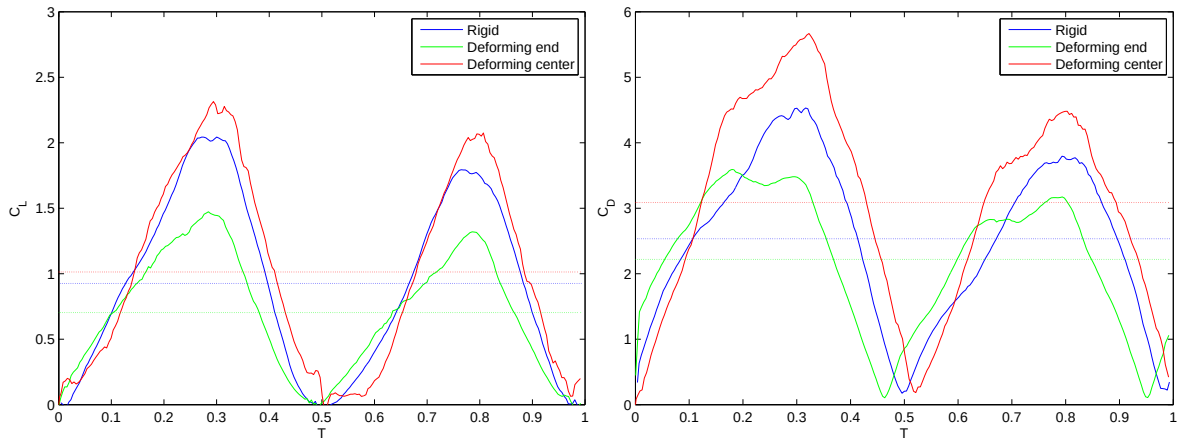

(a) (b)

Figure 6.1: C_L and C_D plot for the spanwise constant deforming cases. The motion starts with an outstroke.

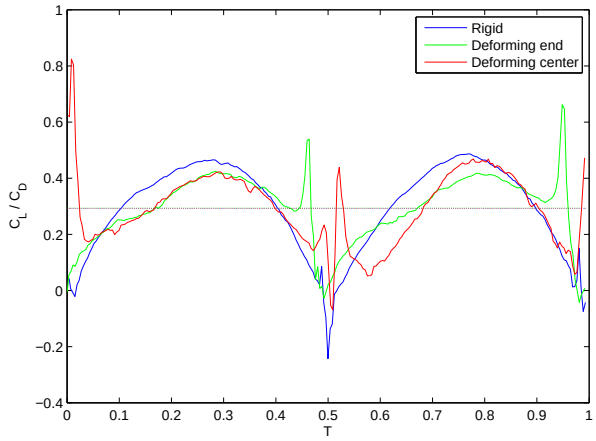

Figure 6.2: C_L/C_D plot for the spanwise constant deforming cases. The motion starts with an outstroke.

Case	Average C_L	Average C_D	Average C_L/C_D
Rigid spanwise constant	0.9266	2.5326	0.2930
Deforming center spanwise constant	1.0130	3.0850	0.2931
Deforming end spanwise constant	0.7015	2.2200	0.2939

Table 6.1: Cycle averaged values of the force coefficients for the spanwise constant cases.

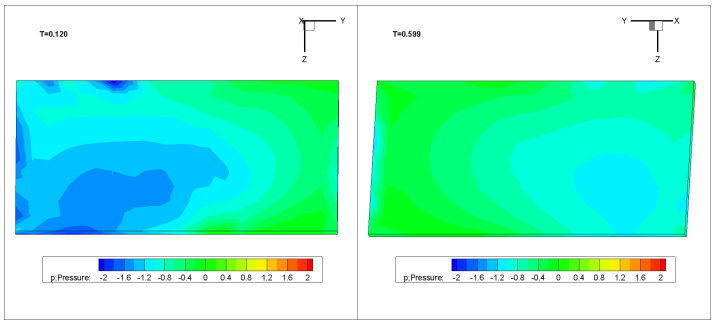

(a) (b)

Figure 6.3: Pressure contours of the lower surface for the spanwise constant rigid case at a) T=0.12 with the wingtip located at the left side and b) T=0.60 with the wingtip located at the right side.

The C_L buildup at the beginning of the instroke differs significantly from that at the beginning of the outstroke. At the beginning of the outstroke, near T=0, C_L increases almost immediately for the deforming end case, and with a small delay also for the rigid case. The lift coefficient of the deforming center case also increases right from the beginning, and a small hump can be noticed in the buildup. Investigation of the non-averaged forces showed that this hump is caused by fluctuations due to the interpolation near the boundary as described in Section 4.1, and is not physical. At the start of the instroke at T=0.5 the rigid case C_L starts increasing almost immediately again, followed by the deforming end case. The gradients are slightly lower however, causing a lower peak in C_L. The gradient of the deforming center case from T=0.6 to 0.7 is actually equal to that from T=0.1 to 0.2, however, it is almost zero for the first 0.1 period of the instroke, from T=0.5 to 0.6. The difference between the outstroke and the instroke is caused by the presence of the symmetry plane. The effect of the symmetry plane can be seen very clearly from the pressure contours on the upper surface of the plates, which are shown in Figures 6.3, 6.4 and 6.5. These figures clearly show that the symmetry plane causes a large low pressure region at the upper surface of the plates, creating higher lift. The difference is particularly important for the deforming center case, due to the shape of the plate at the location of the low pressure region. At the start of the instroke it can be seen from Figure 6.4b that the low pressure region is located at the lower half of the plate chord. At this location the orientation of the plate is almost vertical with respect to the direction of the motion, meaning the force caused by the low pressure has a very small component in lift direction.

A possible explanation for the lower peak in C_L for the deforming end case, is that the higher angle of attack causes shedding of the leading edge vortex (LEV), as suggested in previous studies (Miller and Peskin, 2009; Gillebaart, 2011). To investigate if this is indeed the case the Q criterion contour is plotted for the cases at T=0.12, 0.28, 0.48 and 0.52 at 50% span in Figure 6.6 to see if the LEV indeed sheds during the outstroke. From the plots at T=0.12 (Figures 6.6a to 6.6c) and T=0.28 (Figures 6.6d to 6.6f) it can be seen that for the deforming center case the LEV develops slower than for the other two cases, which is caused by the lower angle of attack at the leading edge. This slower LEV development can also be seen in the contour plot of Figure 6.4b, and causes the slower lift buildup observed in Figure 6.1.

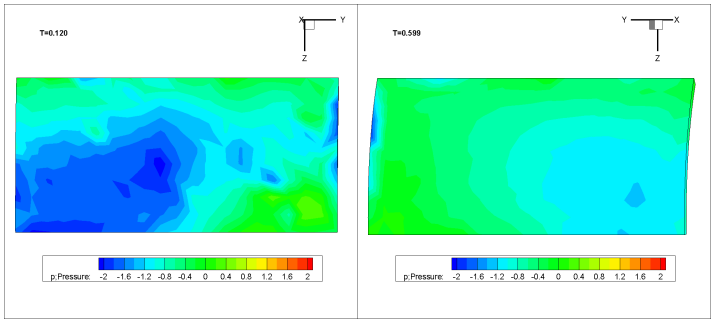

(a) (b)

Figure 6.4: Pressure contours of the lower surface for the spanwise constant deforming center case at a) T=0.12 with the wingtip located at the left side and b) T=0.60 with the wingtip located at the right side.

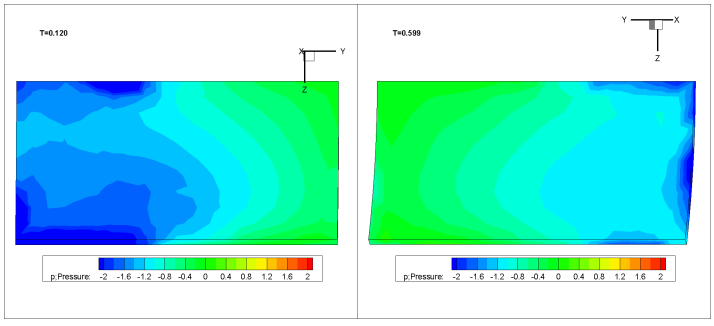

(a) (b)

Figure 6.5: Pressure contours of the lower surface for the spanwise constant deforming end case at a) T=0.12 with the wingtip located at the left side and b) T=0.60 with the wingtip located at the right side.

The higher angle of attack of the other cases does not appear to cause shedding of the leading edge vortex however, as can be seen in the plots at T=0.48 and 0.52 (Figures 6.6j to 6.6l). Shedding of the leading edge vortex is not observed at other points along the span either, leading to the conclusion that the shedding of the leading edge vortex is not responsible for the difference in C_L in these cases. The Q criterion contour plots at other positions along the span can be seen in Appendix B.1, Figures B.2 and B.3.

Instead of shedding of the LEV, the difference in C_L can be understood by looking at the pressure contours on the plate at the moment around the maximum C_L. The lower surface of the three cases at T=0.28 is shown in Figure 6.7, and the upper surface is shown in Figure 6.8. From Figure 6.7 it can be seen that the deforming center case has a larger high pressure region on the lower surface of the plate compared to the rigid case. This high pressure region can be explained by the curvature of the chord of the plate, which causes air to get trapped under the plate. The curvature of the chord in the deforming end case instead reduces the amount of air under the plate compared to the rigid plate, thus reducing the high pressure region and causing a lower C_L.

From the drag coefficients shown in Figure 6.1b it can be seen that the deforming center case creates the highest drag, followed by the rigid case, and that the deforming end case creates the lowest drag. The behavior of C_D is very similar to that of C_L since the same pressure differences responsible for the lift generation also generate the drag. The timing of C_D is changed by the deformations. The rigid case shows a minimum in C_D at T=0.5, when the plate is changing direction from to outstroke to the instroke. The deforming end case shows a minimum in C_D earlier, around T=0.47, and the deforming center case shows a minimum C_D slightly later, around T=0.52. This phase shift can be explained by the way the plates deform. In case the center deforms, the vertical surface area moving trough the fluid is lower at the start of a stroke compared to the rigid case. When the end deforms the same happens at the end of stroke when the plate straightens out.

Figure 6.2 shows the C_L/C_D for the three cases, as well as their cycle average values. It can be seen from Table 6.1 that the cycle average values of C_L/C_D are approximately equal for all three cases, again showing that the difference in pressure distribution caused by the deformations has a similar effect on both the drag and the lift. The development of the curves differ for the three cases, with the rigid case showing an almost symmetric distribution, whereas the deforming end case has a peak in C_L/C_D slightly before reversing direction and the deforming center has a peak slightly after reversing direction. These peaks can be explained by the change in phase of the drag. Since this peaks are just caused by the phase shift of the drag they do not affect the cycle average values.

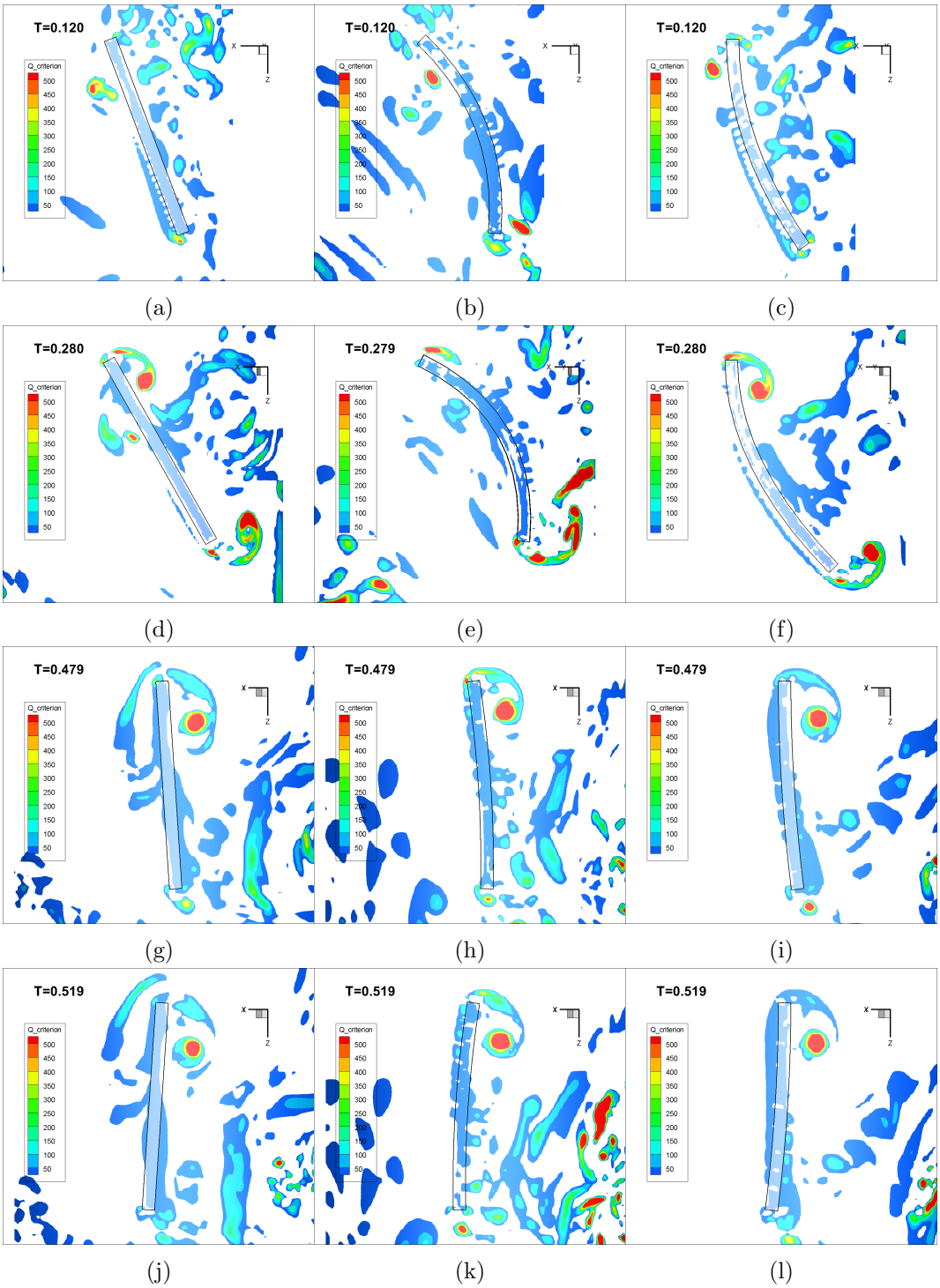

Figure 6.6: Contour plots of the Q criterion at 50% span, for the spanwise constant deformation cases. On the left side the rigid case, in the middle the deforming center case and on the right side the deforming end case.

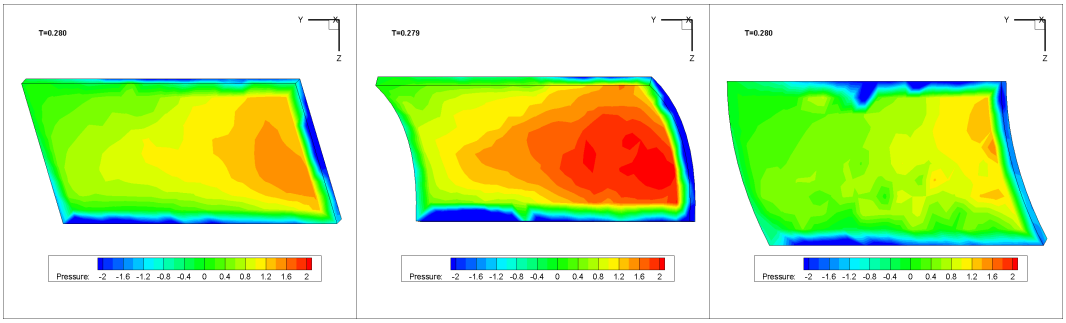

(a) (b) (c)

Figure 6.7: Pressure contours of the lower surface for the spanwise constant deforming cases at T=0.28. a) rigid case, deforming center, c) deforming end.

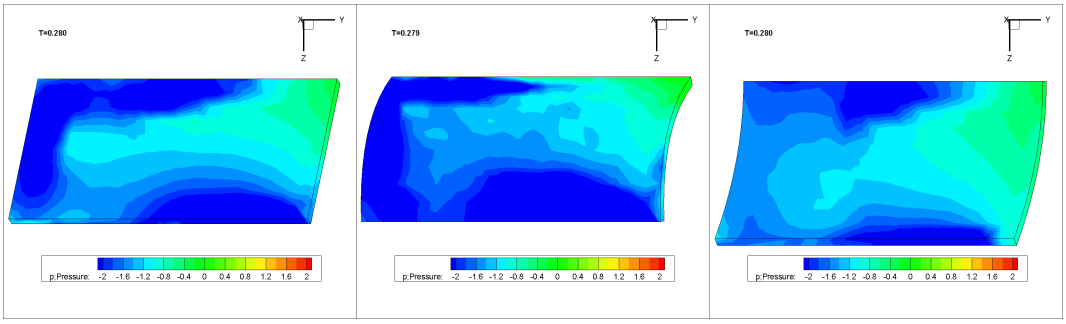

(a) (b) (c)

Figure 6.8: Pressure contours of the upper surfaces for the spanwise constant deforming cases at T=0.28. a) rigid case, deforming center, c) deforming end.

Case	Average C_L	Average C_D	Average C_L/C_D
Rigid spanwise constant	0.9266	2.5326	0.2930
Deforming center spanwise constant	1.0130	3.0850	0.2931
Deforming end spanwise constant	0.7015	2.2200	0.2939
Rigid spanwise varying	0.5558	2.2998	0.2140
Deforming center spanwise varying	0.6171	2.5911	0.2449
Deforming end spanwise varying	0.5948	2.2179	0.2066

Table 6.2: Cycle averaged values of the force coefficients for the spanwise varying cases, as well as the spanwise constant cases copied from Table 6.1.

6.2 Spanwise varying deformation

The cases with spanwise varying deformation are also simulated and the lift and drag coefficient are calculated. The resulting C_L and C_D averaged over the last three cycles are shown in Figure 6.9 along with their cycle average values. The same is shown for C_L/C_D in Figure 6.10. The cycle average values for all three cases are shown in Table 6.2, along with the values from the previous section to allow for an easier comparison. The force coefficients of the full motion are shown in Appendix B.2, Figure B.5

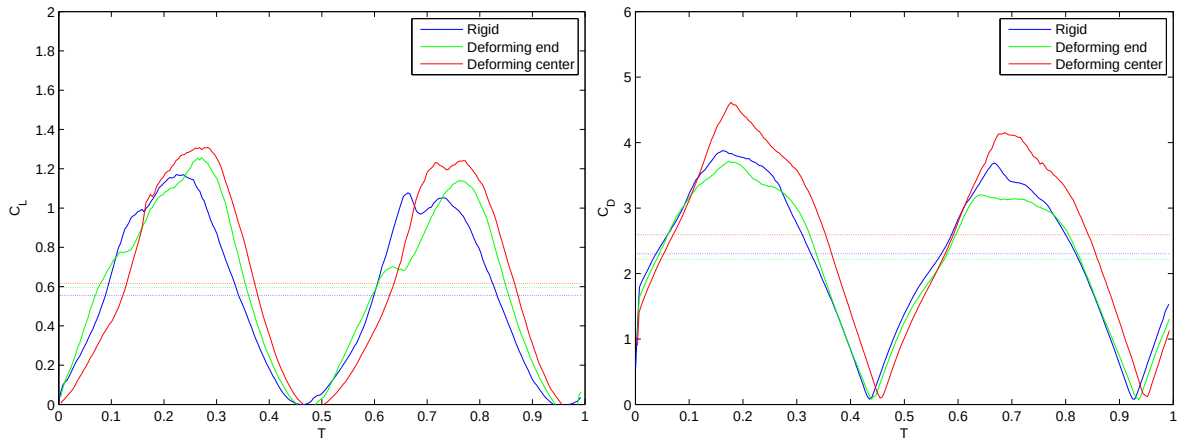

(a) (b)

Figure 6.9: C_L and C_D plot for the spanwise varying deformation cases. The motion starts with an outstroke.

From Table 6.2 it is clear that the lift coefficients of the spanwise varying deformation are considerably lower than those found for the spanwise constant cases. This can be explained by again looking at the pressure contours at the lower surface of the plates, as shown in Figure 6.11. Comparing these contours to the ones shown in Figure 6.7, it can be seen that the high pressure regions are smaller and the pressures are much lower near the root of the plate. This was indeed expected since the plate deforms less near the root. Table 6.2 shows that this effect also lowers the drag coefficients.

From Figure 6.9a it can be seen that both the average and maximum C_L created by the

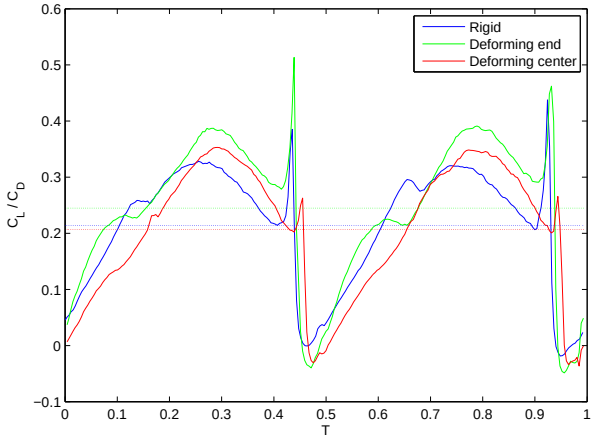

Figure 6.10: C_L/C_D plot for the spanwise varying deformation cases. The motion starts with an outstroke.

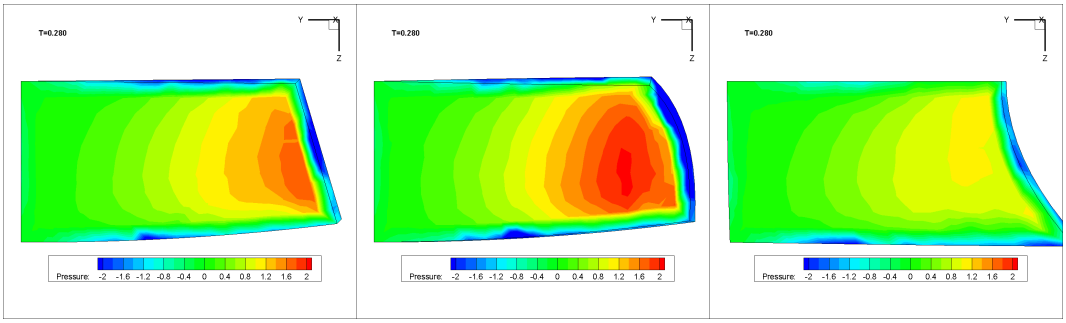

(a) (b) (c)

Figure 6.11: Pressure contours of the lower surfaces for the spanwise varying deforming cases at T=0.28. a) rigid case, b) deforming center, c) deforming end.

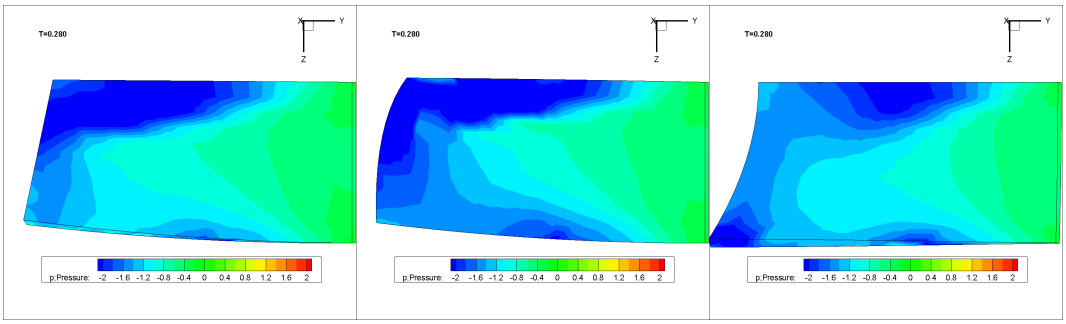

(a) (b) (c)

Figure 6.12: Pressure contours of the upper surfaces for the spanwise varying deforming cases at T=0.28. a) rigid case, b) deforming center, c) deforming end.

deforming center and the deforming end are higher than the lift for the rigid case. This lower lift for the rigid case can not be observed from the pressure on the lower surface shown in Figure 6.11, since the pressure on the rigid case (Figure 6.11a) is higher than on on the deforming end case 6.11c). This means the higher C_L must be caused by a difference on the upper surface. The pressure contours of the upper surfaces for the three cases are shown in Figure 6.12.

Figure 6.12a shows that for the rigid case an extensive low pressure region is located at the leading edge, from about 25% of the span almost to the tip. Figure 6.12b shows a very similar low pressure near the leading edge for the deforming center. Figure 6.12c shows that the deforming end case also has a low pressure region at the leading edge starting around 25% of the span, but it is less strong towards the tip. All cases also show low pressure regions near the trailing edge, which is associated to the trailing edge vortex (TEV), and near the tip, associated to the tip vortex (TV). The deforming end case shows a particular low pressure near the trailing edge tip, which will have a large influence on the C_L due to the orientation of the plate at this position. This can be clearly seen from Figure 6.13, which shows the pressure isosurfaces of p=-1.5 at T=0.28. Since the surface of the plate near the low pressure region has a considerable horizontal surface area, the low pressure region here has a large contribution to the lift. From Figure 6.13 clearly shows the low pressure isosurfaces related to the LEV, TEV and TV. The low pressure at the trailing edge tip is thus caused by a combination of the TEV and TV, meaning these have a significant contribution to C_L. The contribution of the TEV and TV on C_L will be discussed more extensively in Section 6.4. It has to be noted that the elongation of the chord in the deforming end case is significant, and that the low pressure region in this case lies in the region that would be much shorter with the correct chord length. Therefore it is likely that the contribution of this low pressure region to C_L is too large and that C_L is overestimated for this case.

From Figure 6.9a a distinct dip can be seen during the acceleration phase of the plates, both during the outstroke and the instroke. The contour plots of the Q criterion are investigated at the moments around this dip during the instroke, at T=0.559, 0.599, 0.639 and 0.679, at 50% of the span to see if this is associated to shedding of the LEV. The plots are shown in Figure 6.14. Although it can be seen that the LEV moves further away from the plate for the

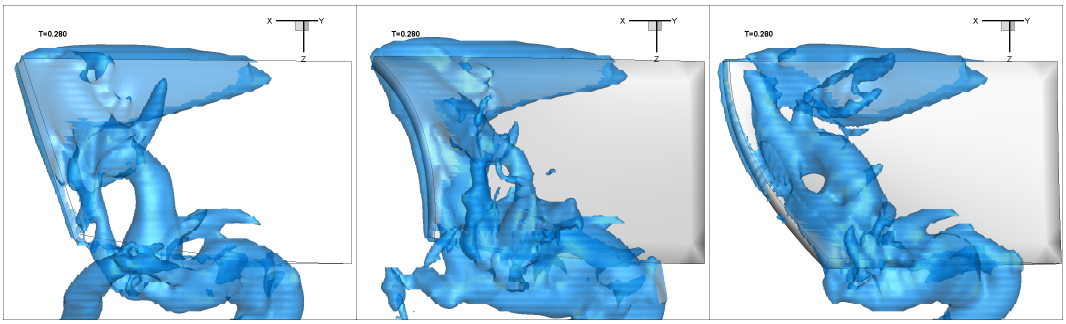

(a) (b) (c)

Figure 6.13: Pressure isosurfaces of $p = -1.5$ near the tip for the spanwise varying deforming cases at T=0.28.

deforming end case, the difference cannot explain the large hump shown in C_L. Contour plots of the Q criterion at different locations along the span do not show distict shedding of the LEV either. These contour plots are shown in Appendix B, Figures B.6 and B.7. Since the shedding of the LEV cannot be identified as the source for the hump, the pressure isosurfaces are investgated. The pressure isosurfaces with $p = -1$ at the beginning of the instroke are shown in Figure 6.15. From Figure 6.15a to 6.15c the vortices from the previous outstroke stroke can be clearly identified, with the shed TV, TEV and LEV in front of the plate. Figures 6.15d to 6.15f show that at T=0.64, the new LEV in the deforming end case interacts with the previously shed LEV, this instant corresponds to the dip in C_L in Figure 6.9a. The other two cases show no interaction, and no change in the C_L slope. At the next instance, shown in Figures 6.15g to 6.15i the shed LEV from the previous stroke has been completly absorbed into the new LEV for the deforming end case, and C_L is again increasing. For the rigid case the interaction between the shed and the new LEV has started, and this is again accompanied by a dip in C_L. Finally Figures 6.15j to 6.15l show the shed LEV completely absorbed by the new vortex for the rigid case as well, and the C_L again increasing. For the deforming center case the interaction between the two vortices is starting, and this matches the small dip in C_L as well. This interaction is not seen in the pressure isosurfaces for the spanwise constant deforming cases, which are shown in Appendix B.1, Figure B.4.

From the previous results it can be concluded that not the shedding of the LEV is responsible for the dip in C_L seen in Figure 6.9a, but the interaction of the LEV with the shed LEV from the previous stroke. If this is indeed the case there should be no dips in the buildup of C_L during the initial stroke, since there will be no previously shed vortices. Figure 6.16 shows the C_L for the three cases during the initial stroke, and it is clear that the dips are indeed absent. To see how the interaction between the two vortices reduces C_L, a close-up of the LEV buildup with and without interaction is shown in Figure 6.17. It can be clearly seen in Figure 6.17b that the LEV from the previous stroke weakens the new LEV.

The faster buildup of the LEV in the deforming end case causes the interaction with the shed vortex to occur earlier. The lowering of the angle of attack by the deforming center case delays the interaction and reduces the negative effect. The curvature of the chord of the plate in the deforming center case also causes the previously shed vortex to get trapped

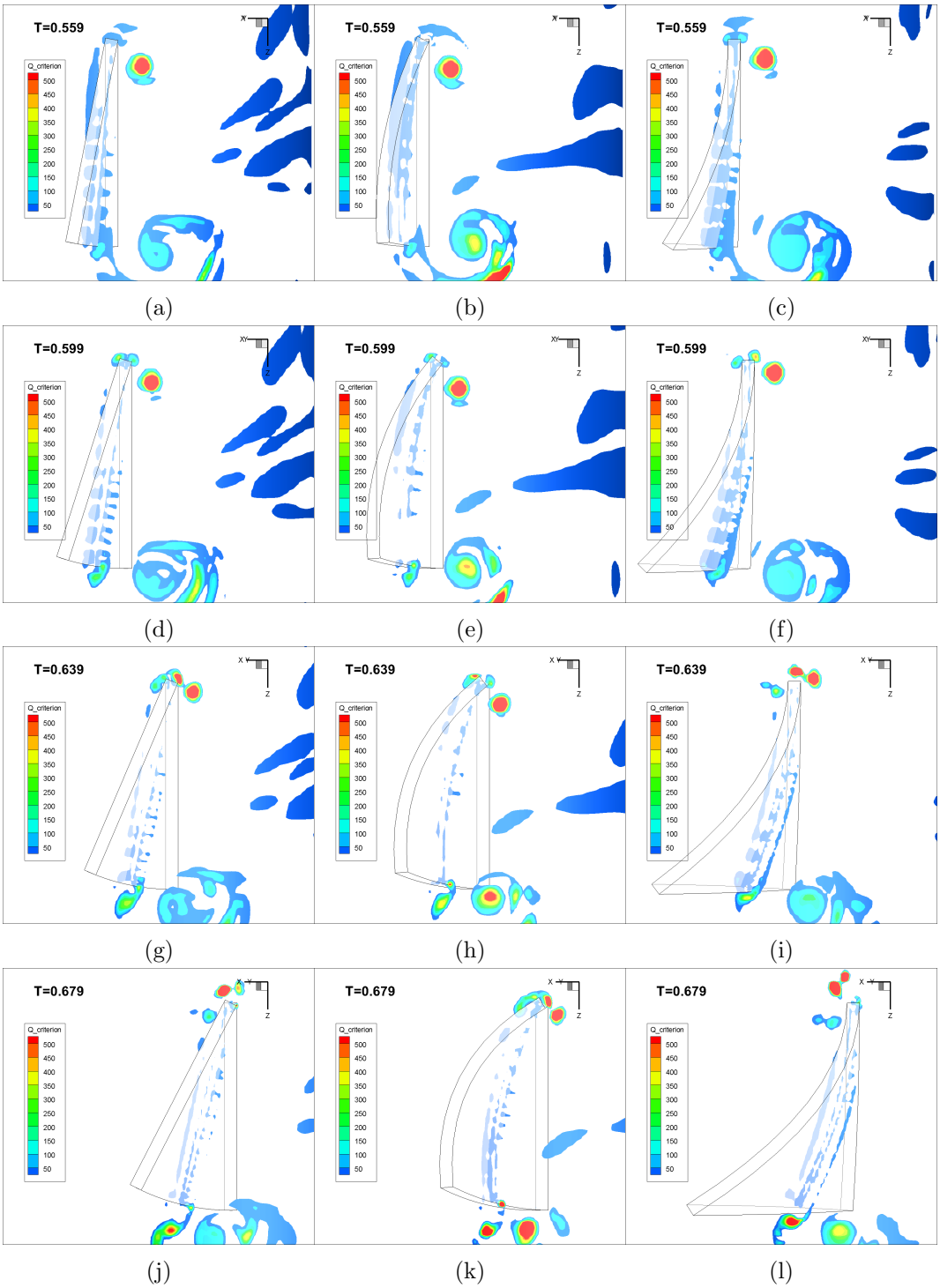

Figure 6.14: Contour plots of the Q criterion at 50% span, for the spanwise varying deformation cases during the instroke. On the left side the rigid case, in the middle the deforming center case and on the right side the deforming end case.

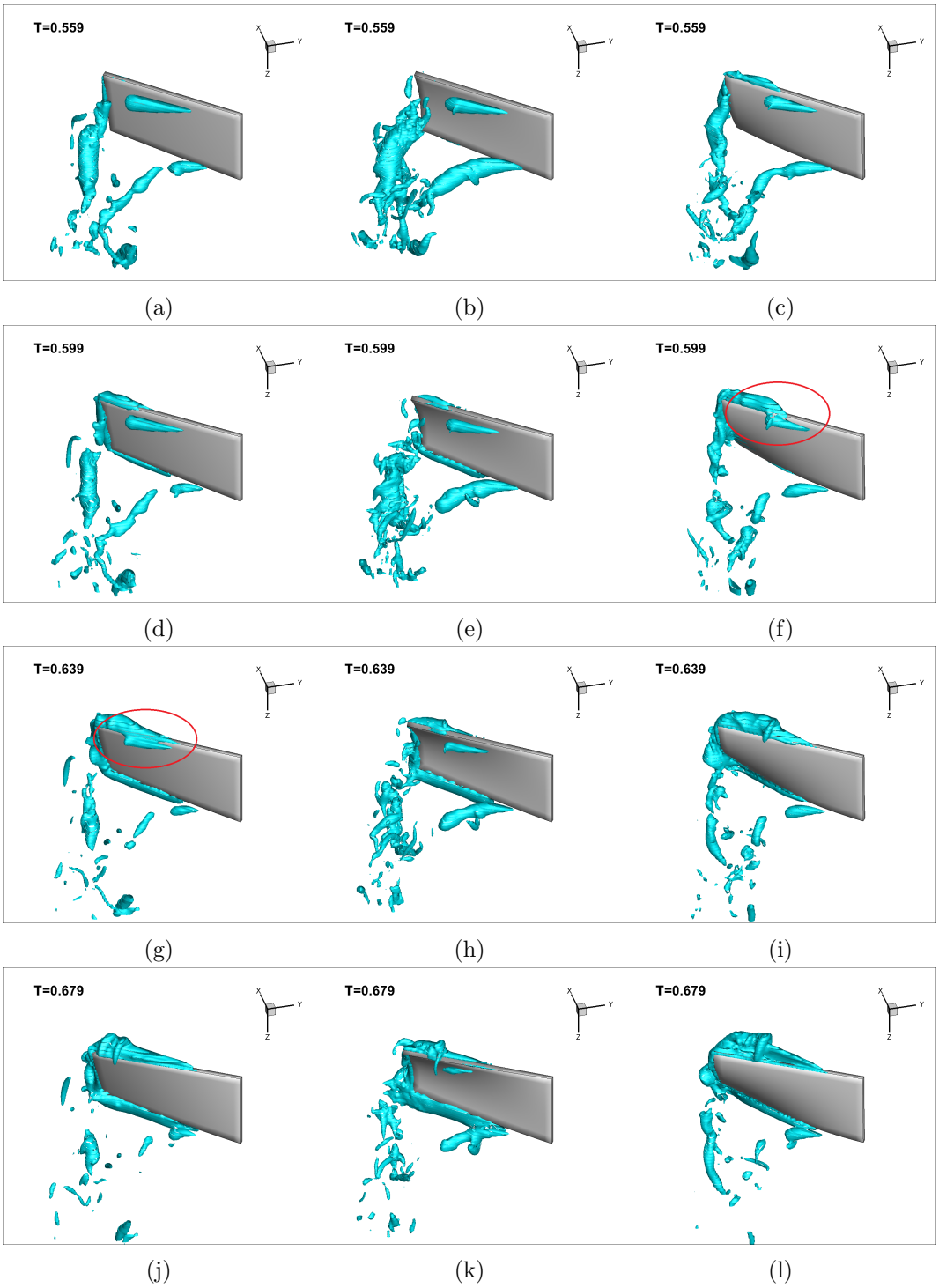

Figure 6.15: Pressure isosurfaces of p=-1 during the instroke. On the left side the rigid case, in the middle the deforming center case and on the right side the deforming end case.

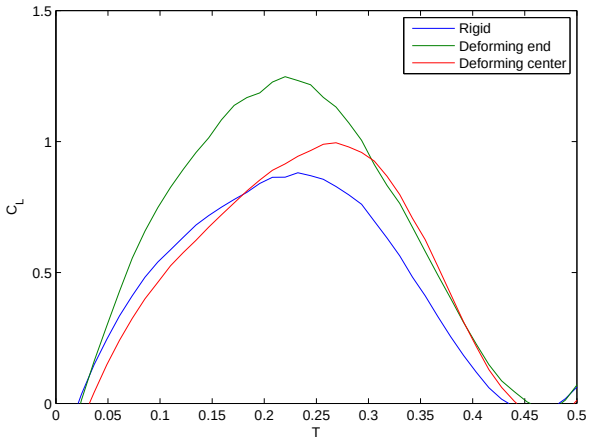

Figure 6.16: C_Ls of the three cases during initial outstroke.

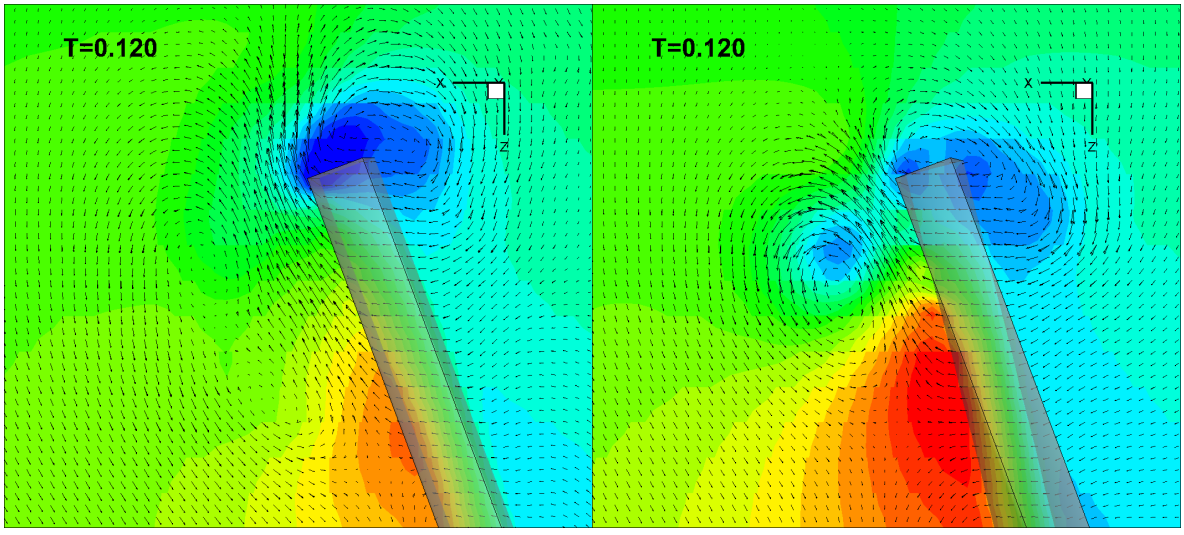

(a) (b)

Figure 6.17: Velocity vectors showing the effect of the interaction of the LEV. Left without interaction, and right with interaction.

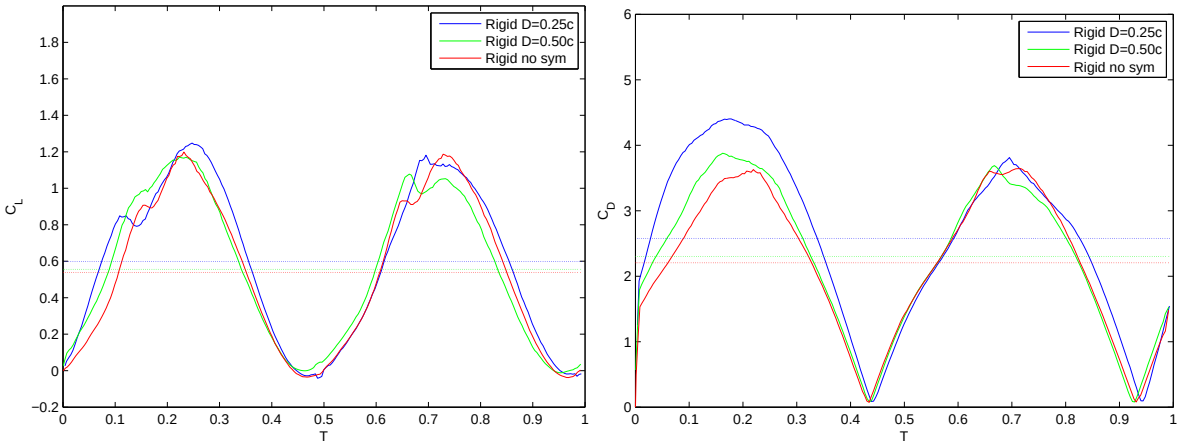

(a) (b)

Figure 6.18: Lift and drag coefficient plot for the spanwise varying rigid cases, at different distances from the symmetry plane. The motion starts with an outstroke.

below the plate, delaying the interaction further. Despite the earlier interaction between the vortices, the deforming end case still shows a higher C_L compared to the rigid case. Although both have similar values around T=0.24, C_L continues to increase for the deforming end case to around T=0.27, whereas the rigid case has reached its peak. The peak of the deforming center case also occurs around T=0.27. This difference in peak timing will be discussed in Section 6.4.

6.3 Effect of distance to symmetry plane

The distance to the symmetry plane as used in the previous experiment was taken as D=0.50c. As explained in Chapter 5 this was done to ensure the plates did not cross the plane in the spanwise constant deformation cases. To investigate the effect of this distance the spanwise varying rigid and deforming center cases are also simulated at a distance of **D**=0.25c and without a symmetry plane.

6.3.1 Rigid case

The lift and drag coefficient for the three rigid cases at different distances are shown in Figure 6.18. The values are again averaged over the three last simulated cycles. The cycle average values are listen in Table 6.3.

From Figure 6.18a it is clear that moving the plate closer to the symmetry plane creates a higher cycle average C_L. During the outstroke this is caused by the faster buildup of the LEV, which is caused by the fling phase of the clap and fling mechanism. Although this mechanism is usually explained with two wings touching one another, or touching the symmetry plane for this case, its effect is still present when there is a small gap. The fling phase occurs during the

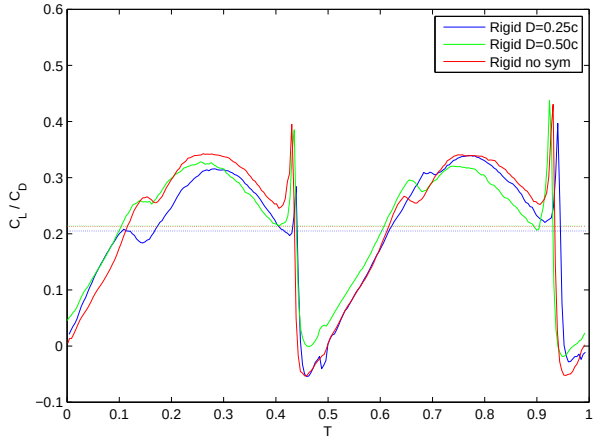

Figure 6.19: C_L/C_D plot for the spanwise varying rigid cases, at different distances from the symmetry plane. The motion starts with an outstroke.

first moments of the outstroke. During the fling the low pressure region between the wings increases the flow over the leading edge, resulting in the creation of massive LEVs (Percin et al., 2011). This is very clear from the C_L buildup. Decreasing the gap between the wings will create a lower pressure and stronger LEVs. This low pressure region will also greatly increase the drag as can be seen in Figure 6.18b.

The positive effect of the faster LEV buildup is reduced by the interaction with the previously shed vortex. The stronger LEV of the D=0.25c case interacts earlier than the weaker vortices of the other two cases, after which its C_L is lower. Around T=0.22 all three cases have the same C_L, however, where the case with D=0.50c and the case without symmetry plane have their peak around T=0.23, the case for D=0.25c continues to increase until its peak at T=0.25. This difference in timing of the peaks will again be discussed separately in Section 6.4.

The clap phase corresponds to the last part of the instroke when the wings clap together. During clap the air between the wings gets trapped and pushed downward, giving a small positive contribution to the lift (Lehmann and Pick, 2007). This effect will be stronger when the distance to the symmetry plane is smaller. The case for D=0.25c shows a slightly higher C_L during the final part of the instroke than the other two cases caused by trapped air being pushed down. This trapped air also gives a small increase in drag.

Figure 6.19 shows C_L/C_D for the different cases. It shows that the average C_L/C_D is almost equal for the single plate and the plate with the symmetry plane at **D**=0.50c. For the case with **D**=0.25c the average is lower so moving the plate closer to the symmetry plane appears to have a negative effect on C_L/C_D.

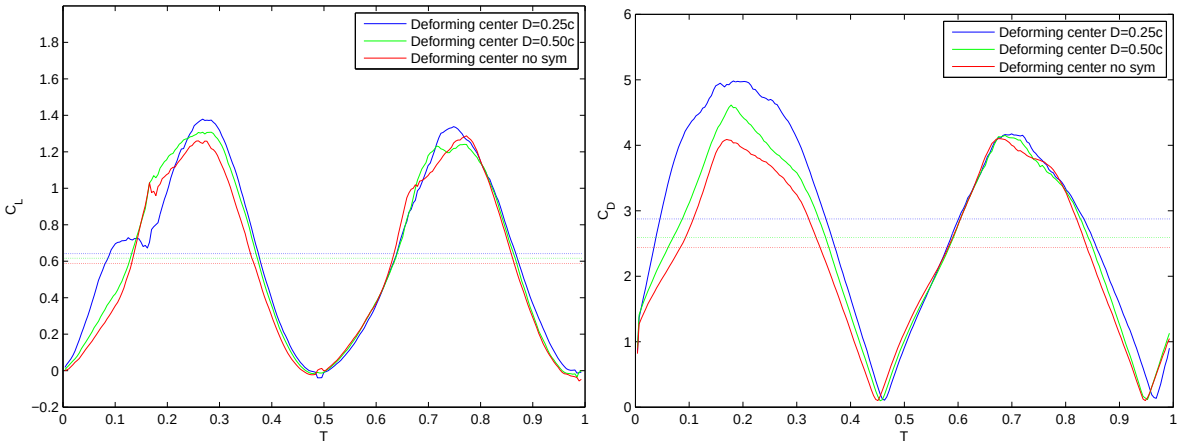

(a) (b)

Figure 6.20: Lift and drag coefficient plot for the spanwise varying deforming center cases, at different distances from the symmetry plane. The motion starts with an outstroke.

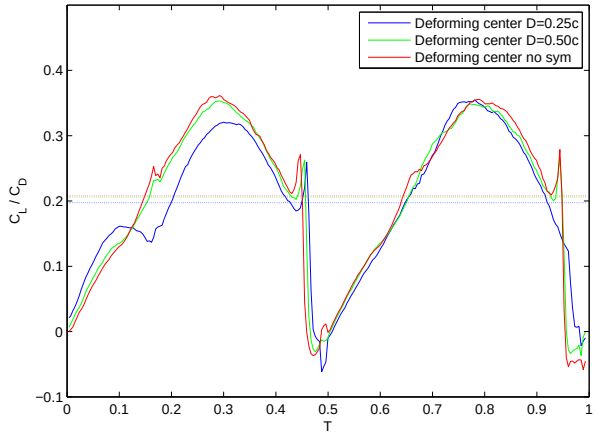

Figure 6.21: C_L/C_D plot for the spanwise varying deforming center cases, at different distances from the symmetry plane.

6.3.2 Deforming center case

The lift and drag coefficient for the three deforming center cases are shown in Figure 6.20, and their cycle average values are listed in Table 6.3. As for the rigid cases of the previous subsection, moving the plate closer to the symmetry plane increases the average force coefficients, particularly during the outstroke. The buildup of C_L for the $\mathbf{D}$=0.25c case is much higher than for the other two cases, but the positive effect of C_L is again limited by the earlier interaction with the LEV from the previous stroke. The interaction also takes considerably longer for this case. No interaction occurs for the $\mathbf{D}$=0.25c case during the instroke. As in the rigid case, moving the plate closer to the symmetry plane increases the average C_L and C_D and decreases the average C_L/C_D.

The case without the symmetry plane shows a slight difference between the instroke and the

Case	C_L	C_D	C_L/C_D	$\Delta\ C_L$	$\Delta\ C_D$	$\Delta\ C_L/C_D$
Rigid **D**=0.25c	0.5979	2.5778	0.2049	+11.3%	+16.9%	-3.7%
Rigid **D**=0.50c	0.5558	2.2998	0.2140	+3.4%	+4.3%	+0.6%
Rigid no symmetry	0.5373	2.2045	0.2127	0	0	0
Deforming center **D**=0.25c	0.6414	2.8739	0.1971	+9.2%	+18.0%	-5.1%
Deforming center **D**=0.50c	0.6171	2.5911	0.2058	+5.1%	+6.4%	-0.9%
Deforming center no symmetry	0.5874	2.4359	0.2077	0	0	0

Table 6.3: Difference in force coefficients with varying distance to the symmetry plane for the rigid and deforming center case.

outstroke. The outstroke shows interaction with the previous shed LEV at T=0.18, whereas the instroke shows a much smaller effect on C_L, around T=0.68. Investigation of the flow field does show interaction between the LEV and the shed vortex, and the non-averaged values in fact do show a hump in lift coefficient for the final instroke. However the two earlier instrokes do not show any interaction. This shows the difficulty of predicting interaction with the previously shed LEV. If the interaction does not occur during every instroke or every outstroke, averaging has to be done differently, if at all possible. If averaging is not possible due to cycle-to-cycle variations in the forces, it will be much harder to distinguish physical phenomena from the fluctuations caused by the interpolation method. The full force response of the case without symmetry plane is shown in Appendix B.3, Figure B.8.

6.3.3 Effect of deformation

As mentioned in Section 5.2.4 comparing the coefficients of different deforming cases directly could give misleading results due to the elongation of the chords. However it is possible to compare how changing the distance to the symmetry plane affects the coefficients for the different cases. Table 6.3 shows the cycle average values of C_L, C_D and C_L/C_D for the cases of this section, along with the difference compared to a plate without symmetry plane. The results show that the difference between a single plate without symmetry plane and the plate at **D**=0.25c increases C_L with approximately 10% and C_D with approximately 17%. This causes C_L/C_D to be reduced by roughly 4%. The increase in C_L is higher for the rigid case than for the deforming center case, whereas the increase in C_D is lower. The reason can be found from the interaction with the previously shed vortex. At larger distances from the symmetry plane the slower build up of the LEV causes the interaction to occur very late, at which point its impact is small. The faster LEV development caused by the proximity of the symmetry plane causes the interaction to occur earlier, resulting in a much larger impact on C_L. Although the interaction occurs slightly earlier for the rigid case with **D**=0.25c as well, the difference is much smaller compared to the case without symmetry plane.

Apart from the difference in interaction between the LEV and the previously shed vortex, moving the symmetry plane closer also moves the peak of the C_L curve to the right. This has a positive effect on C_L for the rigid case, whereas this effect is much smaller for the deforming center case. The timing of the peak will be discussed in the next section.

Spanwise constant cases		
Case	Time of peak C_L	Value C_L^{max}
Rigid **D**=0.50c	0.288	2.043
Deforming center **D**=0.50c	0.298	2.314
Deforming end **D**=0.50c	0.285	1.459
Spanwise varying cases		
Case	Time of peak C_L	Value of C_L^{max}
Rigid no symmetry	0.232	1.198
Rigid **D**=0.5c	0.236	1.175
Rigid **D**=0.25c	0.255	1.248
Deforming center no symmetry	0.272	1.259
Deforming center **D**=0.50c	0.276	1.298
Deforming center **D**=0.25c	0.276	1.373
Deforming end **D**=0.50c	0.272	1.257

Table 6.4: Timing of C_L peak during outstroke for all cases along with the associated value of C_L.

6.4 Peak timing

Several results showed a difference in timing of the peak in C_L and especially during the outstroke a later peak extends the period of lift buildup, leading to a higher C_L^{max}. The peak timings are examined in an attempt to find a possible explanation for this difference. The timing of the C_L peaks occurring during the outstroke is shown for all cases in Table 6.4, along with the value of C_L at the moment of the peak. The table shows some clear differences between the cases. The spanwise constant cases have considerably later peaks than the spanwise varying cases, especially for the rigid cases. For the constant spanwise cases the peak of the deforming end case is the earliest, and the deforming center case comes last.

In the spanwise varying deforming cases at **D**=0.50c the deforming center case also shows the latest peak, however, the deforming end has a peak at almost the same instant. The rigid case has a much earlier peak. Since both of the deforming cases show a later peak than the rigid case, this difference cannot be explained simply by the speed of the LEV buildup, since the LEV buildup will be faster than the rigid case for the deforming end case, and slower than the rigid case for the deforming center case. The elongation of the chords discussed in Section 5.2.4 also does not provide a complete explanation, since the spanwise constant deforming end has an earlier peak than the spanwise constant rigid case. A possible effect of the elongation of the chord would also not explain the difference in timing between the spanwise varying rigid case at different distances from the symmetry plane.

To find the an explanation for these differences in timing the behavior of the vortices around the plates is investigated. Since the spanwise varying rigid cases show a large difference in timing when the distance to the symmetry plane is changed, these cases are investigated first. Figure 6.22 show the contour plots of the Q criterion of these cases around the moment the

peaks occur, at 50% of the span. For the case without symmetry and the one with **D**=0.50c the peak in C_L occurs just before T=0.24, and for the case with **D**=0.25c the peak occurs after T=0.24. Particullary the difference in timing between the **D**=0.50c and **D**=0.25c cases is large with a difference of ΔT=0.02, whereas the difference between the case with **D**=0.50c and the case without symmetry plane is only ΔT=0.004. Looking at Figures 6.22d to 6.22f shows that the LEV is slightly lower, and closer to the surface of the plate for the **D**=0.25c case, compared to the other two cases. The LEV is also strongest for the **D**=0.25c case, and weakest for the case without symmetry plane. Looking at how the LEVs develop from T=0.20 to T=0.32 at 50% of the span does not show a clear explanation for the much larger difference in peak C_L timing between the **D**=0.50c and **D**=0.25c compared to the difference between the **D**=0.50c case and the case without symmetry plane. LEV development at different points along the span also does not show a clear explanation for this difference. These contour plots at different positions along the span are shown in Appendix B, Figure B.9.

Since the LEV cannot explain the difference in peak C_L timing, the other vortices are investigated. Figure 6.23 shows the pressure isosurfaces of the three spanwise varying rigid cases with $p = -2$, around the moment the peaks occur. In the figures it is possible to identify apart from the LEV, also the tip vortex and trailing edge vortex. Note that the 'hole' in the low pressure region near the trailing edge in Figure 6.23c is just the edge of the symmetry plane. A clear difference can be seen between the TEVs of the case with **D**=0.25c and the other two. For both the case without symmetry plane and the one with **D**=0.50c the TEV moves downward below the plate (Figures 6.23a-6.23d-6.23g and 6.23b-6.23e-6.23h), whereas it moves upward over the upper surface of the plate for the case with **D**=0.25c (Figures 6.23c-6.23f-6.23i). The large low pressure region caused by the TEV moving over the upper surface of the plate will affect the forces on the plate, and could therefore explain the difference in the C_L peak timing.

To investigate whether the assumption that the different behavior of the TEV causes the difference in peak C_L timing is also true for different cases, apart from those in Figure 6.23, the same pressure isosurfaces with $p = -2$ are shown for the spanwise varying deforming center cases. These isosurfaces are shown in Figure 6.24. As for the spanwise varying rigid cases, the TEV moves downward below the plate for the the cases without symmetry plane and with **D**=0.50c (Figures 6.24a-6.24d-6.24g and 6.24b-6.24e-6.24h), whereas it moves upward over the upper surface of the plate for the case with **D**=0.25c (Figures 6.24c-6.24f-6.24i). In these cases the different motion of the TEV does not appear to affect the timing of the C_L peak however, since Table 6.4 shows that the timing of the peak for the case with **D**=0.50c and **D**=0.25c is exactly the same. Further comparison of Figures 6.23 and 6.24 in fact shows very similar TEV behavior for the rigid and deforming center case, when at the same distance to the symmetry plane. The reason the TEV behavior does not have a large effect on the peak C_L timing for the deforming center case can be explained by the orientation of the plate. Near the trailing edge the surface of the plate is almost vertical, meaning it cannot have a large contribute to C_L. So although the TEV behavior will affect the peak C_L timing for the rigid cases, the timing is also affected by other effects to create the difference between the rigid case and the deforming center case.

Since the TEV behavior alone cannot explain the differences in peak C_L timing between the rigid and deforming center cases, the tip vortices are also investigated. Figures 6.25 and 6.26

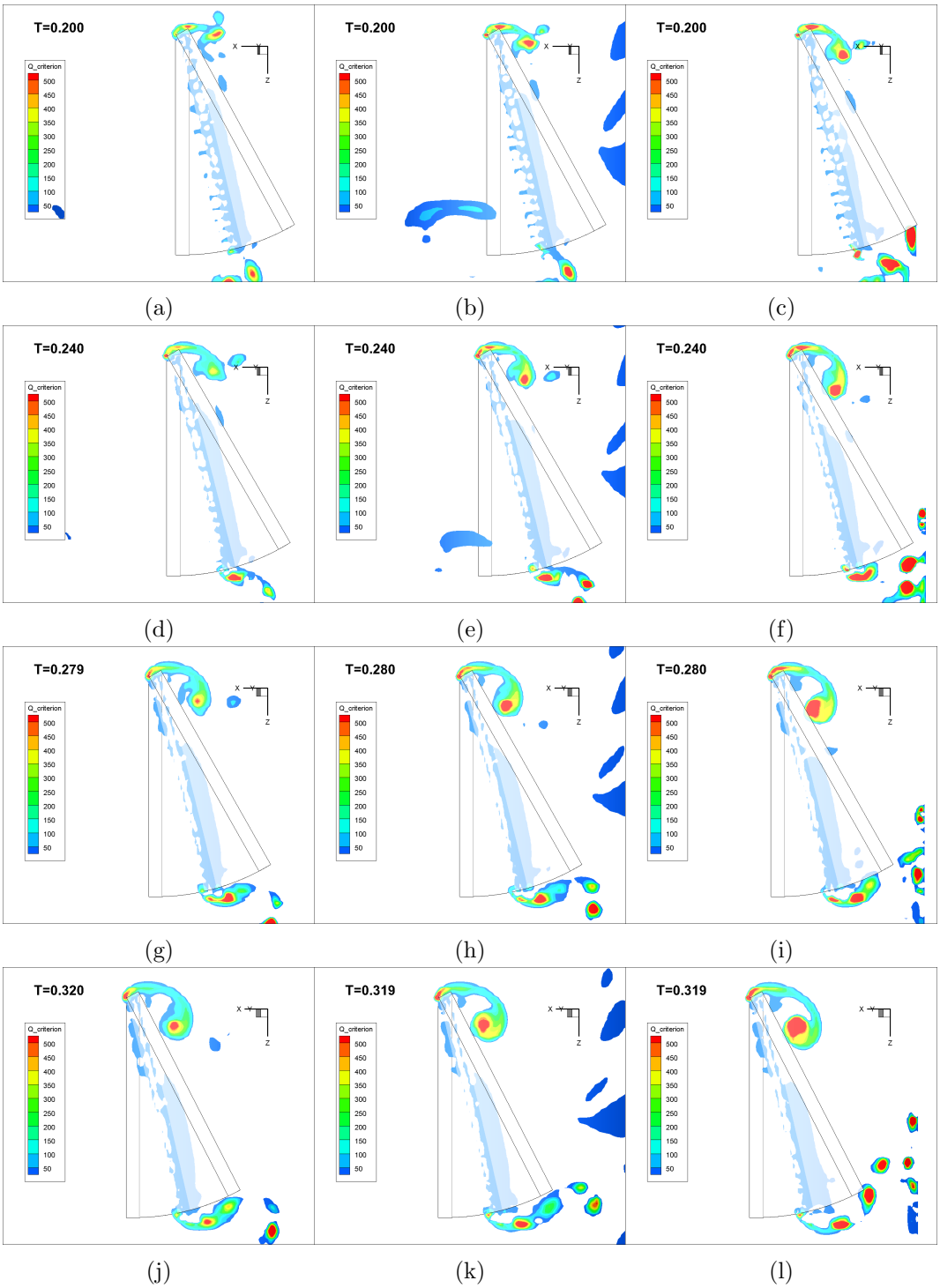

Figure 6.22: Contour plots of Q criterion for the spanwise varying cases at different distances from the symmetry plane at 50% span. Left without symmetry plane, in the center at **D**=0.50c and right at **D**=0.25c.

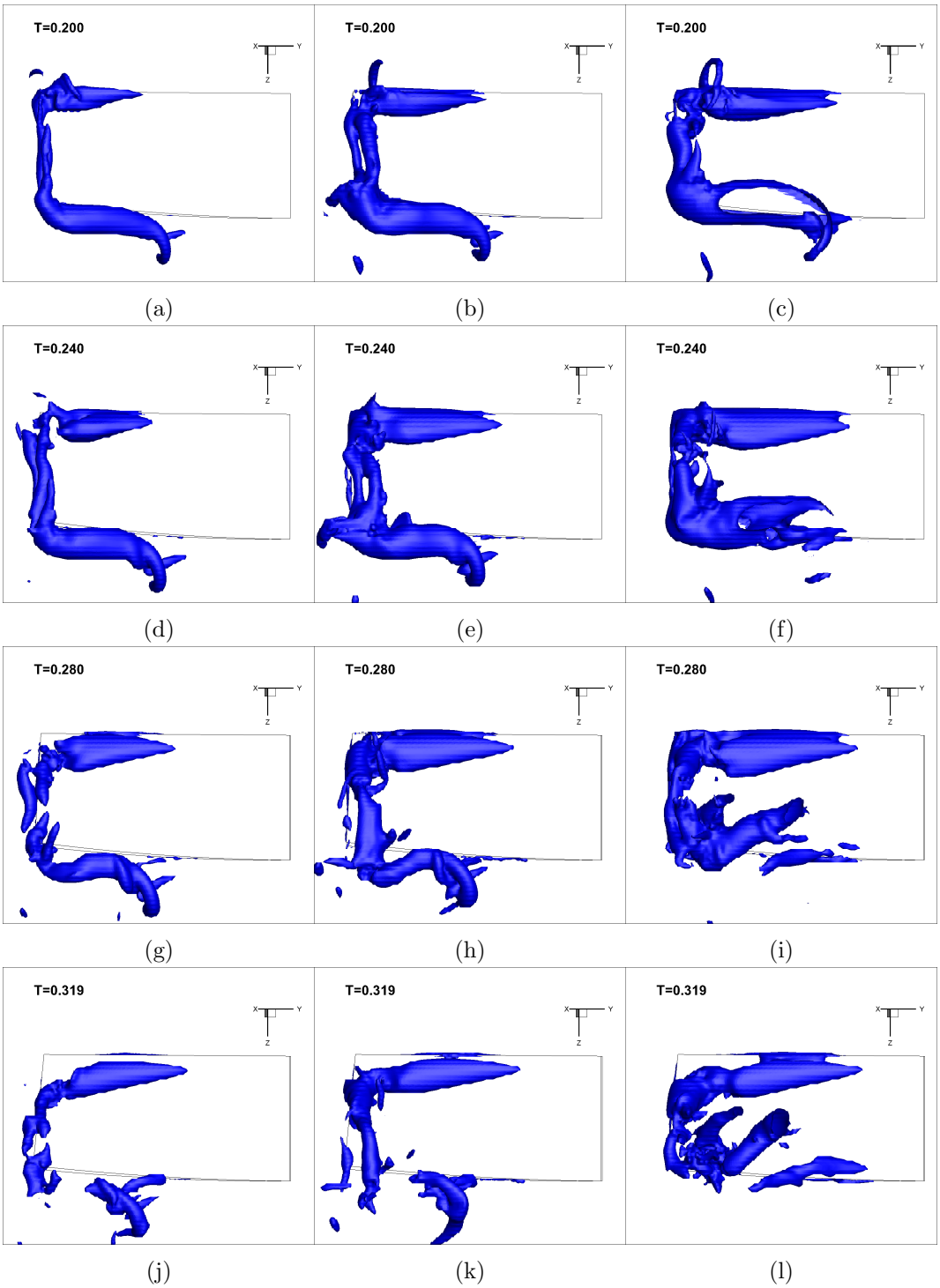

Figure 6.23: Side view of the isosurfaces of the pressure with $p = -2$ for the spanwise varying rigid cases at various distances from the symmetry plane. Left without symmetry plane, in the center at **D**=0.50c and right at **D**=0.25c.

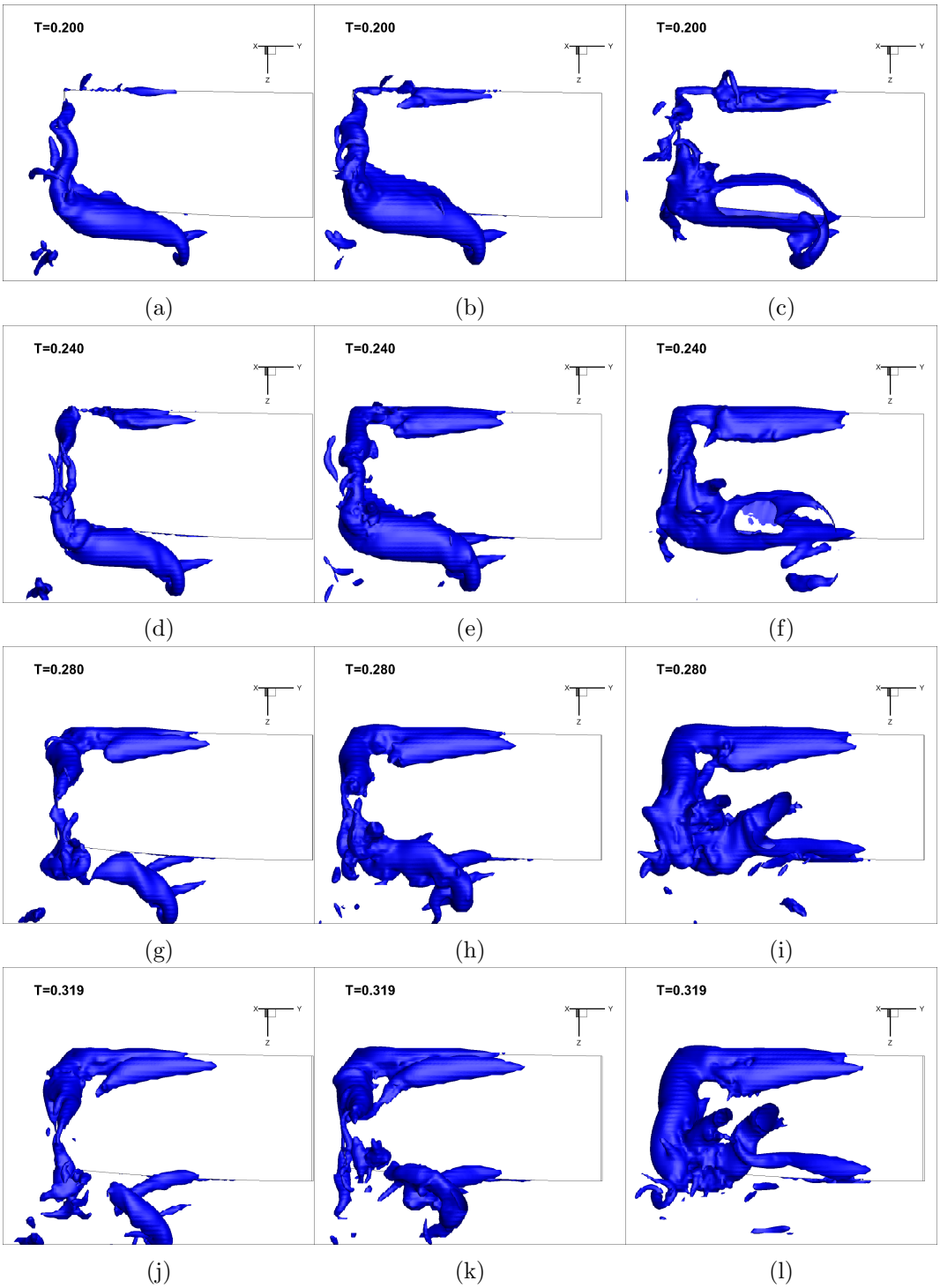

Figure 6.24: Isosurfaces of the pressure with $p = -2$ for the spanwise varying deforming center cases at various distances from the symmetry plane. Left without symmetry plane, in the center at $\mathbf{D}$=0.50c and right at $\mathbf{D}$=0.25c.

show a different view of the isosurfaces from Figures 6.23 and 6.24, and show the development of the TVs for both the rigid and deforming center cases respectively, at different distances from the symmetry plane. Comparing the rigid and deforming center cases shows a clear difference between the TVs created, especially near the leading edge. For the rigid cases the TV is attached from the leading edge to approximately 25% of the chord around T=0.24 (Figures 6.25d to 6.25f), and detaches towards T=0.28 for the cases without symmetry plane and with $\mathbf{D}$=0.50c (Figures 6.25g and 6.25h), and around T=0.32 for the case with $\mathbf{D}$=0.25 (Figure 6.25l). For the deforming center cases on the other hand, the TV is attached from the leading edge to approximately 40% of the chord for the case without symmetry plane and with $\mathbf{D}$=0.50c at T=0.24(Figures 6.26d and 6.26e), increasing to approximately 60% around T=0.32 (Figures 6.26j to 6.25k). For the case with $\mathbf{D}$=0.25c the TV is fully attached around T=0.24 and T=0.28 (Figures 6.26f and 6.26i), reducing to 60% around T=0.32 (Figure 6.26l). The low pressure region associated to the TV will have a large influence on C_L when it is near the leading edge, due to the orientation of the plate in the deforming center case. The fact that the TV is fully attached for the case with $\mathbf{D}$=0.25c does not have a large effect on C_L, since the orientation of the plate is almost vertical for the last 40% of the chord, resulting in the very similar peak C_L times for the deforming center cases.

The clear influence of the local orientation of the plate at the location of the TV and TEV on C_L also plays a role in the peak C_L timing of the deforming end case. A view of the pressure isosurfaces where $p = -2$ for the spanwise varying deforming end case at T=0.24,0.28 and 0.32 is shown in Figure 6.27. It clearly shows the TEV staying closer to the trailing edge compared to the deforming center and rigid cases in Figures 6.23 and 6.24. Again the orientation of the plate is important, since the deforming end case has a nearly horizontal surface near the leading edge, increasing the effect of the TEV on C_L. For the same reason the absence of a TV near the leading edge will not influence the peak C_L timing for the deforming end case. As mentioned in Section 6.2 the actual chord of the deforming edge case should be shorter near the trailing edge tip, so it is likely that the effect of the TEV on the peak C_L timing should be smaller.

Finally the peak C_L timing of the spanwise constant cases has not been discussed yet. The pressure isosurfaces with $p = -2$ are shown for the spanwise constant cases at T=0.28 in Figure 6.28, along with the spanwise varying cases at $\mathbf{D}$=0.50c. From the figure it is clear that TEVs and TVs found for the spanwise varying cases are larger and closer to the plates for the spanwise constant cases. For the rigid case the difference between the peak C_L timing for the spanwise constant and spanwise varying cases is largest, since both the TEV and the TV have a large effect on C_L.

It can be concluded from this section that the deformation of the plate does not only affect the vortex formation around the plate, but also directly affects the way the created vortices affect the forces on the plate. For the deforming center case the TEV plays a much smaller role on C_L compared to the rigid case, whereas the TV plays a more significant role.

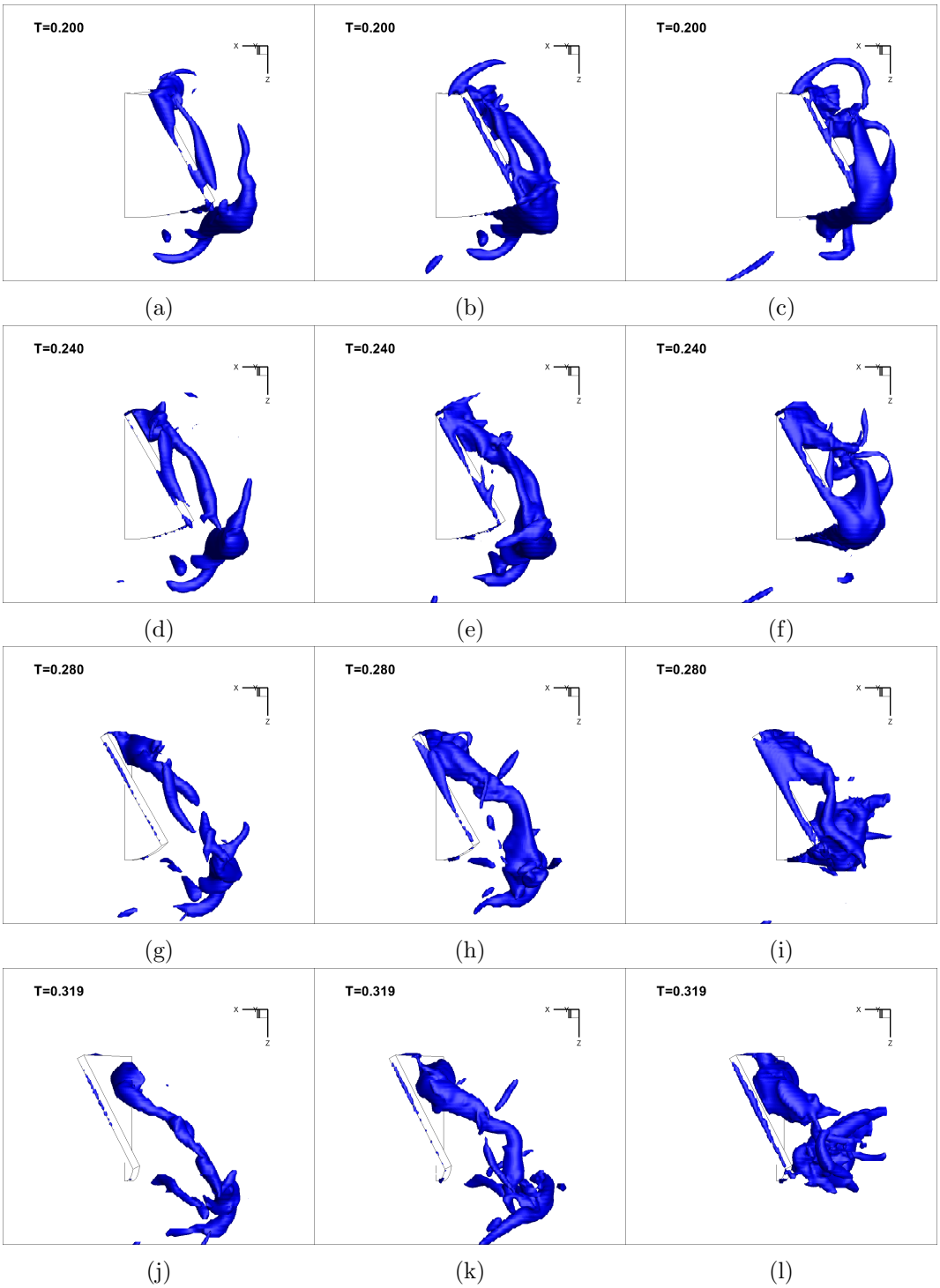

Figure 6.25: Side view of the isosurfaces of the pressure with $p = -2$ for the spanwise varying rigid cases at various distances from the symmetry plane. Left without symmetry plane, in the center at $\mathbf{D}$=0.50c and right at $\mathbf{D}$=0.25c.

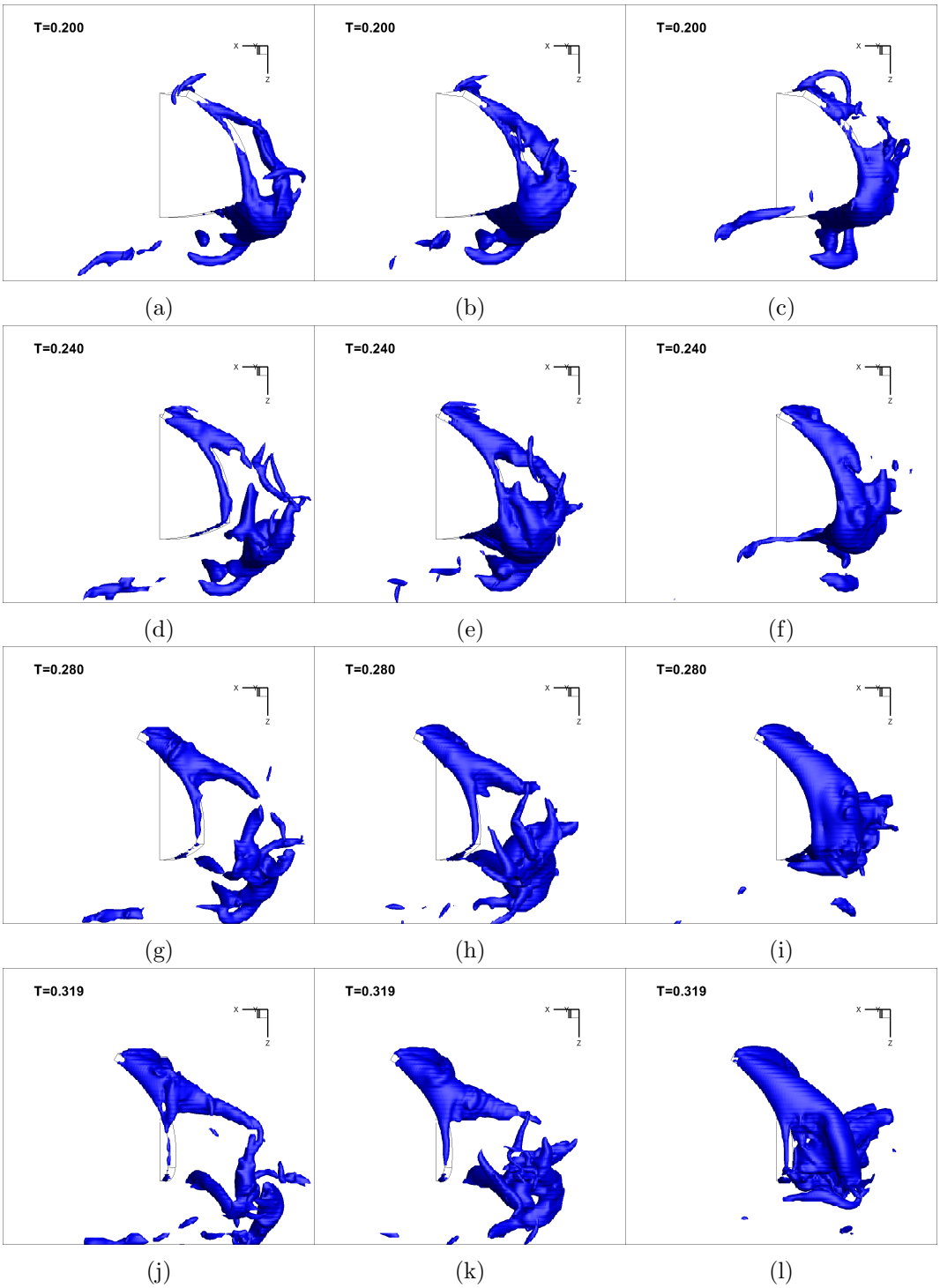

Figure 6.26: Side view of the isosurfaces of the pressure with $p = -2$ for the spanwise varying deforming center cases at various distances from the symmetry plane. Left without symmetry plane, in the center at $\mathbf{D}$=0.50c and right at $\mathbf{D}$=0.25c.

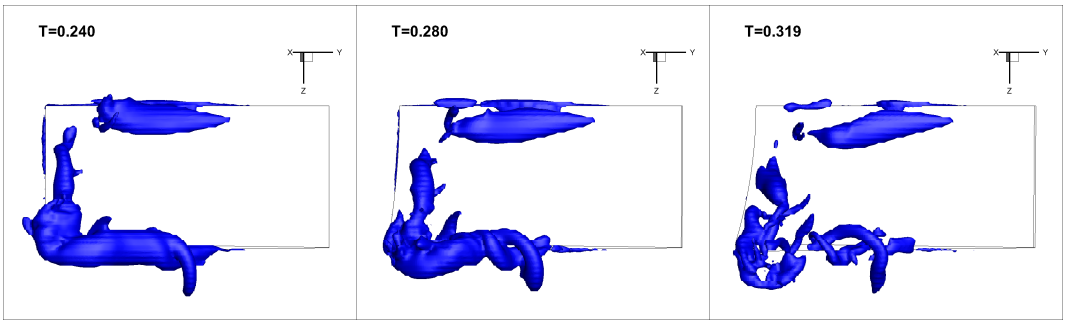

(a) (b) (c)

Figure 6.27: Isosurfaces of the pressure where $p = -2$ for the spanwise varying deforming end case at different times. a) T=0.204, b) T=0.280, c) T=0.319.

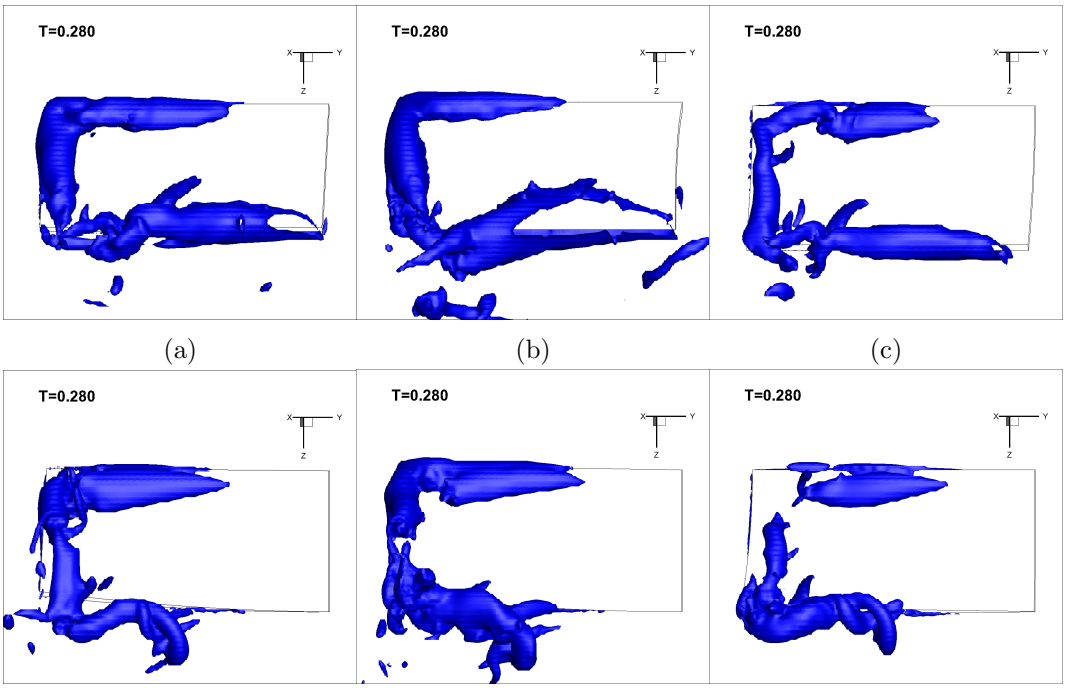

(a) (b) (c)

(d) (e) (f)

Figure 6.28: Isosurfaces of the pressure with $p = -2$ at T=0.28 for the spanwise constant cases on the top, and the spanwise varying cases on the bottom, all at distance to the symmetry plane of $\mathbf{D}$=0.50c. Left the rigid cases, in the center the deforming center cases and at the right deforming end cases.

Chapter 7

Conclusions and Recommendations

This study investigated the effect of chord deformation on the unsteady aerodynamic mechanisms found in hovering flapping flight at a Reynolds number of $\mathcal{R}e = 2002$. This was done by defining two different types of deforming chords, as well as a rigid plate rotating around its leading edge. These were simulated in a flapping motion next to a symmetry plane. The simulations included three cases with a spanwise constant deformation and three cases with a spanwise varying deformation. The influence of the deformation on the positive and negative effects of changing the distance to the symmetry plane was also investigated for two cases. Finally, distinct differences in the timing of the peak in the lift coefficient were found between certain cases, and the behavior of the vortices around the plates was investigated to find an explanation for these differences.

All simulations were performed using a three-dimensional immersed boundary solver. Although this solver had been used before, a validation case was simulated to gain better insight into the performance of the solver. The conclusions that could be drawn from the performed validation and simulations are stated in this chapter. After the conclusions some recommendations are given for future research.

7.1 Conclusions

7.1.1 Validation

The spurious forces inherent to the solver were investigated. From the frequency of the fluctuations it was concluded that they are caused by the boundary moving from one cell to another crossing a grid point. The frequency of the fluctuations was exactly equal to $\frac{U}{\Delta x}$. The amplitude of the fluctuations was expected to be of order $O(\frac{\Delta x}{\Delta t})$. Although reducing Δx and increasing Δt did reduce the fluctuations, they were found to be of order $\frac{\Delta x^{0.63}}{\Delta t^{0.45}}$. A more extensive grid and time step study might provide insight into the reason the found order

differs from the expected order, but was not performed in this study.

To validate the solver an experiment by Kim and Gharib (2011) was simulated. In this experiment a flat plate was accelerated from rest to a constant velocity inside a watertank. This was first simulated using a non-moving flat plate with an accelerating inflow. Since the exact velocity profile during the acceleration was not known, a smooth profile was chosen. Due to this different acceleration the initial force peak did not match between the simulation and experiment. After a constant force coefficient was reached the value found by the simulation was around 6% lower than that found in the experiment. A second case with the plate moving and zero inflow showed results similar to that of the steady plate, with differences explained by the difference between the inflow velocity and the velocity 'felt' by the plate. The steady state force coefficient found for the moving plate was 6% lower than for the steady plate, and 11% lower than the experimental results.

To compare the flow fields, the results of the simulation had to be interpolated to match the resolution of the experiment, since the lower resolution of the experiment had a significant effect on the representation of the flow field. No significant differences could be detected between the isosurfaces of the vorticity magnitude of the experiment and those created from the interpolated simulation results.

A grid refinement study showed no difference in the steady state force coefficient between the coarsest grid with $\Delta x = 0.012$ and the finest grid with $\Delta x = 0.006$ for both the simulation with a steady plate and the one with a moving plate. A difference of 1.5% for the initial peak height was found between the coarsest grid and the finest grid for the steady plate, and a difference of 4.5% for the moving plae. The second hump found in the force response showed no grid convergence.

7.1.2 Simulation results

For the cases with spanwise constant deformation, the deforming center case creates the highest lift coefficient, followed by the rigid case, and the deforming end case creates the lowest lift coefficient. This is not caused by shedding of the leading edge vortex, since no shedding is observed for any of the cases. The difference in lift coefficient is instead caused by the difference in pressure on the lower side of the plates. The curvature of the surface in the deforming center case increases the pressure on the lower surface, whereas the curvature of the deforming end case reduces the pressure.

The deforming end case creates a higher angle of attack near the leading edge. This higher angle of attack causes a faster C_L buildup, created by the faster buildup of the LEV. The deforming center case lowers the angle of attack at the leading edge, causing a slower LEV buildup and therefore slower C_L buildup. In all cases the presence of the symmetry plane increases LEV buildup, causing a higher C_L during the outstroke.

For the cases with spanwise varying deformation, the deforming center case create the highest lift coefficient, in this case followed by the deforming end case, with the rigid case showing

the lowest value of C_L. The high C_L of the deforming end case is caused by a low pressure region near the trailing edge of the tip of the plate, caused by a combination of the tip and trailing edge vortex. Due to the description of the deforming end case, the chord of the plate is elongated at this position, making it likely that the contribution of this low pressure region to C_L is overestimated.

A distinct hump is visible in C_L buildup of the cases with spanwise varying deformation. This hump is not caused by shedding of the LEV, since again no shedding is observed for any of the cases. Instead it is shown that this hump corresponds to interaction of the LEV with the LEV shed from the previous stroke. The interaction is delayed for the deforming center case, both by the slower LEV buildup and because the previously shed vortex gets trapped below the plate, limiting the interaction.

The presence of the symmetry plane increases the buildup speed of the LEV, and with this the C_L buildup. The difference between a plate without a symmetry plane and a plate with distance $\mathbf{D}$=0.25c to the symmetry plane shows an increase in C_L of 9.2% for the spanwise varying deforming center case, and 11.3% for the spanwise varying rigid case, whereas C_D increases 18.0% and 16.9% for the deforming center and rigid cases respectively. The positive effect of the faster LEV buildup on C_L is limited, since the stronger LEV interacts much faster with the vortex shed from the previous stroke, thus limiting further growth. As a result of this, the beneficial effect of the deforming center on delaying the interaction is reduced when moving the plate closer to the symmetry plane.

The moment the maximum C_L is reached during strokes varies for different cases. A later peak in C_L shows a longer C_L buildup and therefore leads to a higher C_L^{max}. The difference in timing appears to be caused by the trailing edge vortex and the tip vortex behavior. The effect of the TEV and TV behavior on the timing depends on the orientation of the surface of the plate on the location of the vortex. This dependence means the positive and negative effects on the TEV and TV depend on the shape of the plate. For the deforming center case, C_L benefits from a stronger TV near the leading edge, whereas for the deforming end case C_L benefits from the fact that the TEV stays closer to the trailing edge.

From the conclusions stated in this section it is clear that the deformation of the wing plays a significant role in the aerodynamic performance of a flapping wing during hover. This means it is important to take the deformation of the wings into account when designing an MAV. Overall it is seen that the deforming center case creates a higher C_L compared to the other cases, and reduces the negative effects of interaction with the previously shed LEV. As a result of this, designing a wing prone to deform in such a way will likely be beneficial to its performance.

7.2 Recommendations

The force results in this report were averaged to eliminate the fluctuations caused by the IBM scheme used for the simulation. The results show more cycles are needed to get a good average, and that for some cases averaging is not possible since the results are not periodic. A better

approach would be to eliminate the fluctuations by modifying the code itself. The studies of Seo and Mittal (2011) and Luo et al. (2012) have shown possible methods of suppressing the fluctuations, and especially the latter could be implemented into the solver with relative ease.

A second aspect that can be implemented into the IBM solver is the application of Fluid Structure Interaction (FSI). Application of two way FSI is complicated when using a discrete forcing approach for several reasons, including problems that are specific to the chosen method (Yang et al., 2008). A similar method to the one used in this study has been used for FSI simulations in Yang et al. (2008) and Yang and Stern (2012) however, and the same approach could be used to allow FSI calculations with the current solver. Implementing this ability will give the option to perform more specific studies on deformation effects on the aerodynamic performance of flapping insect wings.

One of the most important benefits of the lowering of the angle of attack by deforming the wing found in several studies was the delayed shedding of the leading edge vortex (Yin and Luo, 2010; Eldredge et al., 2010a; Gillebaart, 2011). In this study none of the cases showed shedding of the LEV, including the case where the angle of attack near the leading edge was increased by the deformation, so this benefit was not observed. Since the stability of the LEV is affected by the aspect ratio (Lentink and Dickinson, 2009; Harbig et al., 2013; Carr et al., 2013) shedding of the LEV might occur at higher aspect ratios, in which case the effect of the deformation on the stability would become important. Simulations with higher aspect ratio wings are necessary to investigate this issue and might show a more profound effect of the deformation of the LEV stability.

The stability and structure of the LEV is also affected by the maximum stroke angle (Carr et al., 2013). As with using higher aspect ratios, simulating larger stroke angles could show shedding of the LEV and a larger effect of the deformation on the LEV stability as well.

The deforming plates simulated in this study are very basic shapes that do not necessarily correspond to deforming wings seen in flying insects or MAVs. Although the simplification of the shapes allows for better generalization of the results, the simulation of more complex shapes would lead to a better link between the results and the performance of flying insects and MAVs. A trade-off can be made be made between the ability to generalize the results and the ability to compare results to a specific case, since wing deformation differs greatly with different structural and kinematic parameters. A full FSI simulation would be the ultimate specific case, whereas this study represents the other side of the spectrum, but several intermediate cases can be imagined that could have very interesting results.

Different deformation shapes are also required to study the effect of the deformation on the clap and fling mechanism. In this study the minimal distance of the plate to the symmetry plane simulated was 0.25 chordlengths, to prevent the plate from crossing the symmetry plane. In full clap and fling the wings will actually touch each other, causing very different deformations than the ones simulated in this study. The two-dimensional study of Gillebaart (2011) prescribed deformed wing shapes based on experimental data, and a similar method could be used to prescribe three-dimensional wings performing clap and fling.

This study showed that the deforming center case created the highest C_L. Simulating different

deformed shapes is recommended to see if it is possible to create an even higher C_L, or improve the C_L/C_D of the wing. A study investigating the optimal shape of the wing could lead to better wing designs, resulting in improved performance for MAVs.

Bibliography

Anderson, J. D., 2007: *Fundamentals of Aerodynamics*. Fourth international ed., McGraw-Hill, Singapore.

Ansari, S. A., N. Phillips, G. Stabler, P. C. Wilkins, R. Zbikowski, and K. Knowles, 2009: Experimental investigation of some aspects of insect-like flapping flight aerodynamics for application to micro air vehicles. *Experiments in Fluids*, **46**, 777–798.

Balaras, E., 2004: Modeling complex boundaries using an external force field on fixed cartesian grids in large-eddy simulations. *Computers and Fluids*, **33**, 375–404.

Carr, Z. R., C. Chen, and M. J. Ringuette, 2013: Finite-span rotating wings: three-dimensional vortex formation and variations with aspect ratio. *Exp Fluids*, **54 (1444)**, 1–26.

David, L., T. Jardin, P. Braud, and A. Farcy, 2012: Time-resolved scanning tomography piv measurements around a flapping wing. *Experiments in Fluids*, **52**, 857–864.

de Croon, G., K. de Clercq, R. Ruijsink, B. Remes, and C. de Wagter, 2009: Design, aerodynamics, and vision-based control of the delfly. *International Journal of Micro Air Vehicles*, **1 (2)**, 71–97.

Dickinson, M. H., F.-O. Lehmann, and S. P. Sane, 1999: Wing rotation and the aerodynamic basis of insect flight. *Science*, **284**.

Dudley, R., 2002: *The Biomechanics of Insect Flight: Form, Function, Evolution*. Reprint ed., Princeton University Press.

Eldredge, J. D., J. Toomey, and A. Medina, 2010a: On the roles of chordwise flexibility in a flapping wing with hovering kinematics. *Journal of Fluid Mechanics*, **659**, 94–115.

Eldredge, J. D., J. Toomey, and A. Medina, 2010b: On the roles of chordwise flexibility in a flapping wing with hovering kinematics. *Journal of Fluid Mechanics*, **659**, 94–115.

Ellington, C. P., 1999: The novel aerodynamics of insect flight: applications to micro-air vehicles. *The Journal of Experimental Biology*, **202**, 3439–3448.

Ellington, C. P., C. van den Berg, A. P. Willmott, and A. L. R. Thomas, 1996: Leading-edge vortices in insect flight. *Nature*, **384**, 626–630.

Fadlun, E. A., R. Verzicco, P. Orlandi, and J. Mohd-Yusof, 2000: Combined immersed-boundary finite-difference methods for three-dimensional complex flow simulations. *Journal of Computational Physics*, **161**, 35–60.

Gillebaart, T., 2011: Influence of flexibility on the clap and peel movement of the DelFly II. M.S. thesis, Delft University of Technology.

Gillebaart, T., S. van Zuijlen, and H. Bijl, 2011: Aerodynamic analysis of the wing flexibility and the clap-and-peel motion of the hovering delfly II. *Proceedings of the International Micro Air Vehicles conference 2011 summer edition.*

Groen, M. A., 2010: PIV and force measurements on the flapping-wing MAV DelFly II. M.S. thesis, Delft University of Technology.

Harbig, R. R., J. Sheridan, and M. C. Thompson, 2013: Reynolds number and aspect ratio effects on the leading-edge vortex for rotating insect wing planforms. *Journal of Fluid Mechanics*, **717**, 166–192.

Jardin, T., A. Farcy, and L. David, 2012: Three-dimensional effects in hovering flapping flight. *The Journal of Fluid Mechanics*, **702**, 102–125.

Kim, D. and M. Gharib, 2011: Flexibility effects on vortex formation of translating plates. *Journal of Fluid Mechanics*, **677**, 255–271.

Kim, D., F. Hussain, and M. Gharib, 2013: Vortex dynamics of clapping plates. *The Journal of Fluid Mechanincs*, **714**, 5–23.

Kim, J., D. Kim, and H. Choi, 2001: An immersed-boundary finite-volume method for simulations of flow in complex geometries. *Journal of Computational Physics*, **171**, 132–150.

Kolomenskiy, D., H. K. Moffatt, M. Farge, and K. Schneider, 2009: Vorticity generation during the clap-fling-sweep of some hovering insects. *Theory of Computational Fluid Dynamics*, **24**, 209–215.

Kristien M.E de Clercq, R. d. K., B. Remes, B. W. van Oudheusden, and H. Bijl, 2009: Aerodynamic experiments on delfly II: Unsteady lift enhancement. *International Journal of Micro Air Vehicles*, **1 (4)**, 217–224.

Lee, J., J. Kim, H. Choi, and K.-S. Yang, 2011: Sources of spurious force oscillations from an immersed boundary method for moving-body problems. *Journal of Computational Physics*, **230**, 2677–2695.

Lehmann, F.-O., 2004: The mechanisms of lift enhancement in insect flight. *Naturwissenschaften*, **91**, 101–122.

Lehmann, F.-O., 2008: Review when wings touch wakes: understanding locomotor force control by wake-wing interference in insect wings. *The Journal of Experimental Biology*, **211**, 224–233.

Lehmann, F.-O. and S. Pick, 2007: The aerodynamic benefit of wing-wing interaction depends on stroke trajectory in flapping insect wings. *The Journal of Experimental Biology*, **210**, 1362–1377.

Lentink, D. and M. H. Dickinson, 2009: Rotational accelerations stabilize leading edge vortices on revolving fly wings. *The Journal of Experimental Biology*, **212**, 2705–2719.

Liao, C.-C., Y.-W. Chang, C.-A. Lin, and J. McDonough, 2010: Simulating flows with moving rigid boundary using immersed-boundary method. *Computers & Fluids*, **39**, 152–167.

Lighthill, M., 1973: On the weis-fogh mechanism of lift generation. *Journal of fluid mechanics*, **60**, 1–17.

Luo, H., H. Dai, P. Ferreira de Sousa, and B. Yin, 2012: On the numerical oscillation of the direct-forcing immersed-boundary method for moving boundaries. *Computers & Fluids*, **56**, 61–76.

Maxworthy, T., 1979: Experiments on the weis-fogh mechanism of lift generation by insects in hovering flight. part I. dynamics of the fling. *Journal of fluid mechanics*, **93**, 47–63.

Mazaheri, K. and A. Ebrahimi, 2010: Experimental investigation of the effect of chordwise flexibility on the aerodynamics of flapping wings in hovering flight. *Journal of Fluids and Structures*, **26**, 544–558.

Miller, L. A. and C. S. Peskin, 2004: A computational fluid dynamics of clap and fling in the smallest insects. *The Journal of Experimental Biology*, **208**, 195–212.

Miller, L. A. and C. S. Peskin, 2009: Flexible clap and fling in tiny insect flight. *The Journal of Experimental Biology*, **212**, 3076–3090.

Mittal, R. and G. Iaccarino, 2005: Immersed boundary methods. *Annu. Rev. Fluid Mech.*, **37**, 239–261.

Nakata, T. and H. Liu, 2012: Aerodynamic performance of a hovering hawkmoth with flexible wings: a computational approach. *Proceedings of the Royal Society B*, **279 (1729)**, 722–731.

Okamoto, M. and A. Azuma, 2005: Experimental study on aerodynamic characteristics of unsteady wings at low reynolds numbers. *AIAA Journal*, **43 (12)**, 2526–2536.

Percin, M., Y. Hu, B. Oudheusden, B. Remes, and F.Scarano, 2011: Wing flexibility effects in clap-and-fling. *Proceedings of the International Micro Air Vehicles conference 2011 summer edition.*

Sane, S. P., 2003: The aerodynamics of insect flight. *The Journal of Experimental Biology*, **206**, 4191–4208.

Seo, J. H. and R. Mittal, 2011: A sharp-interface immersed boundary method with improved mass conservation and reduced spurious pressure oscillations. *Journal of Computational Physics*, **230**, 73477363.

Shyy, W., H. Aono, S. Chimakurthi, P. Trizila, C.-K. Kang, C. Cesnik, and H. Liu, 2010: Recent progress in flapping wing aerodynamics and aeroelasticity. *Progress in Aerospace Sciences*, **46**, 284–327.

Srygley, R. B. and A. L. R. Thomas, 2002: Unconventional lift-generating mechanisms in free-flying butterflies. *Nature*, **420**, 660–664.

Sudhakar, Y. and S. Vengadesan, 2010: The functional significance of delayed stall in insect flight. *Numerical Heat Transfer, Part A: Applications: An International Journal of Computation and Methodology*, **58 (1)**, 65–83.

Sun, M. and J. Tang, 2002: Unsteady aerodynamic force generation by a model fruit fly wing in flapping motion. *The Journal of Experimental Biology*, **205**, 55–70.

Sun, M. and X. Yu, 2003: Flows around two airfoils performing fling and subsequent translation and translation and subsequent clap. *ACTA MECHANICA SINICA*, **19 (2)**, 103–117.

Sun, M. and X. Yu, 2006: Aerodynamic force generation in hovering flight in a tiny insect. *AIAA JOURNAL*, **44 (7)**, 1532–1540.

Tay, W., B. W. van Oudheusden, and H. Bijl, 2014: Numerical simulation of x-wing type biplane flapping wings in 3d using the immersed boundary method. *Bioinspiration and Biomimetics*, **9**, 1–21.

Tay, W. B., B. W. van Oudheusden, and H. Bijl, 2012: Validation of immersed boundary method for the numerical simulation of flapping wing flight. *International Micro Air Vehicle Conference and Flight Competition (Braunschweig)*, 1–21.

Trizila, P., C.-K. Kang, H. Aono, and W. Shyy, 2011: Low-reynolds-number aerodynamics of a flapping rigid flat plate. *AIAA Journal*, **49 (4)**, 806–824.

Usherwood, J. R. and C. P. Ellington, 2002a: The aerodynamics of revolving wings I. model hawkmoth wings. *The Journal of Experimental Biology*, **205**, 1547–1564.

Usherwood, J. R. and C. P. Ellington, 2002b: The aerodynamics of revolving wings II. propeller force coefficients from mayfly to quail. *The Journal of Experimental Biology*, **205**, 1565–1576.

van den Berg, C. and C. P. Ellington, 1997: The three-dimensional leading-edge vortex of a 'hovering' model hawkmoth. *Philosophical Transactions of the Royal Society B*, 329–340.

van Oudheusden, B. W., 2009: Insect Flight Inspired New Generation of Flapping-Wing Micro-Aircraft. Delft University of Technology, STW Research Proposal, Delft University of Technology.

Walker, J. A., 2002: Rotational lift: something different or more of the same? *The Journal of Experimental Biology*, **205**, 3783–3792.

Wang, Z. J., 2000: Two dimensional mechanism for insect hovering. *Physical Review letters*, **85 (10)**, 2216–2219.

Wang, Z. J., J. M. Birch, and M. H. Dickinson, 2003: Unsteady forces and flows in low reynolds number hovering flight: two-dimensional computations vs robotic wing experiments. *The Journal of Experimental Biology*, **207**, 249–260.

Weish-Fogh, T., 1973: Quick estimates of flight fitness in hovering animals, including novel mechanisms for lift production. *The Journal of Experimental Biology*, **59**, 169–230.

Yang, J., 2005: An embedded boundary formulation for large-eddy simulation of turbulent flows interacting with moving boundaries. Ph.D. thesis, University of Maryland.

Yang, J. and E. Balaras, 2006: An embedded-boundary formulation for large-eddy simulation of turbulent flows interacting with moving boundaries. *Journal of Computational Science*, **215**, 12–40.

Yang, J., S. Preidikman, and E. Balaras, 2008: A strongly coupled, embedded-boundary method for fluid-structure interactions of elastically mounted rigid bodies. *Journal of Fluids and Structures*, **24**, 167–182.

Yang, J. and F. Stern, 2012: A simple and efficient direct forcing immersed boundary framework for fluid-structure interactions. *Journal of Computational Physics*, **231**, 5029–5061.

Yin, B. and H. Luo, 2010: Effect of wing inertia on hovering performance of flexible flapping wings. *Physics of Fluids*, **22 (11)**, 1071–1080.

Zbikowski, R., 2002: On aerodynamic modeling of an insect-like flapping wing in hover for micro air vehicles. *Philosophical Translations of the Royal Society of London A*, **360**, 273–290.

Zhang, X. Q., P. Theissen, and J. U. Schlter, 2013: Towards simulation of flapping wings using immersed boundary method. *International Journal for Numerical Methods in Fluids*, **71**, 522–536.

Appendix A

Interpolation points method

To determine which points are inside a body a small Fortran function is written. This code uses the coordinates of the 8 corners to determine whether points are in or outside of a rectangular cuboid. This function consist of several smaller functions that are all called by the main function **find_inside_points**

A.1 Function input

The function will receive the coordinates of the eight corners and an array containing all grid points of which it should be determined if they are inside the body. This array consist of 4 columns containing the x, y and z coordinate of each gridpoint, and a fourth column which will contain a 0 if the point is outside, and a 2 if the point is inside of the body. This column contains the only value that can be changed by the function. The function can also receive a start and finish index number, to limit the number of grid points that are checked. The first action of the function is to create surfaces from the corner points. To correctly do this the corner coordinates have to be given in a fixed order. This order is shown in Figure A.1. The surfaces are created by the function **build_surfaces**

A.2 Determining the cuboids boundaries

To find which points are inside the cuboid their coordinates are checked against the surfaces. For example, all points that are inside the cuboid depicted in Figure A.1 must have a x coordinate higher than the surface **1-5-8-4**, and lower than the surface **2-6-7-3**. These surfaces will be referred to as **bottom_x** and **top_x**. The same is done for the y and z coordinates and the other surfaces. In the situation as depicted in Figure A.1 determining which surfaces should be used for which coordinate is quite obvious. However, if the cuboid would start to rotate around the line **1-5**, this would become harder. At one point the surface

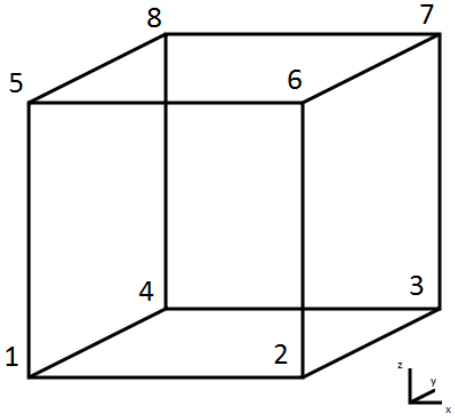

Figure A.1: Order in which the corner coordinates should be given to the function.

2-6-7-3 would become parallel to the original position of surface **3-7-8-4**, at which point it can no longer be used to determine if the x coordinate is in or outside of the cuboid. To make sure the correct surface is used the **bottom_** and **top_** surfaces for each coordinate are determined at every timestep. A surface cannot serve as a bottom or top to any coordinate if all its edges are perpendicular to one of the other coordinate axes. This can be checked by calculating the derivatives of the edges. Again referring to Figure A.1, the derivatives of the edges belonging to surface **2-6-7-3**, would be $\frac{\partial x}{\partial y}_{23} = 0$, $\frac{\partial x}{\partial y}_{26} = \mathbf{NaN}$, $\frac{\partial x}{\partial z}_{23} = \mathbf{NaN}$, $\frac{\partial x}{\partial z}_{26} = 0$, $\frac{\partial y}{\partial z}_{23} = \infty$ and $\frac{\partial y}{\partial z}_{26} = 0$ as well as 1 divided by these derivatives ($\frac{\partial y}{\partial x}_{23}$, $\frac{\partial y}{\partial x}_{26}$, **...**) with **NaN** representing Not a Number which is the result of $\frac{0}{0}$. The surface that is a top or bottom surface for the x coordinate should have at least one edge that has a real and finite derivative for $\frac{\partial x}{\partial y}$ and one for $\frac{\partial x}{\partial z}$. So surface **2-6-7-3** can be the top surface for the x coordinate since it has $\frac{\partial x}{\partial y}_{23} = 0$ and $\frac{\partial x}{\partial z}_{26} = 0$, and it can be seen that only **1-5-8-4** also has this. As the cuboid rotates it is possible that four or even all six surfaces have real and finite derivatives for a certain coordinate. In this case the other derivatives are compared, to make sure the surface that is selected is the one least suited for any of the other coordinates, while making sure no surface is used for two different coordinates. The only thing left to do is determine which surface is the top and which is the bottom surface, which is done by calculating the average value of the coordinate for which they are the top and bottom. The assigning of **top_** and **bottom_** is done by the function **find_derivatives**.

A.3 Determining surface slopes and angles

To determine if a point is below or above a surface the slope of the surface has to be known. The most straightforward case is shown in Figure A.2. Imagine the plane **ABCD** is the **top_z** surface, and it has to be checked if the z coordinate of point **E** is below this surface, with the z axis pointing out of the paper. This means it is required to know the z value of the surface, at the same x and y coordinate as point **E**. To do this the slope of the surface along the line $\mathbf{AE_{sur}}$ must be known, as well as the length of $\mathbf{AE_{sur}}$, calculated as

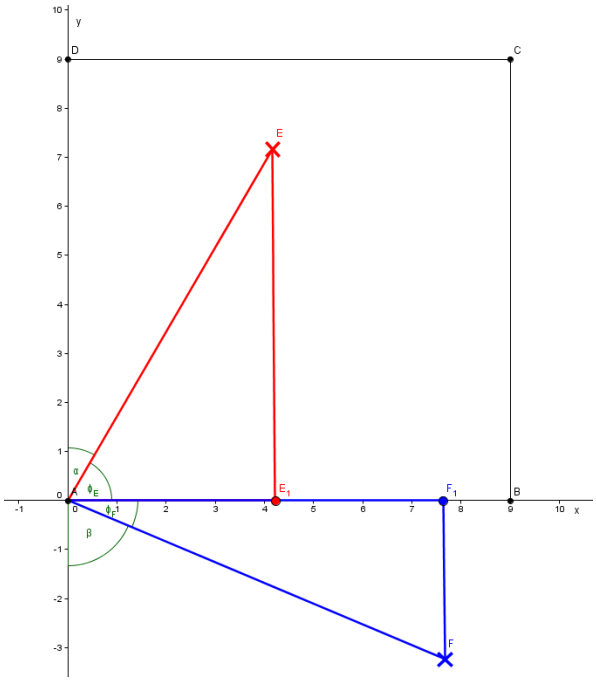

Figure A.2: Example situation in which to find the z coordinate of the surface at the x and y coordinates of points E and F.

$L = \sqrt{(x_E - x_A)^2 + (y_E - y_A)^2}$. Here $\mathbf{E_{sur}}$ is the projection of point $\mathbf{E}$ onto the surface. Although the length can be calculated directly, the slope of the surface along line $\mathbf{AE_{sur}}$ cannot. Therefore the line has to be split up into an x and a y component. This is done by first calculating corner α, and then using ϕ_E and L to calculate the lengths $\mathbf{E_{sur}E}_1$ and $\mathbf{E}_1\mathbf{A}$. These lengths can now simply be multiplied by derivatives $\frac{\partial z}{\partial x}$ and $\frac{\partial z}{\partial y}$ to find the z value at $\mathbf{E_{sur}}$. In case the point $\mathbf{F}$ is investigated the procedure is exactly the same, with the length $\mathbf{FF}_1$ getting a negative value. This is as if the surface $\mathbf{ABCD}$ is infinitely long in both x and y direction, having the same derivatives everywhere. This means the z value of $\mathbf{F}$ might be below this infinite surface, and the point can not be called outside of the body by checking its z coordinate. It can be clearly seen however, that the y value of the point is too low, and when checking **bottom_y** it will be called outside of the body.

Figure A.3 shows the same plane rotated around the z axis. The line $\mathbf{AE_{sur}}$ can again be separated into two components, one parallel to line $\mathbf{AB}$ and one to line $\mathbf{DA}$ with now the need to calculate both α and β, to be able to get ϕ. In this case the resulting lengths $\mathbf{E_{sur}E}_1$ and $\mathbf{E}_1\mathbf{A}$ can not be multiplied with the derivatives as in the previous case, since the lines have both an x and y component. Instead they are multiplied by the slopes of the surface edges, lines $\mathbf{AB}$ and $\mathbf{DA}$. The z coordinate of $\mathbf{E_{sur}}$ is now given by Equation A.1.

$$z_{E_{sur}} = \frac{z_D - z_A}{\sqrt{(x_D - x_A)^2 + (y_D - y_A)^2}}\mathbf{E_{sur}E}_1 + \frac{z_B - z_A}{\sqrt{(x_B - x_A)^2 + (y_B - y_A)^2}}\mathbf{E}_1\mathbf{A} \quad \text{(A.1)}$$

The final case that could occur is when surface $\mathbf{ABCD}$ would also rotate around the y axis. Continuing to look at in the $x - y$ plane gives the picture shown in Figure A.4. It can be

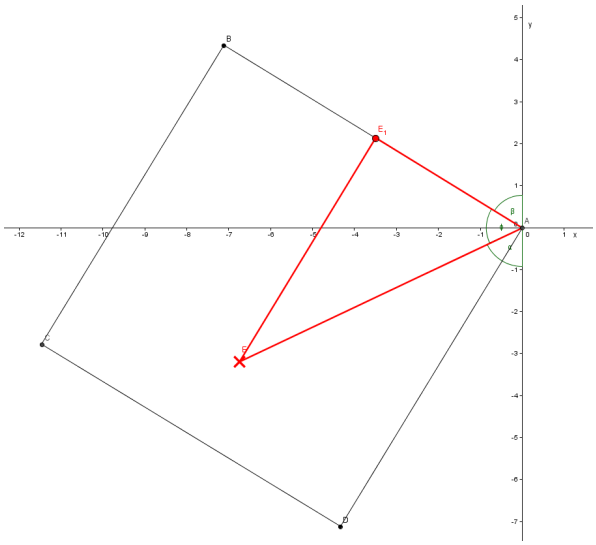

Figure A.3: Example with surface rotated around z axis.

clearly seen that the angle between the surface edges is no longer a straight angle, so splitting line $\mathbf{AE_{sur}}$ into two lines parallel to the two edges is less straightforward. The angle ϵ also has to be calculated, and will be equal to angle ϕ_2. Using this angle and ϕ_1 the last angle of the triangle, ϕ_3, can be calculated. Now that all angles are known the law of cosines can be used to calculate lengths $\mathbf{E_{sur}E_1}$ and $\mathbf{E_1A}$. The law of cosines is given in Equation A.2.

$$\mathbf{AE_{sur}}^2 = \mathbf{E_{sur}E_1}^2 + \mathbf{E_1A}^2 - 2\mathbf{E_{sur}E_1E_1A}\cos\phi_2 \tag{A.2a}$$

$$\mathbf{E_{sur}E_1}^2 = \mathbf{E_1A}^2 + \mathbf{AE_{sur}}^2 - 2\mathbf{E_1AAE_{sur}}\cos\phi_1 \tag{A.2b}$$

$$\mathbf{E_1A}^2 = \mathbf{AE_{sur}}^2 + \mathbf{E_{sur}E_1}^2 - 2\mathbf{AE_{sur}E_{sur}E_1}\cos\phi_3 \tag{A.2c}$$

After some manipulation of the cosine rule the lengths $\mathbf{E_1A}$ and $\mathbf{E_{sur}E_1}$ can be calculated with Equation A.3.

$$\mathbf{E_1A} = \frac{\mathbf{AE_{sur}}(1-\cos^2\phi_3)}{\cos\phi_1 + \cos\phi_2\cos\phi_3} \tag{A.3a}$$

$$\mathbf{E_{sur}E_1} = \mathbf{AE_{sur}}\cos\phi_3 + \mathbf{E_1A}\cos\phi_2 \tag{A.3b}$$

The z value of $\mathbf{E_{sur}}$ can now again be calculated using Equation A.1. This means that to be able to determine if the z coordinate of a point is below the surface **ABCD** for all instances, the values that should be known are the angle between line **AB** and the y axis, the angle between line **DA** and the y axis, the slope in z direction along both line **AB** and **DA**, the angle between line $\mathbf{AE_{sur}}$ and the y axis, and finally the length of the xy component of this same line. The last two of these value have to be calculated for each point individually, but

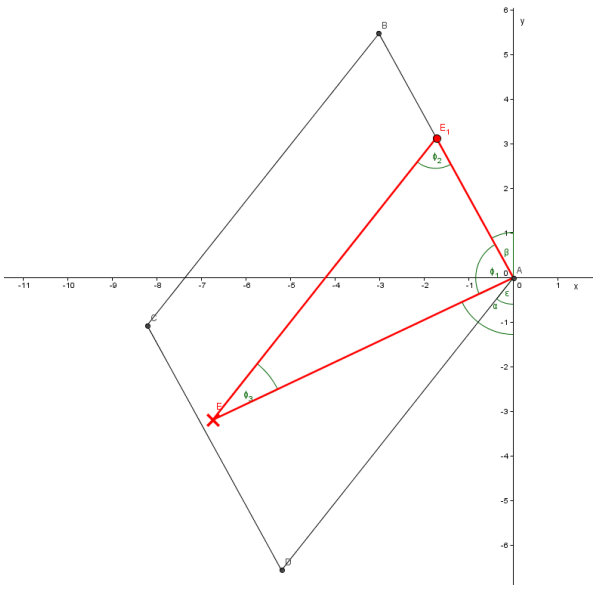

Figure A.4: Example with surface rotated around y axis.

the first four have to be calculated for the surface only once every timestep, and can then used to check multiple points.

The angles and slopes of the surface edges are calculated by the function **slopes**. This function is called six times, once for every surface. Finally the function **inside_point_finder** is called, which loops over all the given grid points and check if they are in or outside of the cuboid. In case it finds that the gridpoint is inside the body it will change the fourth value after the x, y and z coordinate from a 0 into a 2.

A.4 Limitations

The function was designed to check if points are inside of a rectangular cuboid. To create an efficient function to do this, some assumptions were made that do not have to be valid for different shapes. The requirements for the function to work correctly are

- The shape must have 8 different corners, and no more.
- The corners must be in the order shown in Figure A.1.
- All edges must be straight lines.
- All surfaces must be straight surfaces.

The second and fourth requirement are particularly important since the program might work when they are ignored, but the results will not represent the correct body. The third requirement cannot be ignored since the program does not have an option to use curved edges.

Appendix B

Extra figures for results

B.1 Extra figures for Section 6.1

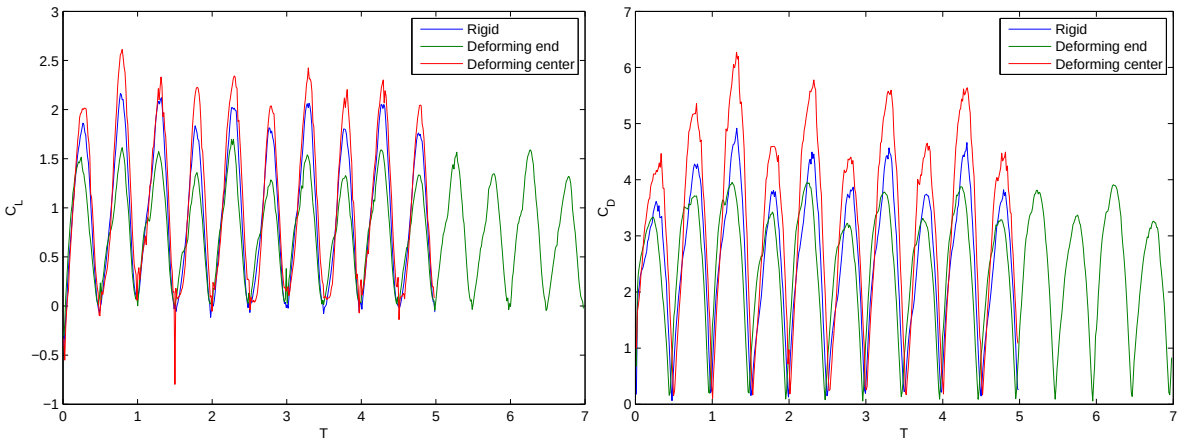

(a) (b)

Figure B.1: Full C_L and C_D response plot for the spanwise constant deforming cases. The coefficients are not corrected for the chord elongation.

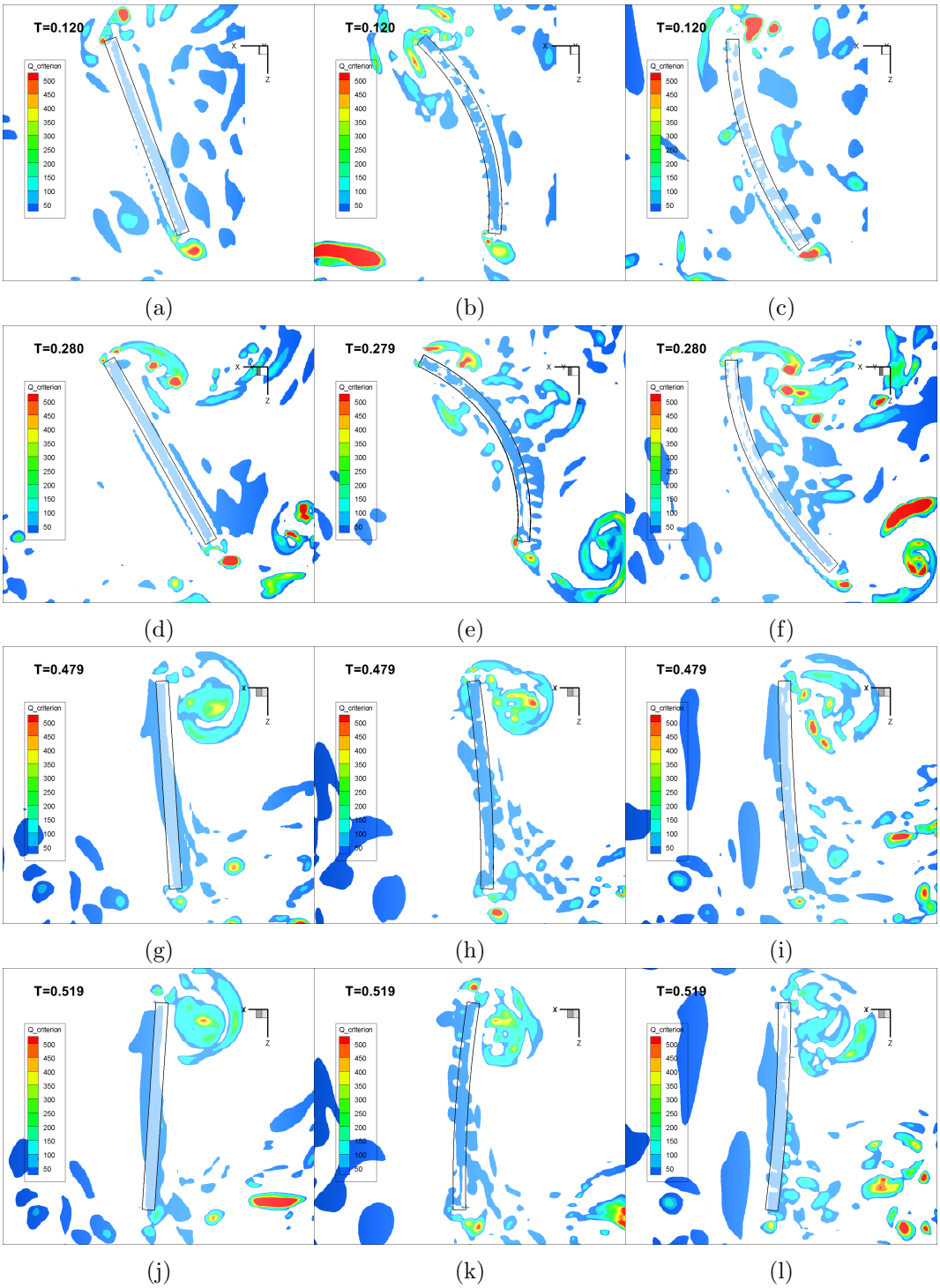

Figure B.2: Contour plots of the Q criterion at 75% span, for the spanwise constant deformation cases. On the left side the rigid case, in the middle the deforming center case and on the right side the deforming end case.

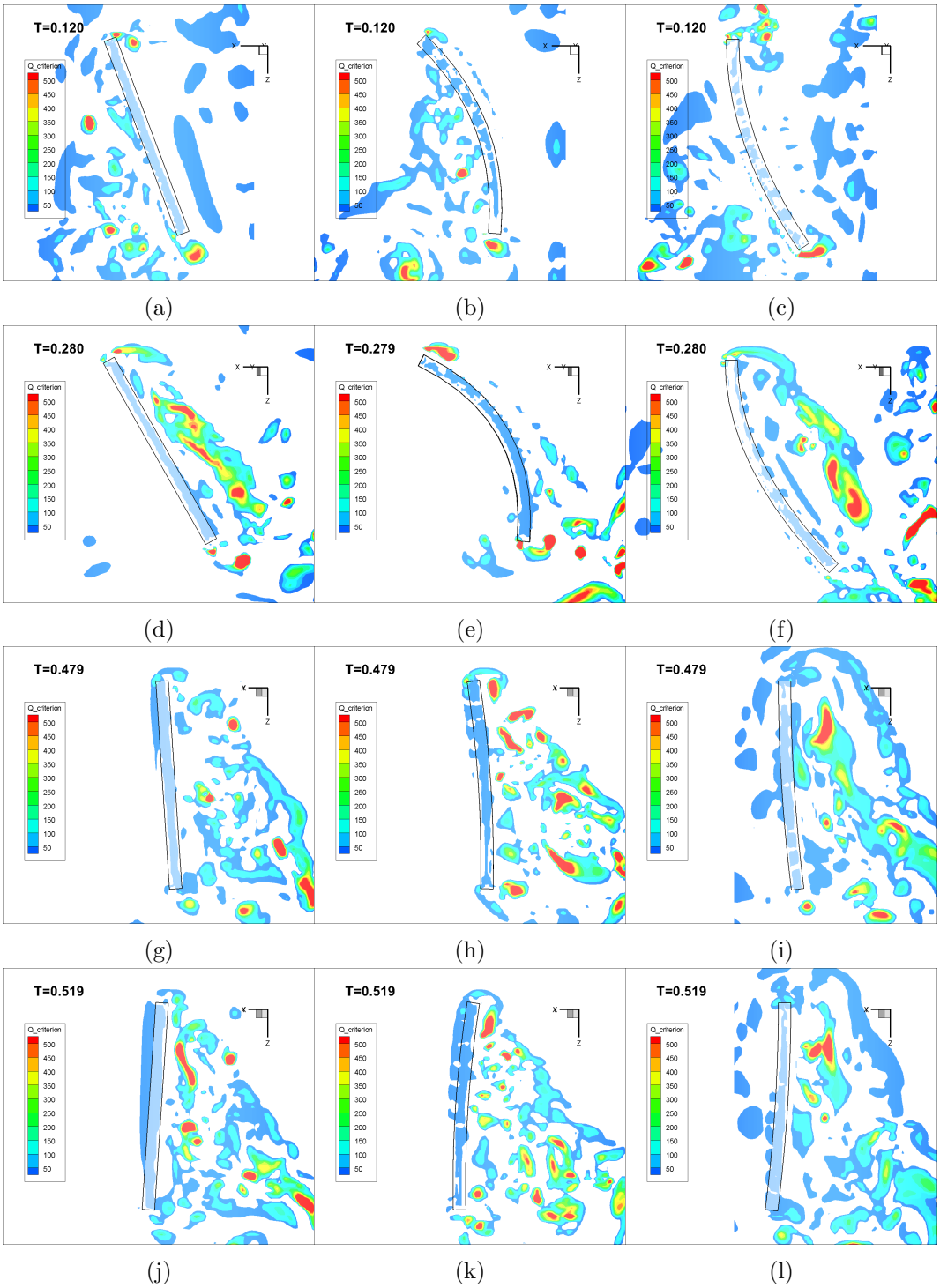

Figure B.3: Contour plots of the Q criterion at 90% span, for the spanwise varying deforming cases. On the left side the rigid case, in the middle the deforming center case and on the right side the deforming end case.

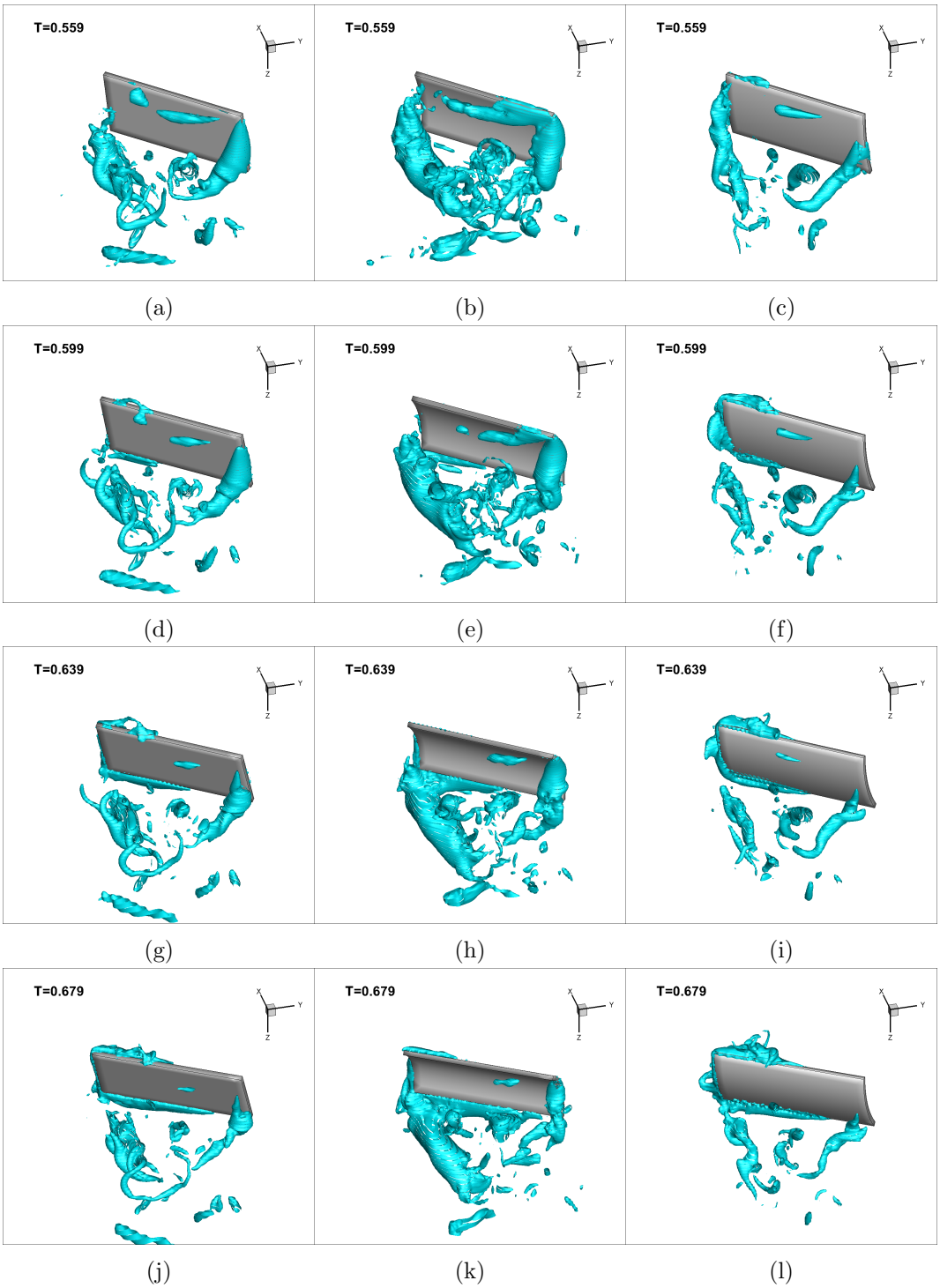

Figure B.4: Pressure isosurfaces of p=-1 during the instroke for the spanwise constant cases. On the left side the rigid case, in the middle the deforming center case and on the right side the deforming end case.

B.2 Extra figures for Section 6.2

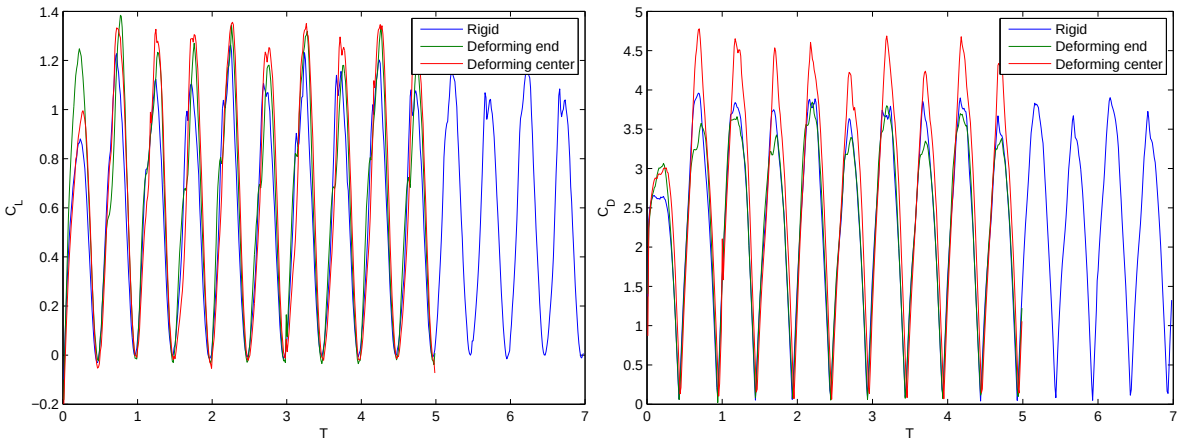

(a) (b)

Figure B.5: Full C_L and C_D response plot for the spanwise constant varying cases. The coefficients are not corrected for the chord elongation.

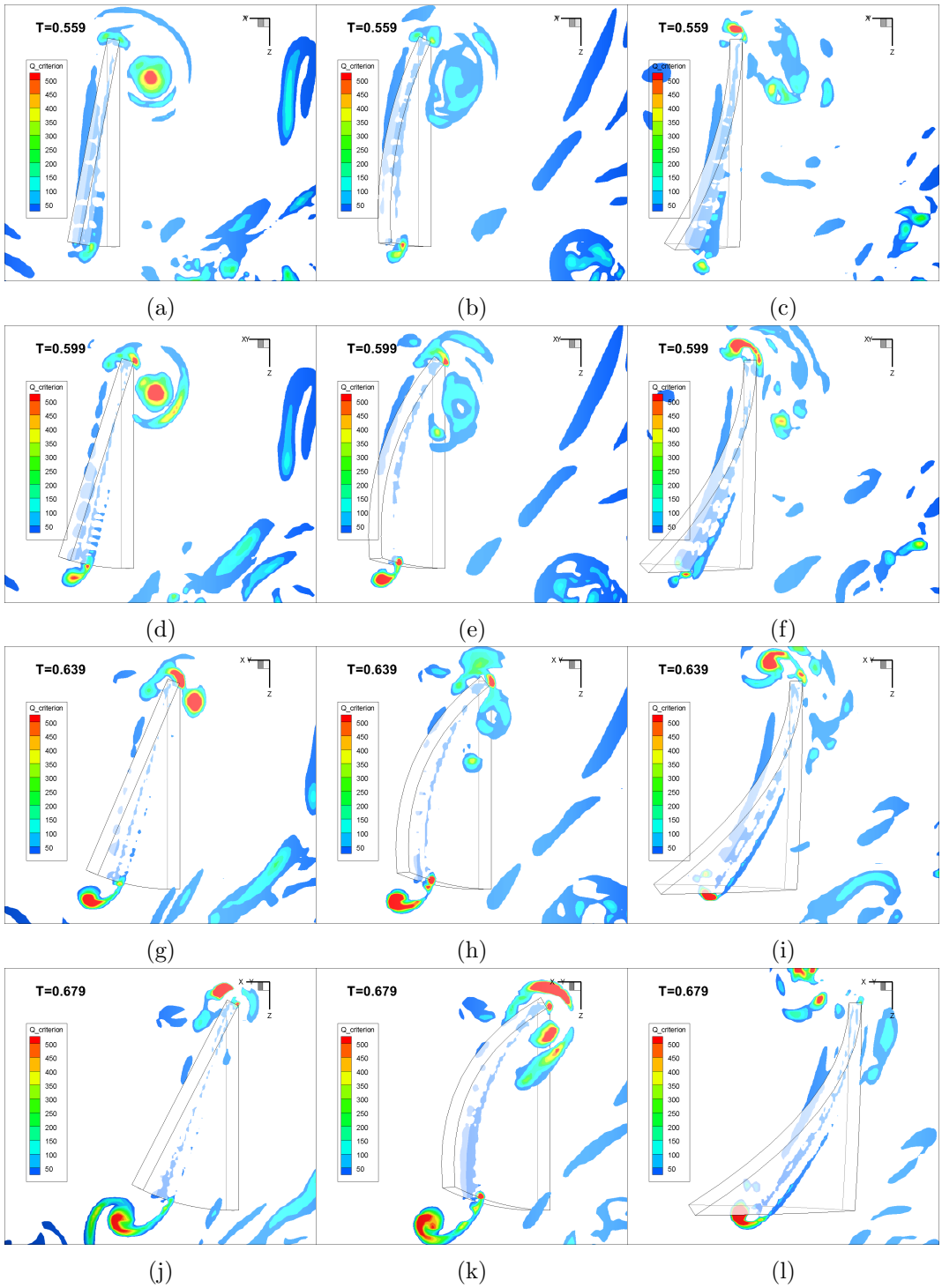

Figure B.6: Contour plots of the Q criterion at 75% span, for the spanwise varying deformation cases during the instroke. On the left side the rigid case, in the middle the deforming center case and on the right side the deforming end case.

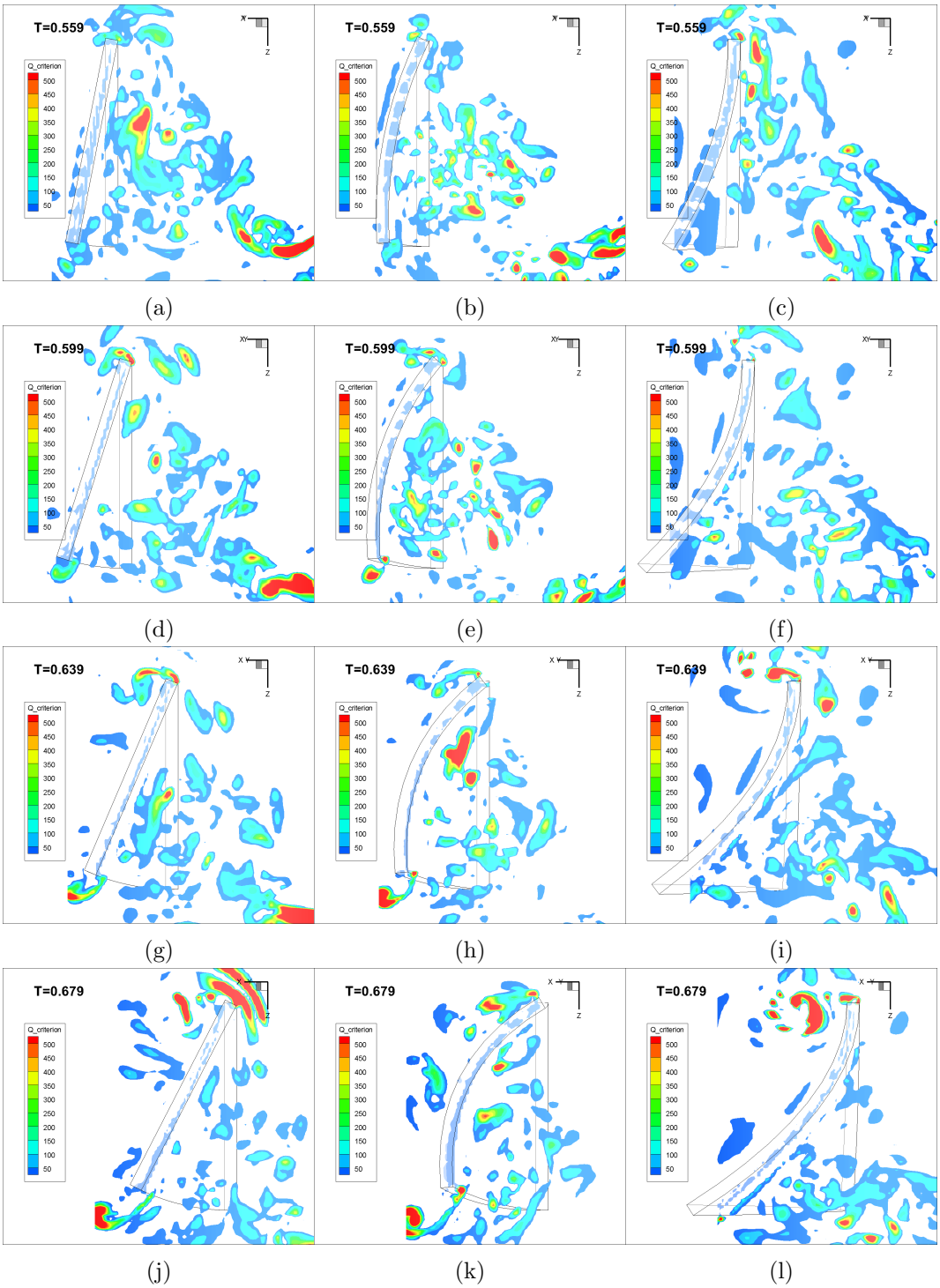

Figure B.7: Contour plots of the Q criterion at 90% span, for the spanwise varying deformation cases during the instroke. On the left side the rigid case, in the middle the deforming center case and on the right side the deforming end case.

B.3 Extra figures for Section 6.3

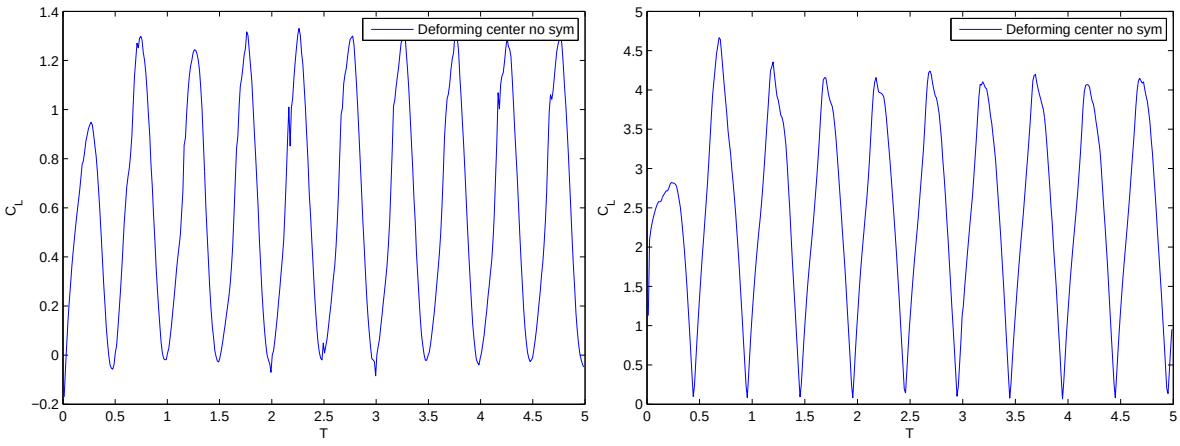

(a) (b)

Figure B.8: Lift and drag coefficient plot for the spanwise varying deforming center case without symmetry plane. The coefficients are not corrected for the chord elongation.

B.4 Extra figures for Section 6.4

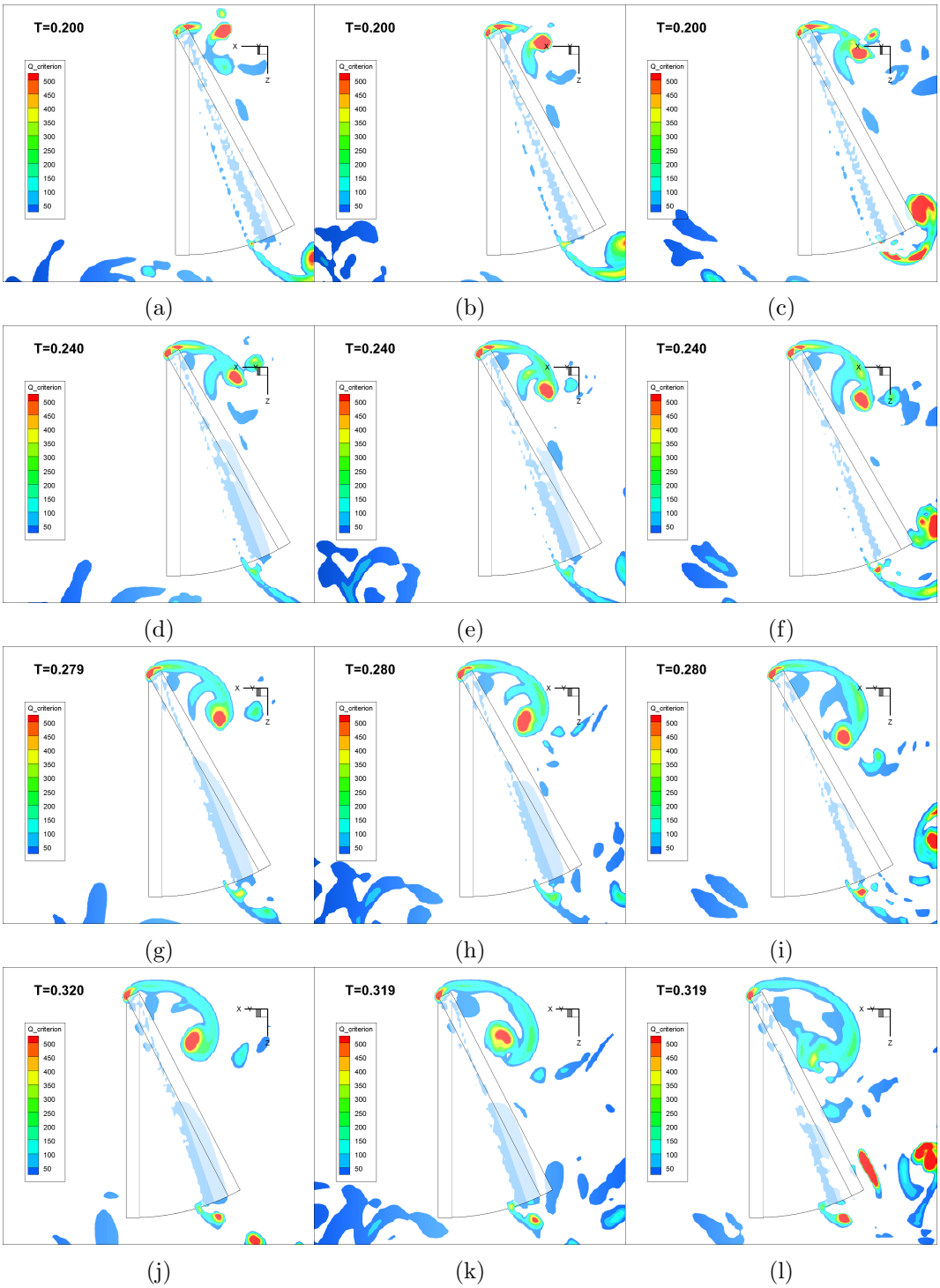

Figure B.9: Contour plots of Q criterion for the spanwise varying cases at different distances from the symmetry plane at 75% span. Left without symmetry plane, in the center at **D**=0.50c and right at **D**=0.25c.